Seismic imaging and thermal modeling of active continental rifting processes in the Salton Trough, southern California

Liang Han

Dissertation submitted to the faculty of the Virginia Polytechnic Institute and State University in partial fulfillment of the requirements for the degree of

Doctor of Philosophy
In
Geosciences

John A. Hole
Robert P. Lowell
Robert J. Bodnar
Martin C. Chapman
Joann M. Stock

January 16, 2016
Blacksburg, VA

Keywords: active rifting, crustal structure, Salton Trough, seismic tomography, controlled-source seismic, metamorphism, thermal modeling

Seismic imaging and thermal modeling of active continental rifting processes in the Salton Trough, southern California

Liang Han

ABSTRACT

Continental rifting ultimately creates a deep accommodation space for sediment. When a major river flows into a late-stage rift, thick deltaic sediment can change the thermal regime and alter the mechanisms of extension and continental breakup. The Salton Trough, the northernmost rift segment of the Gulf of California plate boundary, has experienced the same extension as the rest of the Gulf, but is filled to sea level by sediment from the Colorado River. Unlike the southern Gulf, seafloor spreading has not initiated. Instead, seismicity, high heat flow, and minor volcanoes attest to ongoing rifting of thin, transitional crust.

Recently acquired controlled-source seismic refraction and wide-angle reflection data in the Salton Trough provide constraints upon crustal architecture and active rift processes. The crust in the central Salton Trough is only 17-18 km thick, with a strongly layered but relatively one-dimensional structure for ~100 km in the direction of plate motion. The upper crust includes 2-3 km of Colorado River sediment. The basement below the sediment is interpreted to be similar sediment metamorphosed by the high heat flow and geothermal activity. Meta-sedimentary rock extends to at least 7-8 km depth. A 4-5 km thick layer in the middle crust is either additional meta-sedimentary rock or stretched pre-existing continental crust. The lowermost 4-5 km of the crust is rift-related mafic magmatic material underplated from partial melting in the hot upper mantle.

North American lithosphere in the Salton Trough has been almost or completely rifted apart. The gap has been filled by ~100 km of new transitional crust created by magmatism from below and sedimentation from above. These processes create strong lithologic, thermal, and rheologic layering. Brittle extension occurs within new meta-sedimentary rock. The lower crust, in comparison, stretches by ductile flow and magmatism is not localized. This seismic interpretation is also supported by 1D thermal and rheological modeling. In this passive rift driven by far-field extensional stresses, rapid sedimentation keeps the crust thick and ductile, which delays final breakup of the crust and the initiation of seafloor spreading.

To my dear family, friends and teachers.

ACKNOWLEDGEMENTS

First of all, I would like to express my sincere thanks to my advisors Dr. John. A. Hole and Dr. Robert. P. Lowell, who offered me the opportunity to pursue my M.S. and Ph.D. degree in Virginia Tech. Dr. Hole is my primary advisor for the Ph.D. study. He taught me English, science, and philosophy in life. I learned a lot from him in both scientific research and numerous field projects. Dr. Lowell was also my M.S. advisor, who has been my advisor and friend since then. I appreciate his understanding, enlightenment, respect and support whenever I am depressed or need help. I appreciate their countless guidance, support, encouragement and endurance in my academic pursuits. What I got from them is not limited to geophysics or science, but rather is applicable to my entire life.

I would like to thank my committee members: Dr. Robert Bodnar, Dr. Martin Chapman and Dr. Joann Stock for providing helpful suggestions on my research. Dr. Bodnar is a great advisor, who is always open to students and patient to lead them to the truth. I have often received help from his lectures and personal discussions, particularly about mineral reactions, magmatic systems and other geochemical processes. He is also a very smart and brave scientist. I was inadvertently inspired by his thoughts. Dr. Chapman is a professor on earthquake and controlled source seismology, who is always very supportive to all the students. He earned most respect and gratitude from geophysics graduate students. Dr. Stock is an expert on the geology in the Gulf of California and southern California. It is a great honor to have her in my dissertation committee. She is interested in a very broad research topics and very thoughtful. My research is greatly enlightened and guided by numerous resources from her on tectonics, earthquakes, faults and geothermal energy. Although Dr. Ying Zhou, Dr. Brian Romans, Dr. Mark Caddick, and Dr.

Scott King are not on the list of my committee members, I would like to thank them for what I have learned in their classes. I want to express my gratitude to Dr. Nancy Ross, Dr. Ken Eriksson, and Connie Lowe for providing me extended departmental financial support.

My earnest thanks also go to my group members, Kathy Davenport, Lindsay Sabey, Didem Beskardes, and David Konrad for the insightful discussion and generous help along the way. I also would like to thank my other friends at Virginia Tech, Kui Liu, Wei Cheng, Hui Tang, Qimin Wu, Zhen Guo, Shangxin Liu, Kannikha Kolandaivelu, Roberto Marivela, Amir Zainali, Youyi Ruan, Changyeol Lee, Di Wang, Meijing Zhang, Oluyinka Oyewumi, Daniel Moncada, Rosario Esposito, Kate Craft, Lei Liu, Matt Steele-Maclnnis, Aida Farough, Shreya Singh, Jaewoon Choi, Dave Mercier, Samuel Fortson, Pavithra Sekhar, Eric Kazlaukas, Karina Cheung, Tannistha Maiti, Sharmin Shamsalsadati, and Matthew Francis for their friendships. I regret not to enumerate all the friends here.

Last but not least, I would like to express my deepest gratitude to my family. I would like to thank my parents, my wife, and my sister for pure, unconditional and eternal love. They have given me the strength and courage to complete this work and move forward in life.

TABLE OF CONTENTS

Chapter 5

LIST OF FIGURES

LIST OF TABLES

Chapter 1

Introduction

1.1 Continental Rifting Process

The rifting of continental lithosphere is important for the evolution of continents and the transition to oceanic seafloor spreading. Passive margins caused by continental rifting are typically divided into three types, depending on the magma volume from decompression melting of the upper mantle. The first type of continental margins are "volcanic", with transitional crust composed primarily of voluminous syn-rift igneous rocks [e.g., *White and Mckenzie*, 1989; *Holbrook and Kelemen*, 1993]. The second type is so magma-starved that hyper-extension of the lithosphere exposed serpentinized mantle rocks at the seafloor [e.g., *Whitmarsh et al.*, 2001; *Hopper et al.*, 2004]. A third, intermediate class of continental margins can form extensive areas of new crust through a combination of lithospheric stretching, less voluminous magmatism, and extensive sedimentation. The roles of magmatism and sedimentation on the rifting of continental lithosphere for the third type are not well understood. The Salton Trough in southern California and northern Mexico is an excellent site to study this type of continental rifting process.

1.2 Salton Seismic Imaging Project

Salton Seismic Imaging Project (SSIP), funded by MARGINS/GeoPRISMS, Earthscope, and USGS, acquired seismic data in and across the Salton Trough in 2011 to investigate rifting processes at the northern end of the Gulf of California extensional province and earthquake hazards at the southern end of the San Andreas Fault system. Seven lines of refraction and wide angle reflection data were acquired onshore, two lines and a grid of airgun and OBS data were

acquired in the Salton Sea, and onshore-offshore data were recorded. Complete details of the project are described in *Rose et al.* [2013].

The five themes proposed for the "From Rifting to Drifting" process by GeoPRISMS are listed as below. 1) Melt generation in extensional environments: Mantle decompression, thermal state and composition of the mantle. 2) Magma-lithosphere interaction: diking, metasomatism, thermal weakening, changing the composition of the lithosphere, coupling between deformation and melt migration. 3) Stretching of the lithosphere: Strain localization in brittle and ductile rheology, rates of extension, punctuated events. 4) Feedback loops - rifting and surface processes: sedimentation, margin architecture. 5) Rifting and oceanic spreading - the missing link: Lithospheric breakup, focusing of melt delivery, evolution of mantle deformation. My own research has focused on three refraction seismic profiles in the Imperial Valley to constrain the metamorphosed sedimentary crystalline rock in the upper crust, and one refraction and wide angle reflection seismic profile parallel to the plate motion direction to constrain the active rifting process in the whole crust and upper mantle. The results have provided important insights into themes 3, 4 and 5, which are described in detail in following chapters.

1.3 Summary of Following Chapters

In Chapter 2, I study the metamorphosed sedimentary crystalline rock in the actively rifting Imperial Valley, California, by seismic imaging and correlation with borehole data in the Salton Sea geothermal field. Three 65-90 km seismic refraction profiles across the Imperial Valley are analyzed, two of which went through the volcanic and geothermal field in parallel and perpendicular to the plate motion direction. Both first arrival travel time tomography and frequency domain full waveform inversion are applied to provide high resolution velocity

models down to ~7 km depth. Along all three profiles, the P wave velocity increases gradually from ~1.8 km/s at the surface to ~6 km/s in the crystalline rock inside the valley, with no sharp vertical velocity contrast, indicating a gradational boundary between sediment and crystalline rock. The vertical gradient in velocity decreases at ~4 km/s. The vertical change in seismic velocity gradient coincides with changes in the gradients in porosity and density of borehole core samples, but not a metamorphic facies boundary. This occurs at ~2.8 km depth in most of the valley, but at only ~1.5 km depth in the Salton Sea geothermal field where the heat flow is highest. Borehole data shows progressive metamorphism of young sediment into crystalline rock. We interpret progressive metamorphism caused by the rift valley's high heat flow to be creating new crystalline crust throughout the valley at a rate comparable to the 2 km/Myr sedimentation rate.

In Chapter 3, I study the continental rupture and the creation of new crust in the active Salton Trough rift, southern California. A 250-km long NW-SE refraction and wide angle reflection seismic profile along the axis of the Salton Trough parallel to the direction of plate motion was analyzed to constrain the crustal and upper mantle velocity structure during active continental rifting. The results show that the crust is very thin and approximately one-dimensional from the northern Salton Sea to the southern end of the Imperial Valley. About 3 km of Colorado River sediment underlie the Salton Sea and Imperial Valley. The transition to underlying crystalline rock (~4.0 km/s) is characterized by a strong velocity gradient that reduces to much weaker gradient at ~2.8 km depth. This boundary is not a depositional surface, and the crystalline rock is interpreted to be sediment metamorphosed by high heat flow to at least 8 km deep. Deeper felsic crystalline rock with a velocity of ~6.2-6.7 km/s is less than 5 km thick, and might be stretched pre-existing crust or additional sediment metamorphosed to a higher grade.

High velocity (~6.8 km/s) lower crust between 13-14 km depth and the Moho is interpreted as rift-related underplated gabbros. The Moho is at 17-18 km depth and relatively flat. The upper mantle velocity is 7.8-7.9 km/s, indicative of high temperature and partial melting. Structure under the Coachella Valley is distinctly different. Sediment thins to the north and the underlying crystalline rock (~6 km/s, with a much smaller vertical gradient) is interpreted to be old granitic basement. Mafic rock does not exist at 14-18 depth as it does to the south, and a much weaker reflector suggests Moho at 28 km depth. Structure south of the international boundary in Mexico is less well constrained, but has slower mid-crustal velocity, and rocks with mantle velocity must be much deeper. The different basement and deeper Moho in the Coachella and Mexicali valleys suggest that the main rift zone lies between them, and is at least ~100 km wide. North American lithosphere in the central Salton Trough has been rifted apart for more than 100 km, and is being replaced by new crust added by magmatism from below and sedimentation from above. Structure is remarkably uniform in the middle and lower crust and upper mantle, despite the narrow volcanic, thermal and seismogenic rifting in the upper crust.

In Chapter 4, I develop a one dimensional numerical model of the extensional process in the Salton Trough, southern California, to study the thermal regime of the Salton Trough and the effects of thick sediment upon continental breakup. A simplified whole crust and upper mantle structure from that in Chapter 3 is used as the model setup, and a numerical scheme is developed following *Lachenbruch et al.* [1985] to simulate both steady-state and non-steady-state conditions. A simple benchmark shows that our numerical method has successfully reproduced the model results of *Lachenbruch et al.* [1985]. The modeled heat flow is consistent with the field measurements, if the middle crust is stretched pre-existing crust. The crustal rheology calculated from the modeled temperature profiles supports the interpretation that the deformation

in the lower crust in the Salton Trough is currently ductile. The same extension mechanism could continue for at least another 10 Myr, if the sedimentation is maintained at the same rate. Rapid sedimentation delays the breakup of the continental crust and prevents the initiation of mid-ocean ridges, by maintaining the thickness of the extended crust.

In Chapter 5, I briefly discuss possible future work on the continental rifting process and the SSIP dataset. A three dimensional geodynamic modeling on the rifting process and the effect of thick sedimentation upon continental rupture in the Salton Trough could be performed. A comparison with other rifted continental margins, such as the Eastern North American margins and the East Africa Rift System, is important to understand the full evolution of continental rifting. Some additional analysis on the rest of the SSIP dataset may contribute to this study.

References

Holbrook, W. S., and P. B. Kelemen, 1993. Large igneous province on the United States Atlantic margin and implications for magmatism during continental breakup, *Nature*, 364, 433-436.

Hopper, J. R., T. Funck. B. E. Tucholke, H. C. Larsen, W. S. Holbrook, K. E. Louden, D. Shillington, and H. Lau, 2004. Continental breakup and onset of ultraslow seafloor spreading off Flemish Cap on the Newfoundland rifted margin, *Geology*, 32, 93-96.

Lachenbruch, A. H., J. H. Sass, and S. P. Galanis, Jr., 1985. Heat flow in southernmost California and the origin of the Salton Trough, *J. Geophys. Res*., 90, 6709-6736.

Rose, E.J., G.S. Fuis, J.M. Stock, J.A. Hole, A.M. Kell, G. Kent, N.W. Driscoll, M. Goldman, A.M. Reusch, L. Han, R.R. Sickler, R.D. Catchings, M.J. Rymer, C.J. Criley, D.S. Scheirer, S.M. Skinner, C.J. Slayday-Criley, J.M. Murphy, E.G. Jensen, R. McClearn, A.J. Ferguson, L.A. Butcher, M.A. Gardner, I. Emmons, C.L. Loughran, J.R. Svitek, P.C. Bastien, J.A. Cotton, D.S. Croker, A.J. Harding, J.M. Badcock, S.H. Harder and C.M. Rosa, 2013, Borehole-explosion and air-gun data acquired in the 2011 Salton Seismic Imaging Project (SSIP), southern California-Description of the survey: U.S. Geological Survey Open-File Report 2013-1172, 83pp., http://dx.doi.org/10.3133/ofr20131172.

White, R., and D. Mckenzie, 1989. Magmatism at rift zones: The generation of volcanic continental margins and flood basalts, *J. Geophys. Res*., 94, 7685-7729.

Whitmarsh, R. B., G. Manatschal, and T. A. Minshull, 2001. Evolution of magma-poor continental margins from rifting to seafloor spreading, *Natrue*, 413, 150-154.

Chapter 2

Seismic imaging of the metamorphism of young sediment into new crystalline crust in the actively rifting Imperial Valley, California*

Abstract

Plate-boundary rifting between transform faults is opening the Imperial Valley of southern California, and the rift is rapidly filling with sediment from the Colorado River. Three 65-90 km long refraction seismic profiles across and along the valley, acquired as part of the 2011 Salton Seismic Imaging Project, were analyzed to constrain upper crustal structure and the transition from sediment to underlying crystalline rock. Both first arrival travel-time tomography and frequency-domain full-waveform inversion were applied to provide P-wave velocity models down to ~7 km depth. The valley margins are fault-bounded, beyond which thinner sediment has been deposited on pre-existing rocks. Velocity increases continuously from ~1.8 km/s in sediment at the surface to ~6 km/s in crystalline rock with no sharp discontinuity in the valley, indicating a gradational transition. The vertical gradient in velocity decreases at ~4 km/s. Borehole data shows progressive metamorphism of young sediment into crystalline rock. The vertical change in seismic velocity gradient coincides with changes in the gradients in porosity and density of borehole core samples, but not a metamorphic facies boundary. This occurs at ~3 km depth in most of the valley, but at only ~1.5 km depth in the Salton Sea geothermal field where the heat flow is highest. Meta-sedimentary rock with velocity >5.5 km/s occurs at ~6 km depth in most of the valley but only ~3 km depth in the Salton Sea geothermal field. We interpret progressive metamorphism caused by the rift valley's high heat flow to be creating new crystalline crust throughout the valley at a rate comparable to the 2 km/Myr sedimentation rate.

The crystalline crust newly formed by metamorphism extends to at least 7-8 km depth. Active seismicity occurs entirely within this new crust.

Keywords: active rifting, crustal structure, metamorphism, Salton Trough, seismic tomography, controlled-source seismic

* An edited version of this chapter will be submitted to *Geochemistry, Geophysics, Geosystems*. Han. L., J. A. Hole, J. M. Stock, G. S. Fuis, J. R. Delph, K. Davenport, and A. J. Livers, Seismic imaging of the metamorphism of young sediment into new crystalline crust in the actively rifting Imperial Valley, California.

2.1 Introduction

The Salton Trough is an active sediment-filled rift basin, at the northern end of the Gulf of California extensional province (Figure 2.1) [e.g., *Elders et al.*, 1972; *Lonsdale*, 1989; *Stock and Hodges*, 1989; *Larsen and Reilinger*, 1991]. It is being formed by extension between the plate-bounding right-lateral San Andreas (SAF), Imperial (IF), and Cerro Prieto transform faults. The Imperial Valley (Figure 2.1) is the most active part of the Salton Trough, characterized by high heat flow, volcanic and geothermal activity, and seismicity. It is almost entirely below sea level; the elevation of the Salton Sea is -70 m. The heat flow in most of the Salton Trough is between 100 and 200 mW/m^2 (Figure 2.1) [*Lachenbruch et al.*, 1985], much larger than the mean global heat flow of 80 mW/m^2. In the Salton Sea Geothermal Field in the northern Imperial Valley, heat flow exceeds 600 mW/m^2 in an arcuate zone ~4 km wide and ~12 km long [e.g., *Helgeson*, 1968; *Newmark* et al., 1988], roughly parallel to the five small Late Quaternary volcanic domes at the southern shore of the Salton Sea [e.g., *Robinson et al.*, 1976; *Schmitt and Vazquez*, 2006]. Significant seismicity occurs at ~3-10 km depth in the oblique Brawley Seismic Zone (BSZ) [*Johnson*, 1979; *Lin et al*., 2007], which connects the San Andreas Fault and the Imperial Fault.

In the Salton Trough, the bulk of the sediment and sedimentary rock is originally transported by the Colorado River from the Colorado Plateau [*Muffler and Doe*, 1968; *Herzig et al.*, 1988; *Dorsey*, 2010; *Dorsey and Lazear*, 2013]. The lithology from boreholes is dominantly lacustrine shale, with lesser siltstone, sandstone and anhydrite. Mineralogy is consistent throughout the basin. Coarser alluvium derived from adjacent ranges is interbedded at the edges of the valley. *Larsen and Reilinger* [1991] suggested a recent regional subsidence rate of 3 mm/yr from leveling data in the northern Imperial Valley. *Schmitt and Hulen* [2008] argued that

the sedimentation rate accelerated towards the center of the Salton Trough, increasing from 2.2 mm/yr to 3.8 mm/yr. However, the subsidence to the west of the Salton Trough is generally more moderate (~0.5 mm/yr) since ~8.0 Ma [*Dorsey et al*., 2007]. Mineralogy changes systematically with depth, interpreted to be related to temperature and progressive metamorphism of the sediment, not changes in the source of the sediment [*Muffler and White*, 1969; *McDowell and Elders*, 1980; *Cho et al*., 1988; *Shearer et al*., 1988]. Greenschist facies metamorphism of the sediment is observed in wells throughout the valley, and amphibolite grade is observed at ~3 km depth within the Salton Sea geothermal field.

Numerous regional three dimensional seismic models have been build to study earthquake hazards [e.g., *Magistrale et al*., 1992; *Magistrale et al*., 2000], but earthquake network data do not well constrain shallow structure in the valleys. Structure of the Imperial Valley in the upper few km was best studied by *Fuis et al*. [1984]. They interpreted the shallowest crystalline rock as metamorphosed sediment, based on low seismic velocity and a lack of basement seismic reflection. The Salton Sea Scientific Drilling Project (SSSDP) [*Elders and Sass*, 1988] drilled State Well 2-14 (Figure 2.1), which provides important constraints to tie lithology to geophysical observations in the Salton Sea geothermal field [*Daley et al*., 1988; *Paillet and Morin*, 1988; *Tarif et al*., 1988].

The Salton Seismic Imaging Project (SSIP) acquired new active source seismic data in the Salton Trough in 2011. The objective of this paper is to study the transition from sediment to crystalline rock in the Imperial Valley by seismic imaging from part of this dataset. The seismic velocity models are correlated with borehole and heat flow observations.

2.2 Seismic Data

2.2.1 Data Acquisition

Seven refraction/wide-angle reflection profiles and two 3-D seismometer grids were acquired along and across the Salton Trough by SSIP in 2011 (Figure 2.1). Both inline and offline shots were recorded to provide three-dimensional data coverage. The recording systems were mostly single-component "Texan" (Ref Tek 125a) seismographs with geophone corner frequency of 4.5 Hz. Three-component 4.5 Hz geophones and RT130 (Ref Tek 130) seismographs were deployed every ~1 km along Line 2. In total, 2781 land seismometers, with spacing as dense as 100 m, were deployed at over 4200 sites. A total of 126 contained explosive shots of 3-1400 kg were fired during the survey. Details about data acquisition are described by *Rose et al.* [2013].

In the Imperial Valley, 3 seismic lines were recorded, two of which went through the volcanic and geothermal field. In order to study the transition from sediment to basement in this basin, only the valley and near-valley portions of those 3 seismic profiles are used in this study (Figure 2.1). Twenty shot gathers were analyzed along the ~65-km long portion of Line 1 in the Valley. This line is parallel to the transform faults and relative plate motion direction (Figure 2.1). Most shots were 115 kg, but a few were up to 1367 kg. Those shots were recorded by 574 seismographs in the Imperial Valley at a spacing of ~100 m. There were 18 shots and 776 seismographs along the ~90-km long valley portion of Line 2, oriented approximately perpendicular to the Imperial Fault (Figure 2.1). The receiver interval was 100 m in the west and middle of this line segment, but ~200 m in the eastern third. The shot size was 115 kg in general, except the shot at the Imperial Fault was 911 kg and the shot to the east of the valley was 592 kg. The ~67 km-long portion of Line 3 consisted of 16 shots and 429 seismographs. This line crossed the valley perpendicular to the transform faults and along the Salton Sea Geothermal

Field very close to the volcanic domes (Figure 2.1). On each side of the valley, 2 shots of >400 kg were fired, while in the valley, the shot size was either 115 kg or 229 kg. The receiver interval was ~500 m in the western third of Line 3, 100 m in the valley, and 300 m to the east of the valley. Although larger shots were fired outside of the valley, the signal recorded from these shots by the receivers inside the valley was poor. This also occurred during the seismic survey of *Fuis et al.* [1984], and is probably caused by local geologic structure.

2.2.2 Data Description

Several shots along Line 1 will be shown in Chapter 3, which presents the whole crustal structure of Line 1. Shot 10931 recorded along Line 1 in the northern Imperial Valley (Figure 2.2) illustrates the seismic phases that were observed throughout most of the valley. The inverse of the slope of the seismic arrivals indicates the apparent seismic velocity, which gradually increases from slow sediment near the surface (phase A) to turning (continuously refracted) waves with velocities of crystalline rock (phase B). The boundary between A and B is gradational and does not exhibit a sharp change in apparent velocity. No seismic reflection from the base of sediment is observed in data filtered at any frequency. Phases C were interpreted as multiple basin reverberations by *McMechan and Mooney* [1980] and *Fuis et al.* [1984]. The first arrival (phases A and B) is symmetric on both sides of the shot, which indicates a nearly one-dimensional structure. Close to the Salton Sea geothermal field at the southern shore of Salton Sea, the phase B arrives much earlier than that to the south, which indicates shallower rock. Deeper crustal phases, such as the Moho reflection PmP and Moho refraction Pn, are observed in the valley at distances greater than 40 km and 80 km respectively, but are not shown in this paper. Arrivals similar to those of Figure 2.2 are observed on all shots on Line 1 and nearby

portions of Lines 2 and 3. The data along Lines 2 and 3 have relatively larger variation, due to crossing the Imperial Fault and extending beyond the edges of the Imperial Valley (Figure 2.1).

Shot 21130 near the western edge of the valley shows a strong contrast in phases observed to the west and east of the shot (Figure 2.3). To the east, the first arrival (phases A and B) and basin reverberations (C) are very similar to those of Line 1 shots (Figure 2.2). In contrast to the west, the crystalline-rock phase B arrives much earlier, the velocity increase from A to B is much sharper and the basin reverberation is much weaker. This shot and other shots to the west indicate a shallower basin, a sharper sediment-rock boundary, and a faster crystalline-rock velocity west of this shot. The two eastern-most shots on the Line 2 segment display similar features. Also different from Line 1 shots, a reflection phase D is observed on Line 2 at offset >20-22 km for shot-receiver midpoints west of the Imperial Fault (Figure 2.3 recorded to the east and Figure 2.4 recorded to the west along a reversed path). A similar phase was observed nearby by *Fuis et al.* [1984]. It is interpreted to be caused by a mid-crustal reflector. Phases A and B are not exactly symmetric in shots near the Imperial Fault, but are very similar (Figure 2.4). Basin and shallowest crystalline-rock structure are therefore similar. Deeper structure (reflector D), however, is different across the Imperial transform fault at this latitude, representing two different rift segments. Modeling of this reflector is beyond the scope of this paper, which focuses primarily on the Imperial Valley rift segment.

Shots inside the valley on Line 3 are similar to those on Line 1 (Figure 2.5). Similar to Line 2, differences are observed as the line leaves the central valley. At the west end of the line, granitic bedrock is exposed at Superstition Mountain (F in Figure 2.5). The basin to the west of these mountains is poorly constrained by few shots, but is shallower than in the main valley. The easternmost two shots observe a shallow basin, a sharp sediment-rock boundary, and faster

crystalline rock velocity, similar to the east end of Line 2. A diffraction G is observed at offset ~25 km, which will be discussed in section 2.3.3. Between F and G, phases A and B are very similar to the rest of the valley, with one exception: phase B occurs ~0.5 s earlier than the rest of the valley within the Salton Sea geothermal field. The geothermal field is visible in the shot gathers as a region with higher industrial noise (7 to 18 km in Figure 2.5). And the noise at 20 to 25 km offset is mainly caused by highway traffic. Earlier arrival times for phase B indicate shallower crystalline rock beneath the volcanic and geothermal field, but the transition from phase A to B is gradational, similar to the rest of the valley.

2.3 Travel-Time Tomography

2.3.1 Method

First arrivals were picked manually on all the shot gathers in Promax, as shown in Figure 2.6a. The estimated accuracy of those picks is below half period of the dominant signals, which is about 40-50 ms within the offset range of this study. This represents an upper limit rather than mean value of the picking uncertainty. The picking error could be much lower for data with good signal noise ratio, especially for the primary offset range (<30 km) in this study. Those first arrivals were inverted using the travel time tomography procedures described below.

Hole [1992] and *Zelt et al.* [1996] developed a three dimensional (3D) tomographic inversion procedure from the finite difference calculation of travel time by *Vidale* [1990]. This code tracks rays in a 3D velocity volume, but assuming there is no lateral variation in the direction perpendicular to the seismic profile. The misfit of each pick is evenly distributed along the whole ray path, and the velocity perturbation in a certain grid is calculated from the mean misfit of all the rays traveling through that grid. If the receivers are unevenly spaced, a weighting

parameter is applied in this process. Then, a moving average filter is applied to smooth the velocity perturbation before it is added to the previous velocity model. This procedure repeats as an iteration to generate a new 3D velocity model. The smoothing size of the moving average filter gradually gets smaller as the iterations proceed, but the ratio between the horizontal and vertical size of the moving average filter is kept the same. The velocity model is finalized when the smoothing size approaches the model resolution limited by the shot interval. The grid size used in this study is 100 m.

The starting model for travel time tomography is a smooth 1D velocity model, fitting all the first arrival picks. For example, the 1-D starting velocity model in Figure 2.6b was inverted from all the first arrival travel times of Line 1. The horizontal smoothing was set large enough to keep the model 1-D, and the vertical smoothing was ~1 km. This simple 1D model produces travel times that approximate the average observed times from all of the shots (Figure 2.6a). For Lines 2 and 3, the 1D starting model was derived using data only from the central basin, which is the focus of this paper. Strong velocity contrasts at shallow depth on the valley margins are more dependent upon the starting model and less well constrained by sparser shots, but were not the primary focus here.

2.3.2 Velocity Models and Resolution

The resulting seismic velocity models and ray coverage are shown in Figures 2.7 to 2.9. The final tomography horizontal smoothing of Lines 1 and 3 is 2.5 km, which is roughly the average shot interval, and the vertical smoothing is 0.5 km. Line 2 is smoothed to 3.6 by 0.7 km due to the sparser average shot spacing. The spatial resolution of the final velocity models approximates the smoothing size used, which is limited by the shot and receiver interval. A

smaller smoothing size may result in a better spatial resolution and a smaller data misfit, but with increasing artifacts caused by noise or picking uncertainty.

The ray coverage is very dense and crosses at multiple angles in the center of the models, providing strong constraints on the velocity structure. At the bottom and edges of the models, ray coverage is sparser and mostly parallel to the boundaries, allowing for smearing of structure along these directions. The root-mean-square (RMS) travel time misfit is within the picking accuracy of about a half-cycle (Figure 2.10). The RMS misfit of Line 3 is calculated from the valley portion only. The misfit in the western end of Line 3 is up to ~100 ms because of irregular topography, sparse stations, and lower data quality.

2.3.3 Features of the Velocity Models

For Line 1, which is oriented northwest-southeast parallel to the relative plate motion direction, the velocity structure is almost 1-D (Figure 2.7a). The velocity gradually increases from ~1.8 km/s at the surface to ~6 km/s at ~7 km depth approaching the bottom of good ray coverage. The 4 km/s contour is nearly flat at ~3 km depth along the Imperial Valley. This velocity is typical of a well-lithified low-porosity shale or sandstone. The vertical velocity gradient below 3-4 km depth is much smaller than that near the surface (Figures 2.7a, 2.13, and 2.14). There is no evidence of a steepening in the gradient that might indicate a smoothed discontinuity. Velocity of 5.5 km/s, a rough proxy for crystalline metamorphic or igneous rock, is at ~6.0 km depth in the northern Imperial Valley, and gradually deepens to ~7.0 km depth to the south. The initiation of deepening corresponds roughly with the southern end of the Brawley seismic zone. Fracturing in the seismic zone might be expected to reduce velocity, yet slightly higher velocity is observed at a given depth in the seismic zone. Instead, deeper high velocity

corresponds to both proximity to the mouth of the Colorado River and to slightly lower heat flow. Higher velocity occurs at much shallower depth beneath the SSGF and Obsidian Butte volcanic dome. This structure near the edge of the model is not well constrained on Line 1, but is well resolved by Line 3. A small high in the 2.5-4.5 km/s contour occurs at model km 21, at the smaller Brawley geothermal field. Deeper contours are uplifted a little to the south.

The west-east Line 2 crosses the center of the Imperial Valley and the northern end of the Imperial Fault, approximately perpendicular to Line 1. The deep sedimentary basin is ~60 km wide along this profile, with the deepest part near the Imperial Fault (Figure 2.8). Similar to Line 1, seismic velocity continuously increases in the deep basin, with a similar change in velocity gradient. The velocity structure is nearly identical to Line 1 at the intersection of the lines, except near the bottom of ray coverage at >6 km depth and >5.6 km/s velocity (Figures 2.8 and 2.13). Line 2 has sparser shots than Line 1, and shots outside the central valley are of poorer quality, so Line 1 probably has better constraints at 6-7 km depth. Neither line is well constrained below ~7 km depth. There is a subtle deflection of the contour lines across the Imperial Fault, which may be smaller than can be resolved. Resolution of the margins of the deep basin is affected by the shot spacing and the tomography smoothing, such that lateral resolution is 3-4 km. Velocity contours rise slowly towards the eastern side of the basin, then rise sharply, consistent with a steep fault at model km ~80. This basin margin is east of the southeastern extrapolation of the San Andreas Fault. In the western valley, the contours are consistent with a steep fault at model km ~19. These structures define a complex western margin of the Cerro Prieto rift, west of the transform Imperial Fault.

Line 3 extends southwest-northeast along the southern shore of the Salton Sea, along the axis of the geothermal field. The basin is about 45 km wide along this profile, with the deepest

part near the western margin (Figure 2.9). The basin boundaries are consistent with steep faults, with the western margin at or west of the Superstition Hills fault, and the eastern margin consistent with the along-strike extension of the Sand Hills Fault. Similar to the other lines, velocity within the main basin increases continuously with depth, with a change in gradient. However, the velocity gradients are much larger within the Salton Sea geothermal field, and high velocity occurs at much shallower depth (Figures 2.9 and 2.15). This is also observed along Line 1 (Figure 2.7a), but it is better constrained along this profile. The diffraction phase G in Figure 3.5 is caused by multi ray paths off the edge of the shallow crystalline rock at distance ~50 km. In the basin, the velocity model is only well constrained to ~5 km depth and <5.6 km/s. Compared to Line 2, the basin is much narrower at this location, which limits the maximum recording offset and the imaging depth of the basin.

Travel-time tomography with smoothing successfully matches the data (e.g., Figure 2.10), but produces a model that is as smooth as possible. A sharp velocity discontinuity will be imaged as a broad zone with high velocity gradient by travel time tomography because of smoothing. There is no evidence within the velocity models for a velocity gradient higher than the background values at any depth (Figures 2.7 to 2.9). In addition, no strong reflectors are observed in the data (Figures 2.2 to 2.5). This suggests that no velocity discontinuity, such as a depositional surface between sediment and bedrock, exists.

2.4 Full-Waveform Inversion

To improve the vertical resolution and to test for the existence of discontinuities, full-waveform synthetic seismograms were computed for representative data in the central Imperial

Valley. Full-waveform inversion was then applied to the northern half of Line 1, where the shots are closest together.

2.4.1 Synthetic Seismograms

The full-waveform inversion algorithm of *Pratt* [1999] computes synthetic seismograms in a gridded 2-D velocity model using a finite-difference approximation of the acoustic wave equation in the frequency domain. Synthetic data were computed at 2-10 Hz in the northern half of the travel-time tomography model of Figure 2.7. The synthetic data successfully reproduce the first arrivals and strong basin reverberations with time similar to the real data. These reverberations were not included in the tomography, so their reproduction in the synthetic data provides confidence in the velocity model, and in particular in the strong velocity gradient in the near-surface.

2.4.2 Inversion Method

The full-waveform tomography algorithm of *Pratt* [1999] inverts phase and amplitude of seismic data in the frequency domain. An excellent starting model, accurate to within a half-period of the frequencies being inverted, is required for convergence. *Brenders and Pratt* [2007a, 2007b] demonstrate that a starting velocity model derived from first-arrival travel-time tomography works well for long-offset refraction and reflection data. An approach that progressively inverts from low to high frequency stabilizes the inversion by producing more detailed starting models for inversions at higher frequency.

Land crustal seismic refraction and wide-angle reflection data are usually acquired along crooked roads, which makes 2D full waveform inversion difficult. Due to the crooked SSIP line (Figure 2.1), an approximate 2-D geometry was used following *Smithyman and Clowes* [2012].

Similar to the travel-time tomography, the velocity and attenuation models are assumed to be homogeneous in the direction perpendicular to the average seismic line. Shots and receivers are projected to the straight line, and the seismic waveforms are corrected using a time shift determined by 3D ray tracing, which accounts for the cross line offsets produced by the crooked-line acquisition.

Densely spaced shots and receivers are required for full-waveform inversion to converge. At least one of the two domains must not be spatially aliased. The minimum velocity in the Imperial Valley is >1.6 km/s, and the receiver interval is ~100 m, so 8 Hz is the highest frequency that is not spatially aliased. The lowest frequency observed in the SSIP data is 2 Hz, so the data were inverted from 2 to 7 Hz. *Brenders and Pratt* [2007b] showed that full-waveform inversion can work if the shots are spatially aliased, but only up to a limit. The northern 30 km of Line 1 along the northern Imperial Valley has the densest shot spacing. Unfortunately, two shots could not be used because the existing software does not accept the different station spacing recorded by those shots. The remaining shots are spaced ~2.5 km on average, and ~7 km at most. The lowest frequency in our dataset is ~2 Hz, from which the inversion starts. So the Δ_{samp} is as low as 0.4 km, where the full wavelength is 0.8 km for the minimum velocity of 1.6 km/s at 2 Hz. The ratio $\Delta s/\Delta_{samp}$ calculated for this study is ~6.25. *Brenders and Pratt* [2007b] showed that the image quality remains acceptable provided this ratio is less than 3, and accurate images can be obtained in the central portion of the model when the ratio is around 7, but the images suffer from some degradation. Additional challenges are the irregular shot spacing and realistic noise in the data. *Bleibinhaus et al.* [2009] discuss methods required for the inversion of real long-offset data with non-ideal shot spacing. They showed that the inversion of only the phase of the frequency-domain data is more stable, so the SSIP inversion ignored amplitude. The inversion is

thus similar to the finite-frequency inversion method, but it uses the windowed waveform including multiple arrivals in the frequency domain rather than the travel time of a narrowly windowed single arrival. Data pre-processing included removal of noisy data traces and bandpass filtering. Large-amplitude surface waves and S waves were muted from the data, as they are not included in the acoustic-wave synthetic data.

2.4.3 Inversion of Synthetic Data

In order to test whether full waveform inversion enables improved imaging, a synthetic dataset was produced using the same shot and receiver geometry as the real data and a similar geological structure. The synthetic velocity model (Figure 2.10a) was created by adding a sharp boundary with a velocity contrast from 4 km/s to 5 km/s to the real travel-time velocity model (Figure 2.7). Noise-free acoustic data with frequency of 0.1-10 Hz were computed by finite differences in the frequency domain. Full-waveform inversion was applied to these data. The starting model was derived from first arrival travel-time tomography, using travel-times calculated from the synthetic velocity model. The sharp boundary was fully smoothed and did not exist in this starting model. The evidence for the boundary in the synthetic seismic data is a sharper change in slope of the first arrival and a secondary reflection arrival, neither of which is detected in the real data.

The synthetic data were pre-processed in the same manner as would be used for the real data. The near offset data were muted to remove surface waves and very high amplitudes. The amplitude generated by real shots is quite different from that modeled by the acoustic wave equation, especially at near offset. The remaining data were windowed for 3 s after the first arrivals. The data were then filtered by a high-pass minimum-phase Ormsby filter with

frequencies of 0-0-f1-f2, where frequency f1 is 0.5 Hz lower than frequency f2. Three frequencies were selectively selected for f2, which are 3, 5 and 8 Hz. After that, the amplitudes of the filtered data were corrected by synthetic waveforms, which were forwarded up to the frequency f2 from the current best velocity model. After the data preparation, the inversion was iteratively performed on a single frequency each time, progressing gradually from 2 to 7 Hz (Table 2.1). The inversion for each higher frequency used the velocity model from the previous inversion as the starting model. For each frequency, the source signature was inverted first from the most recent velocity model and used in the inversion for the new velocity model. Inversion for each frequency required 8 iterations, and only the phase of the data are inverted. The cost function reduction is shown in Table 2.1.

The velocity model after full-waveform inversion of 2-7 Hz data successfully sharpened the velocity contrast at the correct depth (Figure 2.10). Although oscillations common from waveform inversion were produced, the results closely resemble the true synthetic model. The image quality is best at model distances of 8-14 km and 28-34 km, which are beneath the densest shots. This shows that full waveform inversion can improve images for the geometry of the SSIP experiment, and the sharp boundary in the upper crust should be imaged by full-waveform inversion if it exists.

2.4.4 Inversion of SSIP Data

The same procedure and parameters (Table 2.1) were applied to the real SSIP data. The starting velocity model was the first-arrival travel-time tomography model from Figure 2.7. (Figure 2.11a). Short-offset data, bad seismic traces and a very noisy section of the dataset were muted. The remaining data were windowed for 3 s after the first arrivals. The waveform-

inversion model closely resembles the travel-time inversion velocity model, except for the high velocity below 2.5 km depth at distance 14-25 km. This part of the model is not as well constrained by the sparse shots above it, as suggested by the synthetic study, so is interpreted as an artifact. Other than that feature, the contours of 3 to 5 km/s are consistent before and after waveform inversion. According to the synthetic study, the portions of the model with the best image quality are at distances 8-14 km and 28-34 km, beneath the densest shots. Vertical profiles at these locations have short-wavelength oscillations about the starting model but show no evidence for a sharp contrast (Figure 2.14). No evidence for a velocity discontinuity with depth is imaged by full waveform inversion. The transition from sediment to crystalline rock has to be gradual.

2.5 Metamorphism of Sediment

2.5.1 Seismic Evidence

The seismic velocity throughout the Imperial Valley increases continuously with depth from <2 km/s in surface sediment to >5.5 km/s typical of crystalline rocks (Figures 2.7 to 2.9 and 2.13 to 2.15). The high-quality seismic data are capable of detecting a sharp vertical velocity contrast, but such a discontinuity is not detected by a seismic reflection arrival nor by full waveform inversion. The mineralogy in geothermal energy and research boreholes indicates progressive metamorphism of Colorado River sediment with depth resulting from the valley's high geothermal gradient [e.g., *Muffler et al*., 1969; *McDowell and Elders*, 1980; *Cho et al*., 1988; *Shearer et al*., 1988]. A previous seismic refraction study with several sparsely sampled lines also observed a lack of seismic bedrock reflector and a low crystalline-rock velocity, and interpreted shallow crystalline rocks within the Imperial Valley to be metamorphosed sediment

[*Fuis et al.*, 1984]. The SSIP data provide higher-resolution seismic images that support this interpretation.

Beyond the margins of the deep basin, sediment is much thinner and the seismic shots are sparser. The data for shots beyond the basin margins clearly show a much sharper velocity contrast from <3.5 km/s to ~6 km/s (e.g., west side of Figure 2.3). The starting velocity model and smoothing used for the tomography do not ideally image the shallow sediment-rock transition outside the deep basin. However, the data are most consistent with 0-2 km of sediment deposited on pre-existing felsic crystalline bedrock.

Throughout the Imperial Valley, the vertical velocity gradient deeper than ~4.5 km/s is much smaller than that above ~4.0 km/s [Figures 2.7 to 2.9 and 2.13 to 2.15]. The velocity gradient at shallow depth varies within the valley from 0.8 s^{-1} up to 2 s^{-1}, such that ~4 km/s occurs at variable depth. This depth strongly correlates with heat flow (Figure 2.1) [*Lachenbruch et al*., 1985]. At greater depth, the gradient is a much lower 0.4-0.5 s^{-1} to almost 6 km/s. The transition zone is 0.5-1 km thick between these two gradients along line 1 and the central valley portions of lines 2 and 3. Towards the western margin of the deep basin along line 3 and both margins along line 2, the velocity gradient changes more gradually, but a strong change is still observed. The true change in gradient may be more gradational at these locations, or resolution might be worse because of sparser shots and lateral smearing of the basin margins.

2.5.2 Correlation with Borehole Observations

The State 2-14 well of the Salton Sea Scientific Drilling Project [*Elders and Sass*, 1988] is located <0.5 km from seismic Line 3, which makes it feasible to correlate the seismic velocity model with observations from this borehole (Figure 2.15). This research borehole penetrated

3.22 km of Pleistocene to Holocene sediment and meta-sedimentary rock in the Salton Sea geothermal field. Temperature in the borehole was 300˚C at 1700 m (Figure 2.15e) [*Sass et al.*, 1988]. Sedimentary layering and bulk composition are preserved throughout the borehole and are consistent with a Colorado River source, but the sediment is progressively metamorphosed as temperature increases with depth [*Cho et al.*, 1988; *Shearer et al.*, 1988]. Three major metamorphic zones are observed from core samples (Figure 2.15a): a chlorite-calcite (chl-cc) zone, biotite (bt) zone, and clinopyroxene-amphibole (cpx) zone. Epidote is formed beneath 0.9 km depth, at ~250˚C. The chl-cc zone beginning at <0.6 km depth represents greenschist facies metamorphism and the cpx zone at ~3.0 km depth and ~325˚C marks the low-pressure transition from greenschist to amphibolite facies. The rocks are progressively lithified similar to diagenesis, but without the formation of zeolite. A regional 770 ka tuff is observed in the well at 1.7 km depth [*Herzig and Elders*, 1988; *Schmitt and Hulen*, 2008], indicating rapid metamorphism of very young sediment. Metamorphism is driven primarily by the effects of temperature and hydrothermal fluids.

Seismic velocity measured in the borehole and from core samples [*Daley et al.*, 1988; *Paillet and Marin*, 1988; *Tarif et al.*, 1988] is consistent with the seismic velocity model from Line 3 (Figure 2.15b). The change in velocity gradient at 1.6-2.1 km depth occurs within the chl-cc metamorphic zone, and does not correlate with any metamorphic facies boundary or major mineral occurrence (Figure 2.15). It does, however, correlate with a change in gradient in the density and porosity of core samples (Figure 2.15d) [*Tarif et al.*, 1988] and in the electrical resistivity log [*Paillet et al.*, 1988]. Most of the porosity is sedimentary matrix porosity, not fractures. Porosity decreases rapidly within the chl-cc zone, from >20% to ~5%, due to calcite precipitation, crystal overgrowth, and metamorphism of clays to feldspars and epidote. Once

porosity reaches ~5%, metamorphism continues with depth, but porosity is closed much more slowly. The top of the change in gradient in seismic velocity is interpreted to be due to the change in gradient in porosity and density, not to the minerals present. This occurs at a velocity of ~4.4 km/s, which is typical of a well-cemented, low-porosity shale or sandstone. This porosity is very high and seismic velocity is very low for a greenschist facies meta-sedimentary rock, probably due to the shallow depth and rapid rate of metamorphism.

The same metamorphic mineralogy is observed in geothermal wells throughout the Imperial Valley [e.g., *Muffler et al*., 1969; *McDowell and Elders*, 1980]. The metamorphic reactions are observed at different depths due to different heat flow, but at very similar temperatures. The Elmore 1 well within the geothermal field near line 3 has much higher temperature (361˚C at 2169 m depth), the metamorphic zones are shallower, and garnet is created near the bottom of the well [*McDowell and Elders*, 1980]. A change in porosity gradient at porosity ~5%, very similar to the State 2-14 well, occurs at ~1.1 km depth, but near the bottom of the chl-cc zone.

Metamorphic mineralogy is available for few wells outside the geothermal field, where the heat flow is much lower but still much higher than normal continental values. The deep Wilson No. 1 well at the intersection of Lines 1 and 2, with a temperature more typical of most of the valley (~260˚C at 4.1 km depth), observed the same metamorphic reactions at approximately the same temperatures (Figure 2.13a) [*Muffler et al*., 1969]. Due to lower temperature, epidote and the biotite zone were not observed. Porosity was mostly closed at an unreported depth within the chl-cc zone. Seismic velocity at this location is lower than in the geothermal field, and the change in velocity gradient occurs almost twice as deep at ~2.8 km depth, where the velocity is a very similar 3.9 km/s (Figure 2.13). This depth is within the chl-cc

zone, but at lower metamorphic facies within the zone. The change in velocity gradient is interpreted to be due to a change in porosity gradient at ~5% porosity similar to that observed in the State 2-14 well. Rapid closure of porosity always occurs within the chl-cc zone, indicating that metamorphism plays a role. However, at greater depth, it occurs at a lower temperature within the chl-cc zone. This suggests that while pressure plays only a minor role in the metamorphic mineralogy, metamorphism and pressure work together to close porosity.

2.5.3 Depth and Extent of Meta-sedimentary Crust

The top of the sharp decrease in seismic velocity gradient is interpreted to be the depth where rapid closure of porosity ends, at roughly 5% porosity. This depth was measured along all of the seismic lines (Figure 2.17). Even though the depth changes along the lines, it occurs at a fairly consistent velocity of ~4.1 km/s. Where the change in velocity gradient is as not sharply defined, this velocity was used as a proxy. At this depth (Figure 2.17), we interpret a greenschist-facies meta-sedimentary rock with ~5% porosity due to rapid metamorphism at shallow depth. This "boundary" is in fact gradational due to progressive metamorphism with depth. The shallowest depth for this velocity-gradient boundary is 1.2-1.6 km in the Salton Sea geothermal field along Line 3 and at the northern end of Line 1 (Figure 2.17), where the heat flow exceeds 600 mW/m^2 [*Helgeson et al*., 1968; *Newmark et al*., 1988] and the wells tie velocity gradient to density gradient. This geothermal field, however, is sharply bounded, and most of the rest of the valley has much lower heat flow of 100-200 mW/m^2, averaging ~140 mW/m^2 [*Lachenbruch et al.*, 1985]. For most of the valley, the depth of the velocity-gradient boundary is about twice as deep, at ~2.8 km depth, and it is very flat along the axis of the valley on Line 1 (Figure 2.17). Velocity of <4.5 km/s and the gradient boundary are slightly shallower near the North Brawley geothermal field, at model km ~20 on Line 1, and also shallower at the east end of line 2, near

the East Brawley geothermal field. No contrast is observed across the Imperial Fault, even though this transform fault bounds two different rift segments. The deepest boundary is along the western portion of Line 3, which extends west of the northwest extrapolation of the Imperial fault. This area lies outside the main rift. The velocity-gradient boundary is difficult to define near the margins of the valley due to sparser shots, shallower ray coverage, and lateral smoothing of the tomography model. It may not turn shallower as shown in Figure 2.17.

The above porosity-gradient boundary represents a metamorphic rock with high porosity and low seismic velocity atypical of traditional deeper metamorphism. Like the seismic velocity, the brittle strength of this rock is probably similar to a strong sedimentary rock. A seismic velocity of 5.5 km/s is used as a rough proxy for stronger crystalline rock (Figure 2.17). Beneath the deep basin, this proxy is not an actual boundary, but lies within continuing metamorphism of the meta-sedimentary rock. In general, the shape of this velocity contour mimics the shallower velocity-gradient boundary at about twice the depth. Strong crystalline rock is at <3 km depth beneath the Salton Sea geothermal field, and at ~6 km depth in most of the rest of the valley. It is slightly deeper at the southern end of the Imperial Valley. This means slower velocity or deeper high velocity outside the Brawley Seismic Zone, which is the opposite trend compared to what is expected of fracturing. Instead, this greater depth could be due to lower heat flow or to faster sediment deposition near the mouth of the Colorado River. Crystalline rock is also deeper beneath the western end of Line 3, which is a complex region of plate motion transfer between the Imperial Fault and San Jacinto and San Andreas Faults.

At the eastern and western margins of the valley along Lines 2 and 3, the seismic data indicate thinner sediment, a sharp sediment-rock boundary, and faster crystalline-rock velocity of ~6 km/s immediately beneath the sediment. These are interpreted as evidence for sediment

deposition on pre-existing crystalline crust outside the main rift valley. The margins of the deep basin are smeared by tomographic smoothing and in some places sparser shots, but are consistent with steep faults. The western boundary along Line 2 is consistent with a steep fault at model distance ~20 km , near shot 21130 (Figures 2.3, 2.8). This location approximately corresponds to the northwest extrapolation of the Cerro Prieto Fault in Mexico, the next active transform fault to the south of the Imperial Fault. It may be the inactive western boundary of the Cerro Prieto rift segment, analogous to an oceanic fracture zone.

The western boundary along Line 3 is poorly defined due to sparse shots. It lies east of the Superstition Mountains, which expose granitic basement, and may be as far east as the Superstition Hills Fault (Figures 2.9). The steepness of this boundary is poorly defined. The basin is very thick near this boundary, even though it is west of the along-strike extension of the Imperial Fault. This deep basin probably represents extension related to the complex distribution of extension from the Imperial Fault to the San Jacinto and San Andreas Faults. The eastern boundary of the basin is similar along lines 2 and 3 and is consistent with a steep boundary (Figures 2.8, 2.9). At Line 2, it corresponds with the Sand Hill Fault, an along-strike extension of the Algodones Fault in Mexico. The location at Line 3 is along strike with this fault. Both are east of the along-strike extension of the active San Andreas Fault. The Sand Hills Fault is thought to represent an inactive strike-slip fault that pre-dates the modern active faults.

Meta-sedimentary crust extends to at least 7-8 km depth based on smoothly increasing seismic velocity that is slower than that observed outside the basin. Based on deposition rates of ~2 km/Myr [*Schmitt and Hulen*, 2008], 8 km of sediment has been deposited in last 4 Myr. Based on longer-offset SSIP data (Chapter 3), felsic crystalline rock extends to ~13 km depth.

The entire felsic component of the crystalline crust may be metamorphosed syn-rift sediment. Alternatively, the lower ~5 km is also consistent with pre-rift granitic continental crust.

Abundant seismicity occurs at 3-8 km depth in the Salton Sea geothermal field, 5-10 km depth in most of the Brawley Seismic Zone, and 7-11 km depth beneath the Imperial fault [*Lin et al*., 2007]. These depths are accurate to 1-2 km. The shallowest seismicity is slightly deeper than the velocity gradient boundary interpreted to have a strength similar to strong clastic sedimentary rock, and is shallower than the 5.5 km/s proxy for strong crystalline rock. The brittle-ductile transition is within or only slightly deeper than the minimum depth of meta-sedimentary rock.

2.6 Conclusions

Three P-wave seismic velocity models in the Imperial Valley were generated from first arrival travel time tomography of the SSIP refraction data. The results are consistent with the previous study of *Fuis et al.* [1984], but provide more details on the basin structure and underlying crystalline rock. Velocity increases continuously with depth within the valley, with no vertical velocity discontinuity, indicating a gradational boundary between sediment and crystalline rock. This is confirmed by full waveform inversion on one of the seismic lines. Comparison with boreholes indicates that sediment within the basin is progressively metamorphosed at shallow depth by the high heat flow in the rift. Metamorphism recrystallizes the sediment into rock in a process similar to diagenesis, but at shallower depth and without the appearance of zeolite. This temperature-driven metamorphism continues with depth, producing strong, new crystalline rock. A sharp change in the seismic velocity gradient correlates with a change in the rate of closing porosity in boreholes. This change occurs within the greenschist facies, but at a porosity of 5% that is much higher than traditional metamorphism. This change in

porosity gradient occurs at ~2.8 km depth in most of the valley, but is much shallower at ~1.5 km depth in the Salton Sea geothermal field, where the heat flow is considerably greater. Velocity more typical of strong crystalline rock is observed at about twice these depths. Earthquakes occur entirely within metamorphosed syn-rift sediment. Sedimentation and high heat flow are actively creating new crystalline crust in the Imperial Valley, and that crust is strong enough for brittle seismicity related to ongoing extension.

Acknowledgments. This research was supported by NSF MARGINS and EarthScope grants 0742263 to JAH and 0742253 JMS, and by the U. S. Geological Survey's Multihazards Research Progam. We thank the >90 field volunteers and USGS personnel who made data acquisition possible. Numerous landowners allowed access for shots and stations. Seismographs and technical support were provided by the IRIS-PASSCAL instrument facility; special thanks to Mouse Reusch and Patrick Bastien from PASSCAL for their field and data efforts. Software support was provided by Landmark Software and Services, a Halliburton Company.

References

Bleibinhaus, F., R. W. Lester, and J. A. Hole (2009), Applying waveform inversion to wide-angle seismic surveys, Tectonophysics., 472, 238-248.

Brenders, A. J., and R. G. Pratt (2007a), Full waveform tomography for lithospheric imaging: results from a blind test in a realistic crustal model, Geophys. J. Int., 168, 133-151, doi: 10.1111/j.1365-246X.2006.03156.x.

Brenders, A. J., and R. G. Pratt (2007b), Efficient waveform tomography for lithospheric imaging: implications for realistic, two-dimensional acquisition geometries and low-frequency data, Geophys. J. Int., 169, 152-170, doi: 10.1111/j.1365-246X.2006.03096.x.

Cho, M., J. G. Liou, and D. K. Bird (1988), Prograde phase relations in the State 2-14 well metasandstones, Salton Sea geothermal field, California, J. Geophys. R., 93, 13081-13103.

Daley, T. M., T. V. McEvilly, and E. L. Majer (1988), Analysis of P and S wave vertical seismic profile data from the Salton Sea Scientific Drilling Project, J. Geophys. R., 93, 13025-13036.

Dorsey, R. J. (2010), Sedimentation and crustal recycling along an active oblique rift margin Salton Trough and northern Gulf of California, Geology, 38, 443-446, doi:10.1130/G30698.1.

Dorsey, R. J., and G. Lazear (2013), A post-6 Ma sediment budget for the Colorado River，Geosphere, 9, doi:10.1130/GES00784.1.

Elders, W. A., R. W. Rex, T. Meidav, P. T. Robinson, and S. Bieler (1972), Crustal spreading in southern California, Science, 178, 15-24.

Elders, W. A., and J. H. Sass (1988), The Salton Sea Scientific Drilling Project, J. Geophys. R., 93, 12953-12968.

Fuis, G. S., and W. M. Mooney, J. H. Healy, G. A. McMechan, and W. J. Lutter (1984), A seismic refraction survey of the Imperial Valley region, California, J. Geophys. Res., 89, 1165-1189.

Hauksson, E. (2000), Crustal structure and seismicity distribution adjacent to the Pacific and North America plate boundary in southern California, J. Geophys. Res., 105(B6):29.

Helgeson, H. C. (1968), Geologic and thermodynamic characteristics of the Salton Sea geothermal system, Am. J. Sci., 266, 129-166.

Herzig, C. T., and W. A. Elders (1988), Nature and significance of igneous rocks cored in the State 2-14 research borehole: Salton Sea Scientific Drilling Project, California, J. Geophys. R., 93, 13069-13080.

Herzig, C. T., J. M. Mehegan, and C. E. Stelting (1988), Lithostratigraphy of the State 2-14 borehole: Salton Sea Scientific Drilling Project, J. Geophys. R., 93, 12969-12980.

Hole, J. A. (1992), Nonlinear high-resolution three-dimensional seismic travel time tomography. J. Geophys. Res., 97, 6553-6562.

Lachenbruch, A. H., J. H. Sass, and S. P. Galanis, Jr. (1985), Heat flow in southernmost California and the origin of the Salton Trough, J. Geophys. R., 90, 6709-6736.

Larsen, S., and R. Reilinger (1991), Age constraints for the present fault configuration in the Imperial Valley, California: Evidence for northwestward propagation of the Gulf of California rift system, J. Geophys. Res., 96, 10,339-10,346.

Lekic, V., S. W. French, and K. M. Fischer (2011), Lithospheric thinning beneath rifted regions of southern California, Science, 334, 783-787, doi:10.1126/science.1208898.

Lin, G., P. M. Shearer, and E. Hauksson (2007a), Applying a three-dimensional velocity model, waveform cross correlation, and cluster analysis to locate southern California seismicity from 1981 to 2005, J. Gephys. Res., 112, B12309, doi:10.1029/2007JB004986.

Lin, G., P. M. Shearer, E. Hauksson, and C. H. Thurber (2007b), A three-dimensional crust seismic velocity model for southern California from a composite event method, J. Gephys. Res., 112, B11306, doi:10.1029/2007JB004977.

Lin, G., C. H. Thurber, H. Zhang, E. Hauksson, P. M. Shearer, F. Waldhauser, T. M. Brocher, and J. Hardebeck (2010), A California statewide three-dimensional seismic velocity model from both aboslute and differential times, Bull. Seismol. Soc. Amer., 100, 225-240, doi:10.1785/0120090028.

Lonsdale, P. (1989), Geology and tectonic history of the Gulf of California, in E. L. Winterer, D. M. Hussong, and R. W. Decker, eds., The Eastern Pacific Ocean and Hawaii, Geol. Soc. Am., The Geology of North America, vol. N, p. 499-521.

Magistrale, H., H. Kanamori, and C. Jones (1992), Forward and inverse three-dimensional P wave velocity models of the southern California crust, J. Geophys. Res., 97, 14,115-14,135.

Magistrale, H., S. Day, R. W. Clayton, and R. Graves (2000), The SCEC southern California reference three-dimensional seismic velocity model version 2, Bull. Seismol. Soc. Amer., 90, S65-S76.

McDowell, S. D., and W. A. Elders (1980), Authigenic layer silicate minerals in borehole Elmore 1, Salton Sea geothermal field, California, USA, Contrib. Mineral. Pet., 74, 293-310.

McMechan, G. A., and W. D. Mooney (1980), Asymptotic ray theory and synthetic seismogram for laterally varying structures: Theory and application to the Imperial Valley, California, Bull. Seismol. Soc. Amer., 70, 2021-2035.

Muffler, L. J. P., and B. R. Doe (1968), Composition and mean age of detritus of the Colorado River delta in the Salton Trough, southeastern California, J. Sediment. Petrol., 38, 384-399.

Muffler, L. J. P., and D. E. White (1969), Active metamorphism of upper Cenozoic sediments in the Salton Sea geothermal field and the Salton Trough, southeastern California, Geological Society of America Bulletin, 80, 157-182.

Newmark, R. L., P. W. Kasameyer, and L. W. Younker (1988), Shallow drilling in the Salton Sea region: the thermal anomaly, J. Geophys. R., 93, 13005-13023.

Paillet, F. L., and R. H. Morin (1988), Analysis of geophysical well logs obtained in the State 2-14 borehole, Salton Sea geothermal area, California, J. Geophys. R., 93, 12981-12994.

Pratt, P. G. (1999), Seismic waveform inversion in the frequency domain, part 1: Theory and verification in a physical scale model, Geophysics, 64, 888-901.

Robinson, P. T., W. A. Elders, and L. J. P. Muffler (1976), Quaternary volcanism in the Salton Sea geothermal field, Imperial Valley, California, Geol. Soc. Amer. Bull., 87, 347-360.

Rose, E.J., G.S. Fuis, J.M. Stock, J.A. Hole, A.M. Kell, G. Kent, N.W. Driscoll, M. Goldman, A.M. Reusch, L. Han, R.R. Sickler, R.D. Catchings, M.J. Rymer, C.J. Criley, D.S. Scheirer, S.M. Skinner, C.J. Slayday-Criley, J.M. Murphy, E.G. Jensen, R. McClearn, A.J. Ferguson, L.A. Butcher, M.A. Gardner, I. Emmons, C.L. Loughran, J.R. Svitek, P.C. Bastien, J.A. Cotton, D.S. Croker, A.J. Harding, J.M. Badcock, S.H. Harder and C.M. Rosa (2013), Borehole-explosion and air-gun data acquired in the 2011 Salton Seismic Imaging Project (SSIP), southern California-Description of the survey: U.S. Geological Survey Open-File Report 2013-1172, 83pp., http://dx.doi.org/10.3133/ofr20131172.

Sass, J. H., S. S. Priest, L. E. Duda, C. C. Carson, J. D. Hendricks, and L. C. Robison (1988), Thermal regime of the State 2-14 well, Salton Sea Scientific Drilling Project, J. Geophys. R., 93, 12995-13004.

Schmitt, A. K., and J. B. Hulen (2008), Buried rhyolites within the active, high-temperature Salton Sea geothermal system, J. Volcanol. Geotherm. Res., 178(4), 708-718.

Schmitt, A. K., and J. A. Vazquez (2006), Alteration and remelting of nascent oceanic crust during continental rupture: Evidence from zircon geochemistry of rhyolites and xenoliths from the Salton Trough, California, Earth Planet. Sci. Lett., 252, 260-274.

Shearer, C. K., J. J. Papike, S. B. Simon, and B. L. Davis (1988), Mineral reactions in altered sediments from the California state 2-14 well: Varations in the model mineralogy, mineral chemistry and bulk composition of the Salton Sea scientific drilling project core, J. Geophys. R, 93, 13,104-13,122.

Smithyman, B. R., and R. M. Clowes (2012), Waveform tomography of field vibroseis data using an approximate 2D geometry leads to improved velocity models, Geophysics, 77, R33-R43, doi: 10.1190/GEO2011-0076.1.

Stock, J. M., and K. V. Hodges (1989), Pre-Pliocene extension around the Gulf of California and the transfer of Baja California to the Pacific Plate, Tectonics, 8, 99-115.

Tape, C., Q. Liu, A. Maggi, and J. Tromp (2009), Adjoint tomography of the southern California crust, Science, 325, 988-992, doi: 10.1126/science.1175298.

Tarif, P. A., R. H. Wilkens, C. H. Cheng, and F. L. Paillet (1988), Laboratory studies of the acoustic properties of samples from Salton Sea Scientific Drilling Project and their relation to microstructure and field measurements, J. Geophys. R., 93, 13057-13067.

Vidale, J. E. (1990), Finite difference calculation of travel times in three dimensions, Geophysics, 55, 521-526.

Zelt, B. C., R. M. Ellis, R. M. Clowes, and J. A. Hole (1996), Inversion of three-dimensional wide-angle seismic data from the southwestern Canadian Cordillera. J. Geophys. Res., 101, 8503-8529.

Figure 2.1

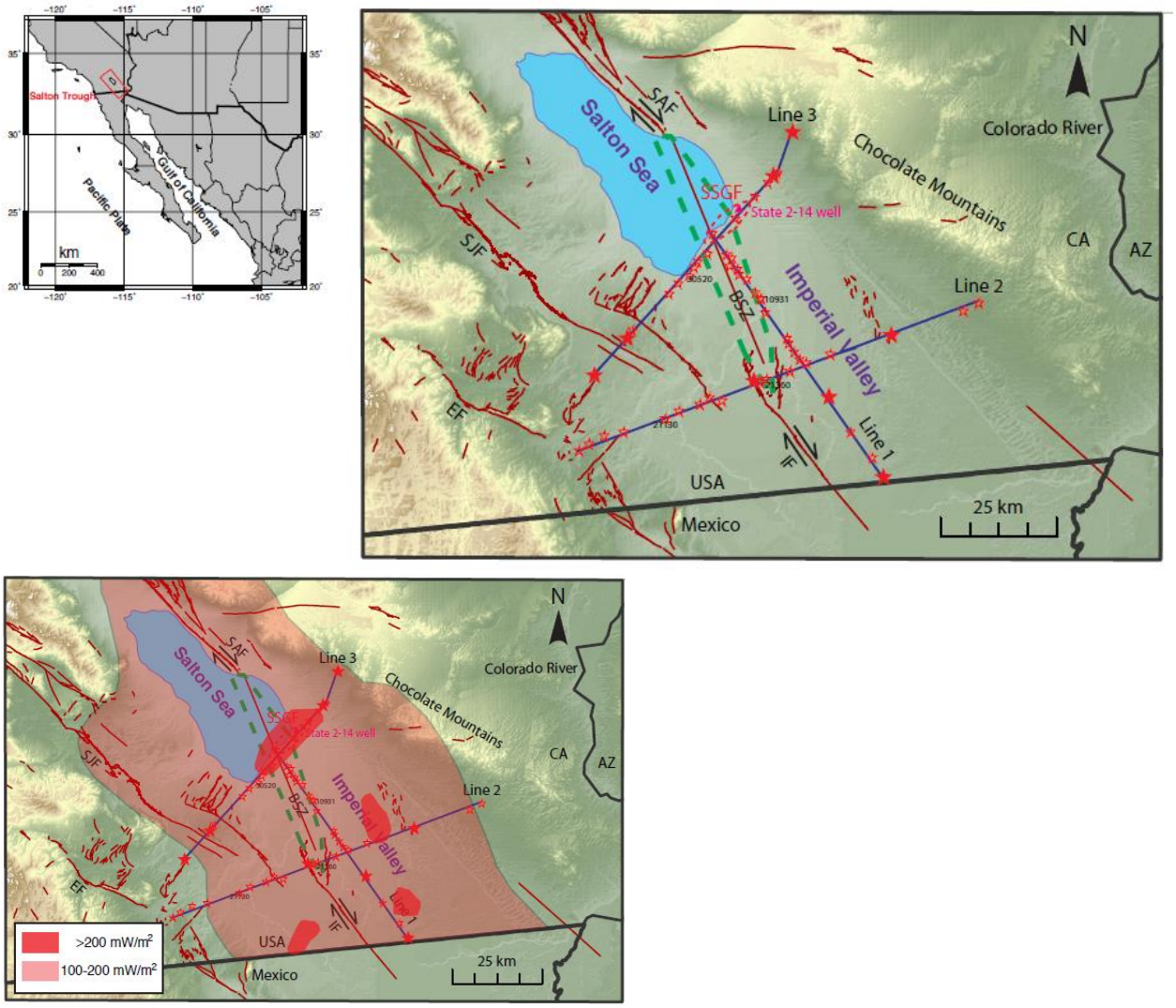

Salton Seismic Imaging Project (SSIP) study area and the experiment map. Red stars are shots along three seismic lines in blue, and larger solid stars are shots greater than 400 kg. Labeled shots are shown in the following figures. Red lines are Quaternary faults by USGS. Heat flow is shown by shaded area at the bottom panel (after *Lachenbruch et al*., 1985). Note, CA, California; AZ, Arizona; SAF, San Andreas Fault; IF, Imperial Fault; SJF, San Jacinto Fault zone; EF, Elsinore Fault zone; BSZ, Brawley Seismic Zone; SSGF, Salton Sea geothermal field.

Figure 2.2

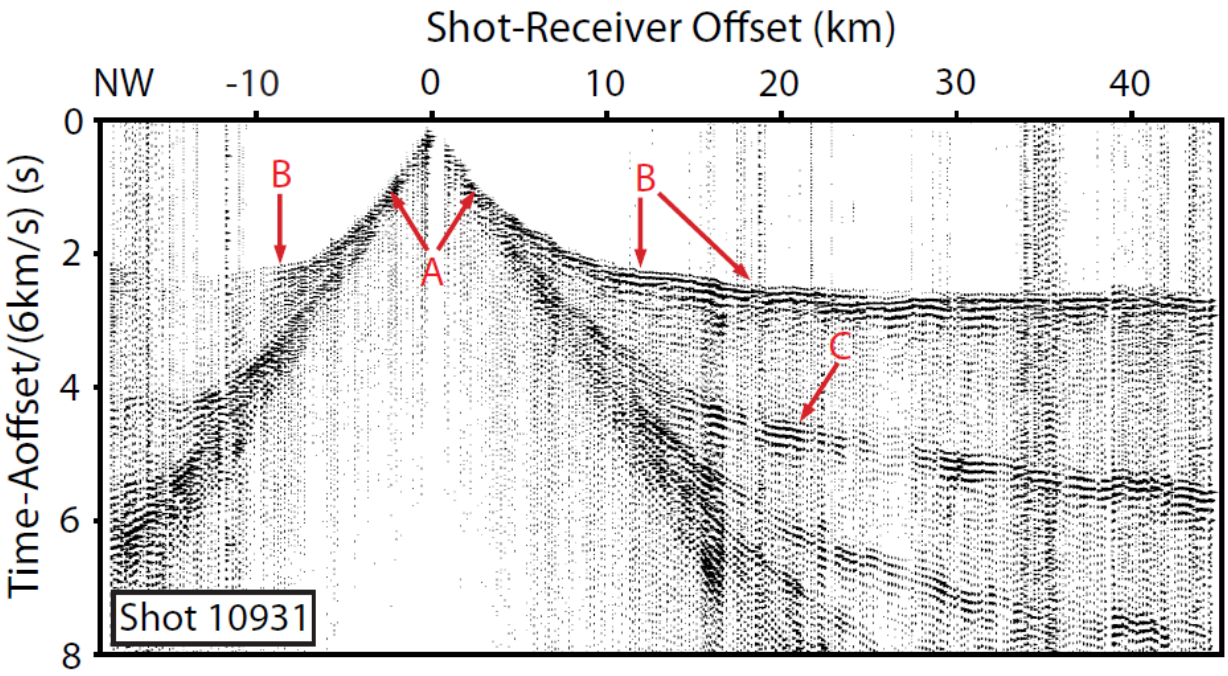

Data plot of shot 10931 from Line 1. Only the portion of the line in the Imperial Valley is shown (Figure 2.1). The data are bandpass filtered using a minimum phase Ormsby 5-8-20-30 Hz filter in Halliburton SeisSpace industry software. Amplitudes are normalized for each station. Smaller signal at the northwest end of the figure is due to normalization of geothermal energy industrial noise. Label A is waves that have traveled in the sediment; B is energy that has turned in deeper sediment or crystalline rock; phases C are basin reverberations.

Figure 2.3

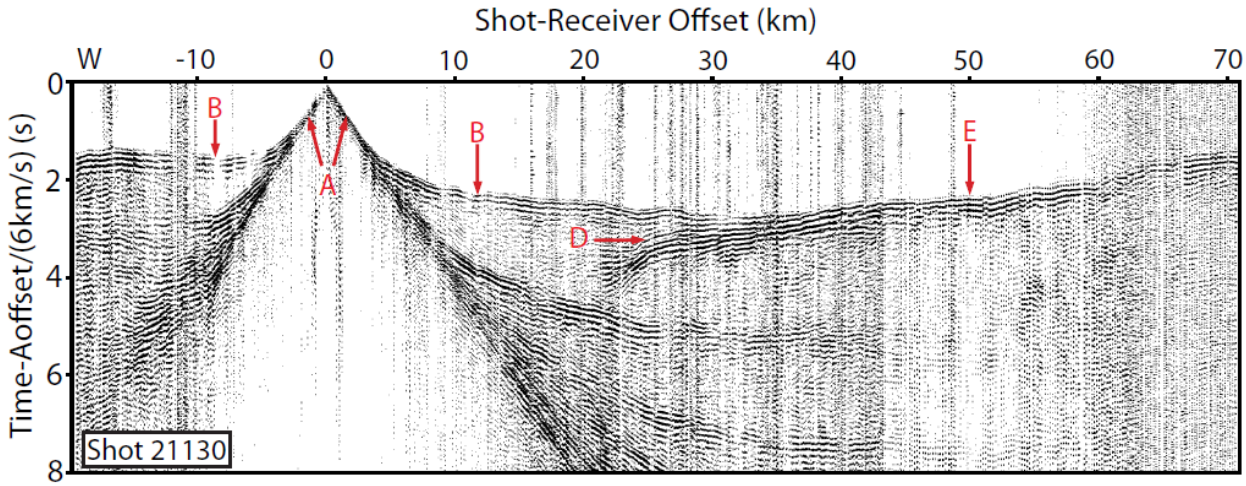

Data plot of shot 21130 from Line 2. It is plotted and labeled similar to Figure 2.2. West is to the left. This line segment crosses the Imperial Fault (IF) and extends beyond farmland (lacustrine clay soil) onto the alluvial flanks of the Imperial Valley (Figure 2.1). Phase D, reflection from the middle crust; E, refraction from beneath reflector D.

Figure 2.4

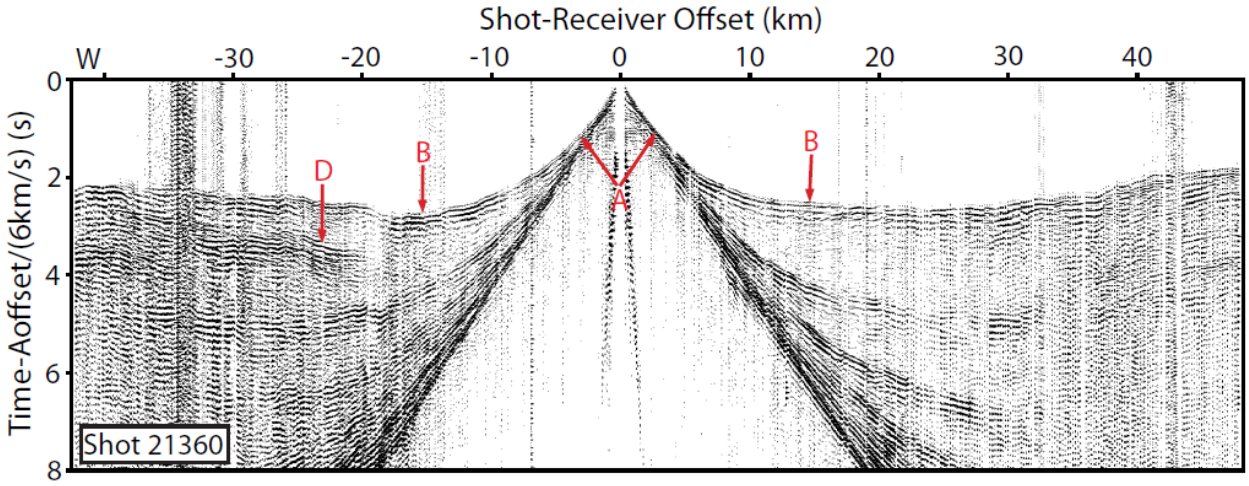

Data plot of shot 21360 from Line 2. It is plotted and labeled the same as Figure 2.3. The shot is close to the Imperial Fault (IF).

Figure 2.5

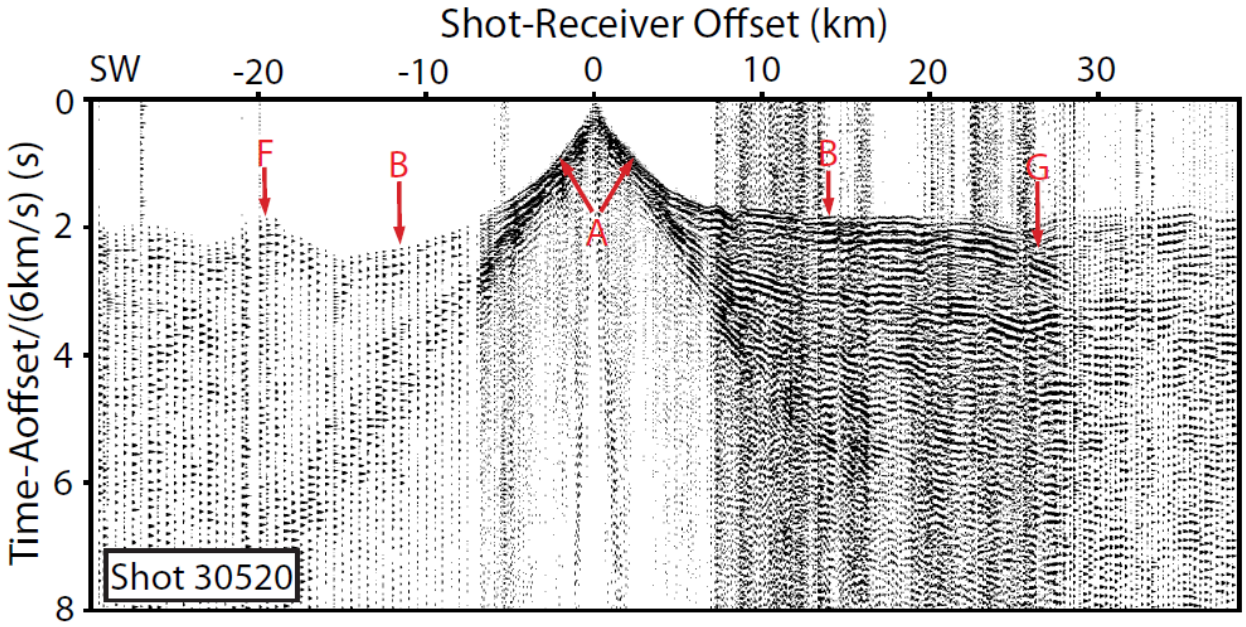

Data plot of shot 30520 from Line 3. It is plotted and labeled the same as Figure 2.2. This line extends along the Salton Sea geothermal field (SSGF) near the volcanic domes, and extends beyond farmland (lacustrine clay soil) onto the alluvial flanks of the Imperial Valley (Figure 2.1). Phase F, earlier arrivals in the Superstition Mountains; phase G, diffraction at the edge of the shallow crystalline rock. Phase B to the east of the shot is ~0.5 s earlier within the SSGF.

Figure 2.6

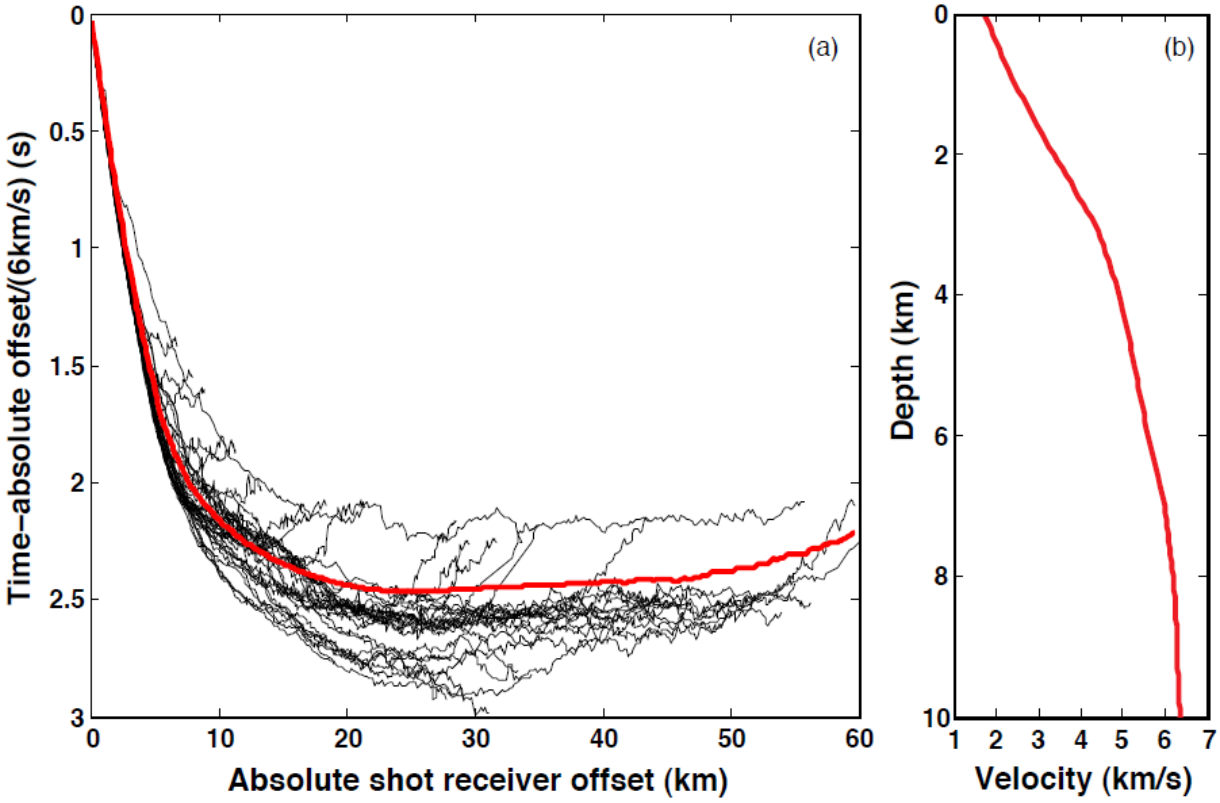

1D starting velocity model of Line 1. a) Reduced first-arrival travel times for shots recorded along Line 1 (black lines) and synthetic times from the model in (b). The earlier times correspond to the shot and stations in the Salton Sea geothermal field. Later times correspond to shots and receivers in southern Imperial Valley. b) 1-D starting velocity model for Line 1 derived from the first arrival travel times.

Figure 2.7

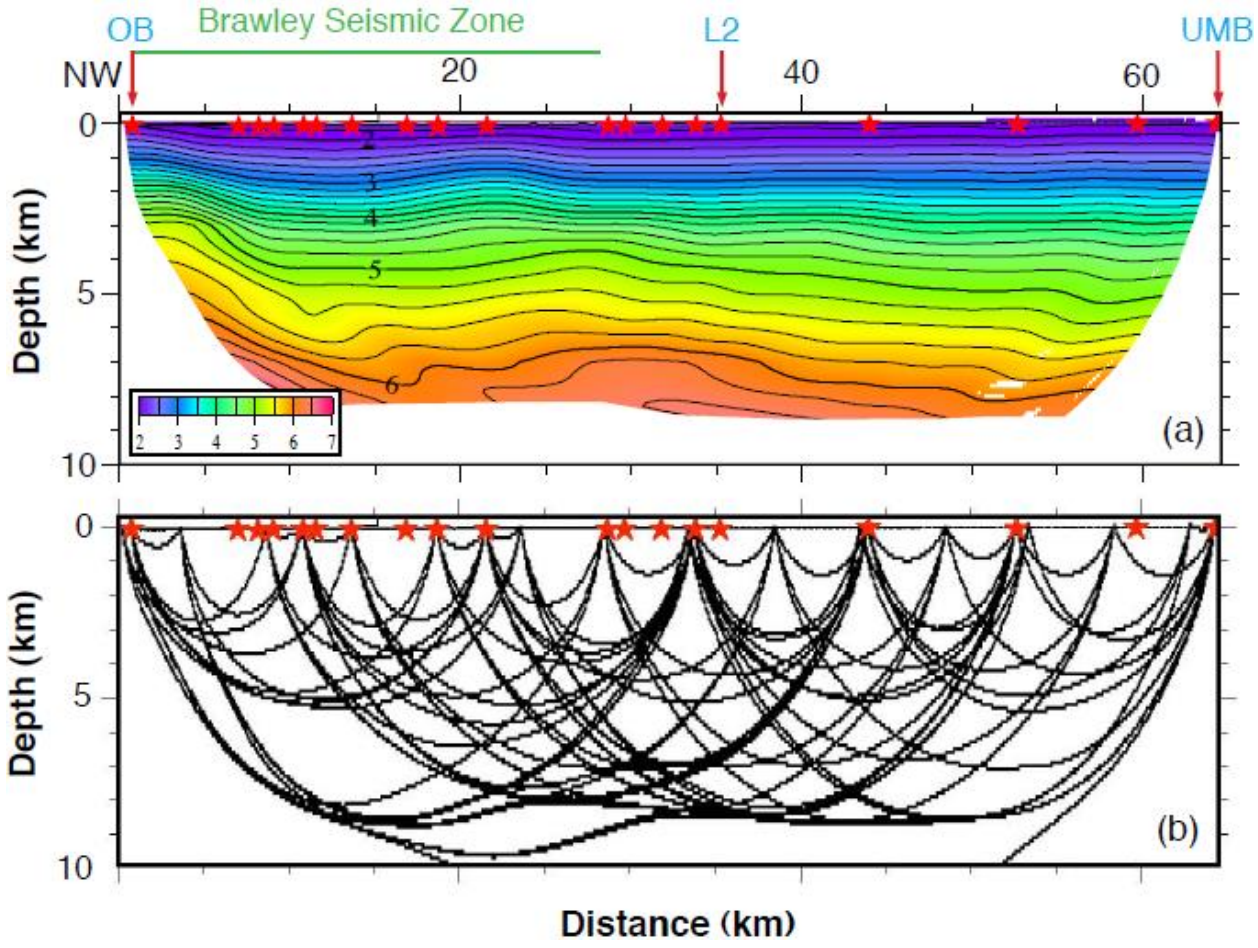

Line 1 upper crust velocity model and simplified first arrival ray paths. Red stars are shots along the seismic line. Velocity is in km/s, and contours are at 0.2 km/s intervals. The portion without direct data coverage is whitted out. In panel b, ray paths are plotted for shots every ~10 km and receivers every ~5 km. Note, OB, Obsidian Buttes; L2, Line 2; UMB, USA-Mexico border.

Figure 2.8

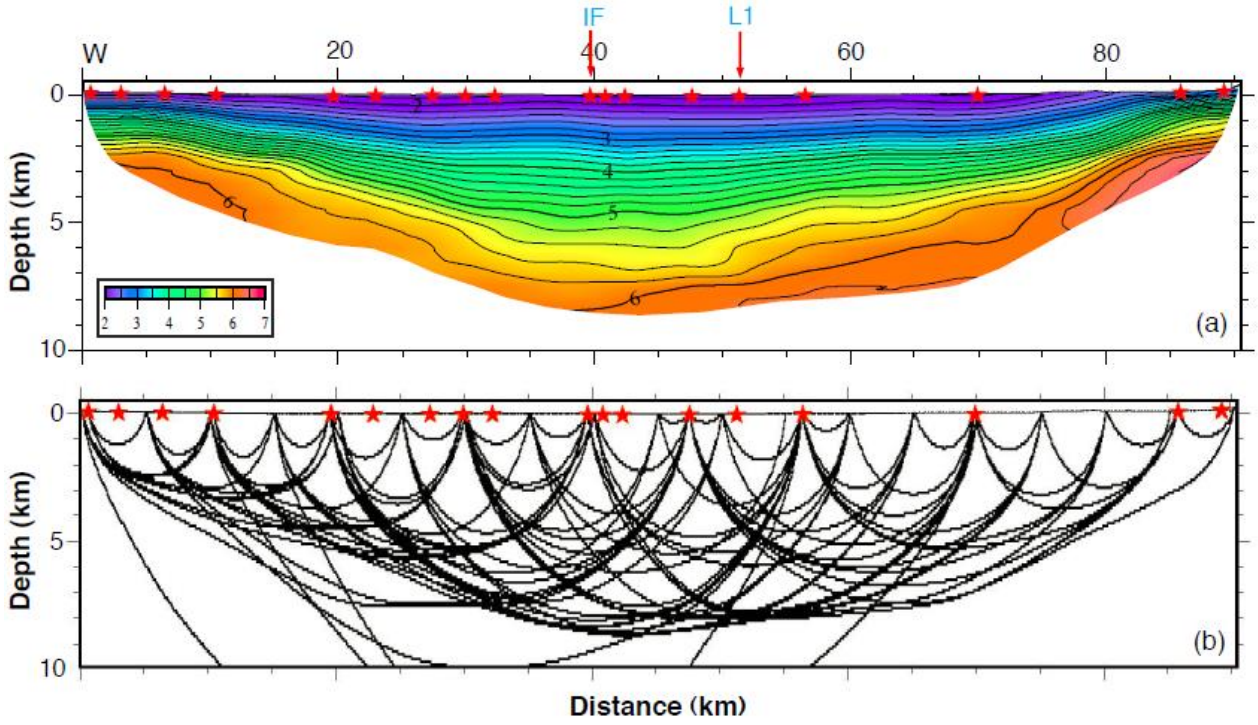

Line 2 upper crust velocity model and simplified first arrival ray paths. It is plotted as Figure 2.7.

Note, IF, Imperial Fault; L1, Line 1.

Figure 2.9

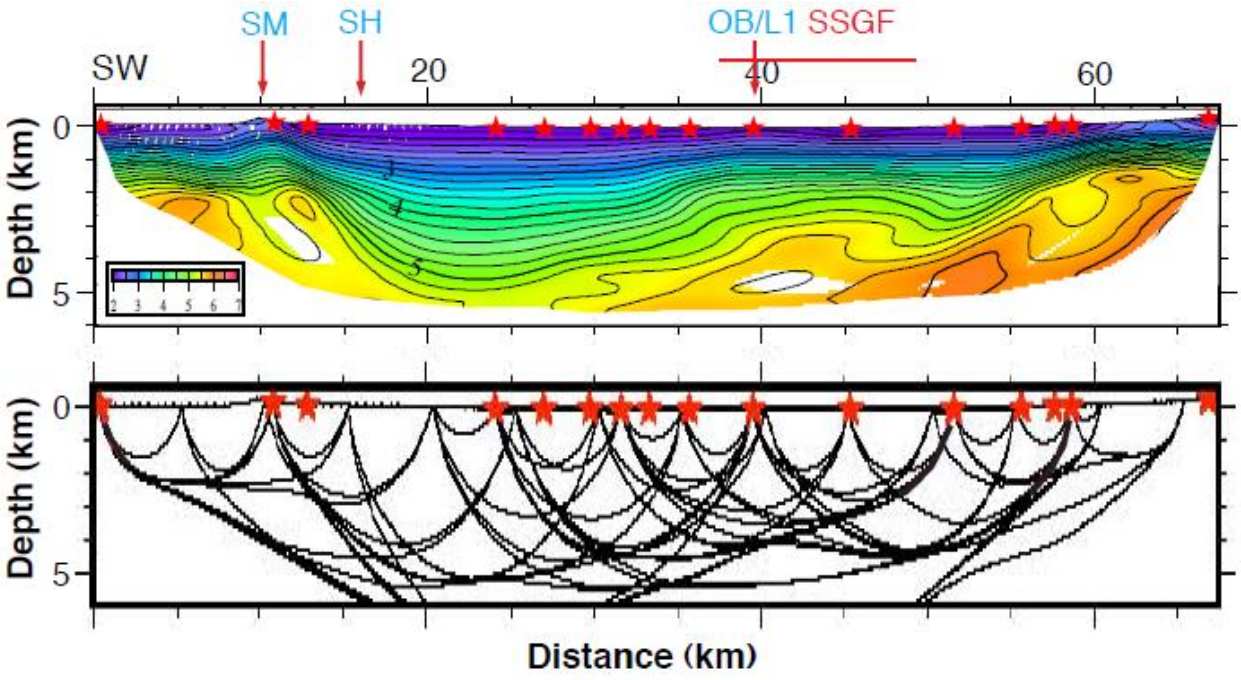

Line 3 upper crust velocity model and simplified first arrival ray paths. It is plotted as Figure 2.7. Note, SM, San Jacinto Fault zone Superstition Mountain section; SH, San Jacinto Fault zone Superstition Hills section; OB, Obsidian Buttes; L1, Line 1; SSGF, Salton Sea geothermal field.

Figure 2.10

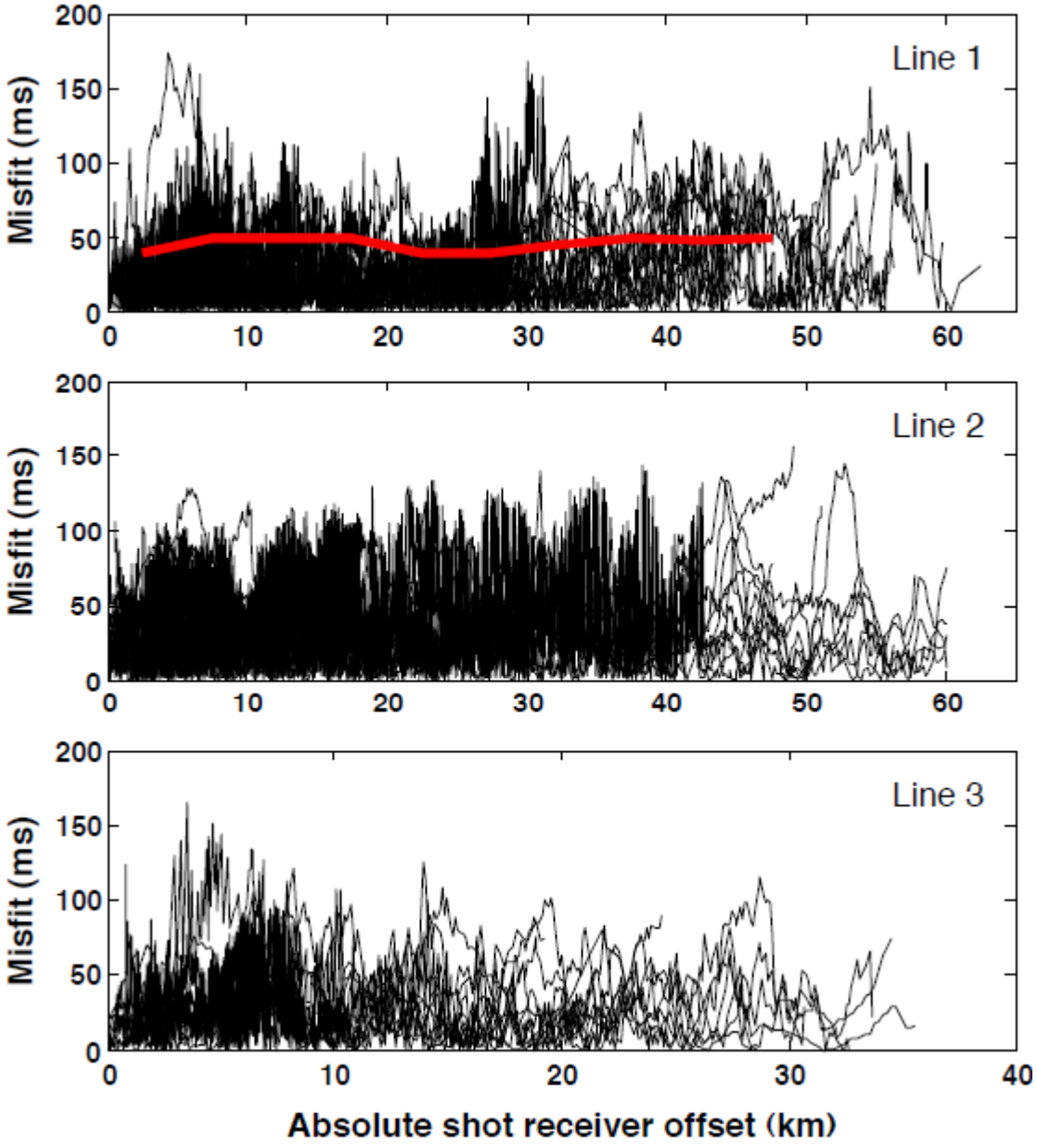

RMS misfit of all three seismic velocity models. The x-axis is absolute shot receiver offset. The red solid line in the top panel is the half cycle of the main first arrival phase of shot 10931 at different offset.

Figure 2.11

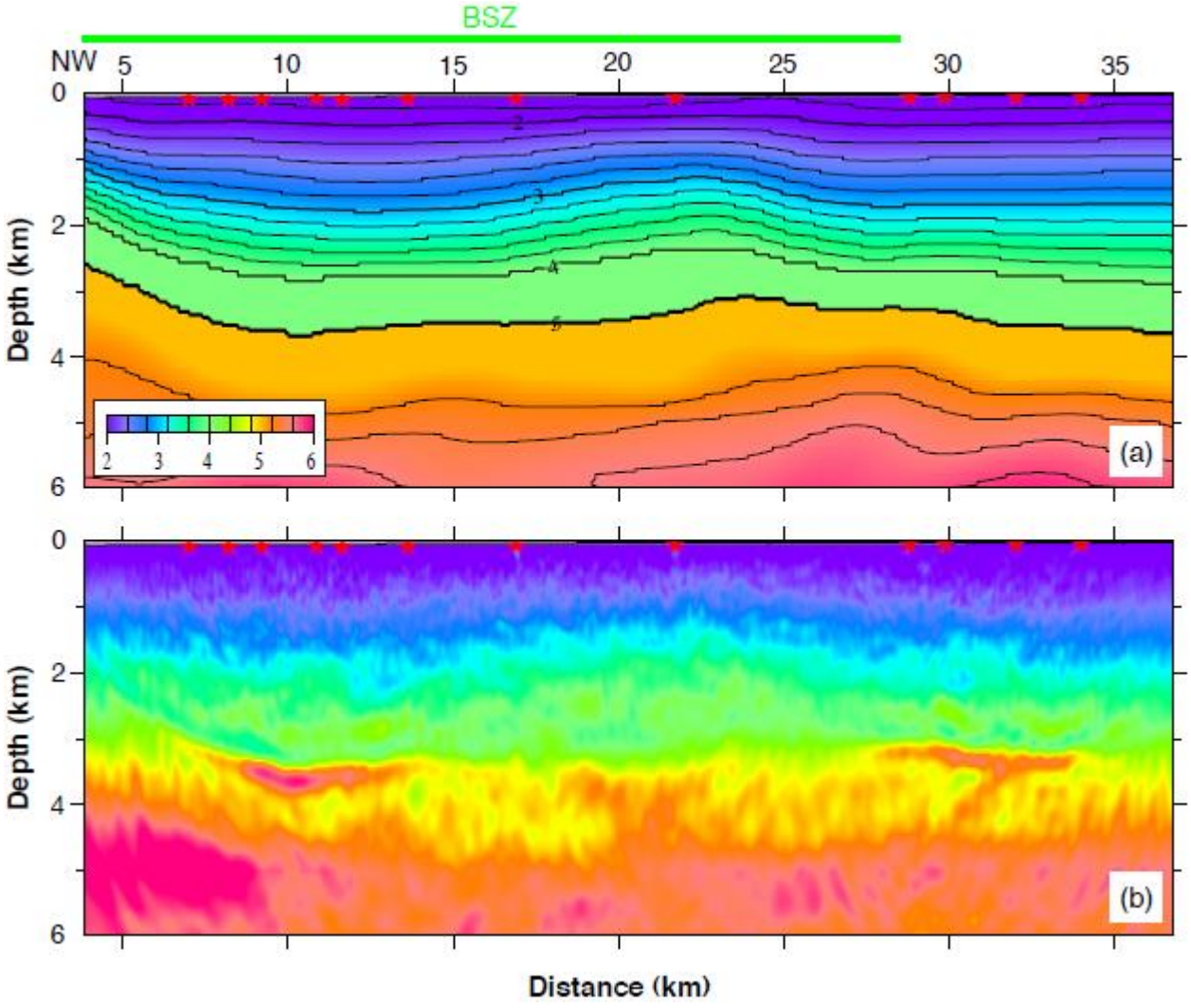

The base model and the velocity model after full waveform inversion in the synthetic experiment. a) The synthetic base model is derived from the model of Figure 2.7 with an added 4 km/s to 5 km/s discontinuity. The distance axis is labeled as for Figure 2.7. b) Results of full-waveform inversion of 2-7 Hz synthetic seismic data for the shots shown as stars.

Figure 2.12

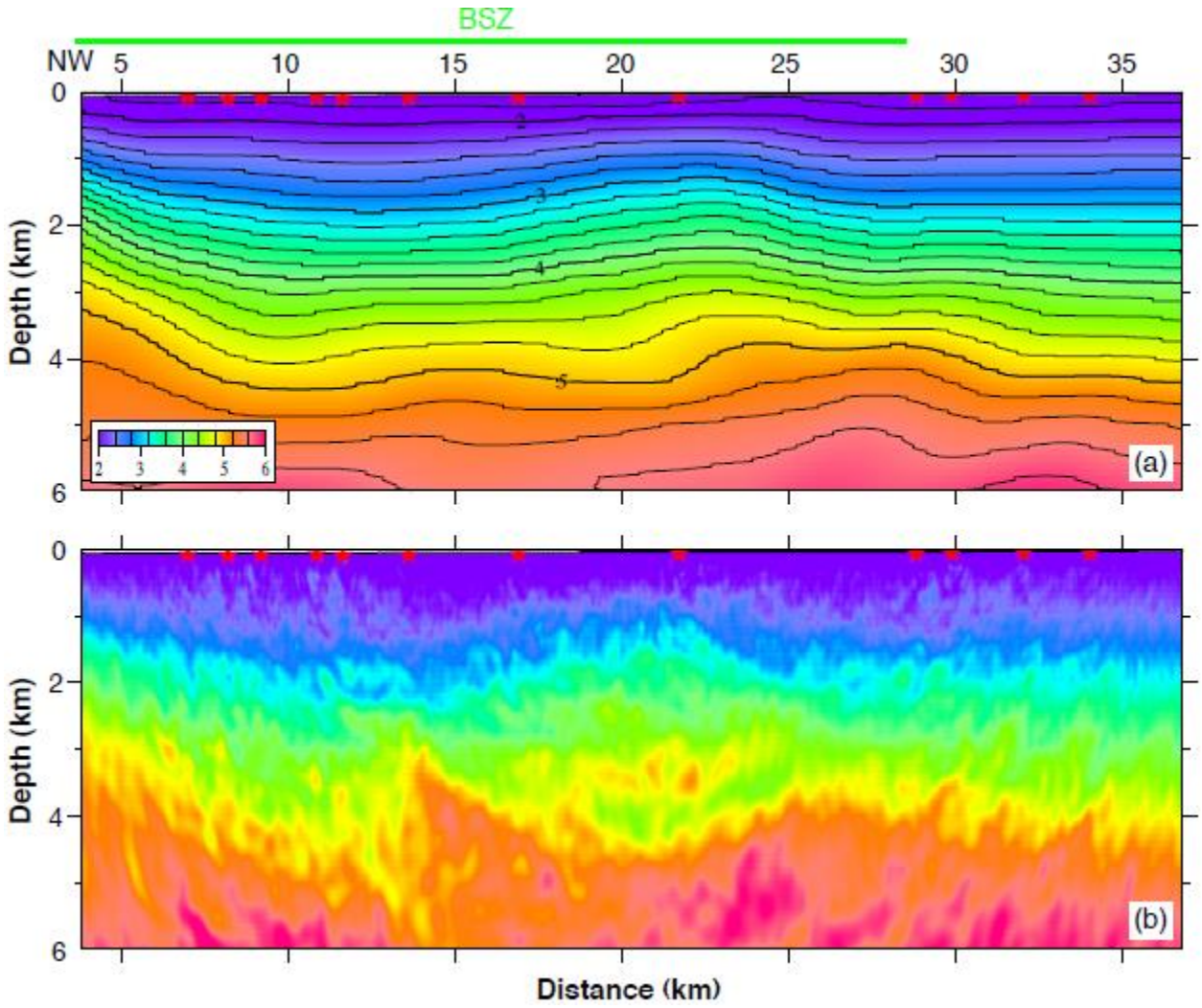

The starting model and the full waveform inversion image of Line 1. a) The starting velocity model is from first arrival travel time tomography. b) Full-waveform inversion image of a portion of Line 1, using 2-7 Hz data. The distance axis is labeled as for Figure 2.7.

Figure 2.13

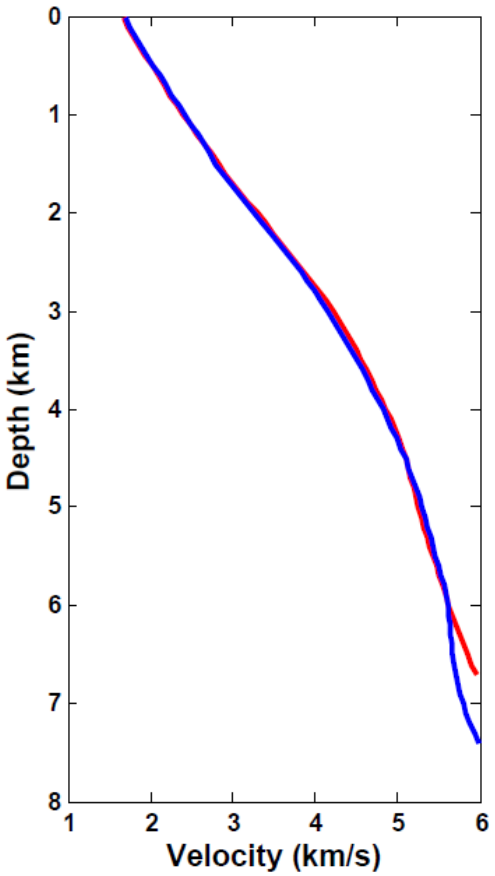

The velocity depth profiles at the intersection of Line 1 and Line 2 from both lines. Seismic velocity from Line 1 is in red, and that from Line 2 is in blue.

Figure 2.14

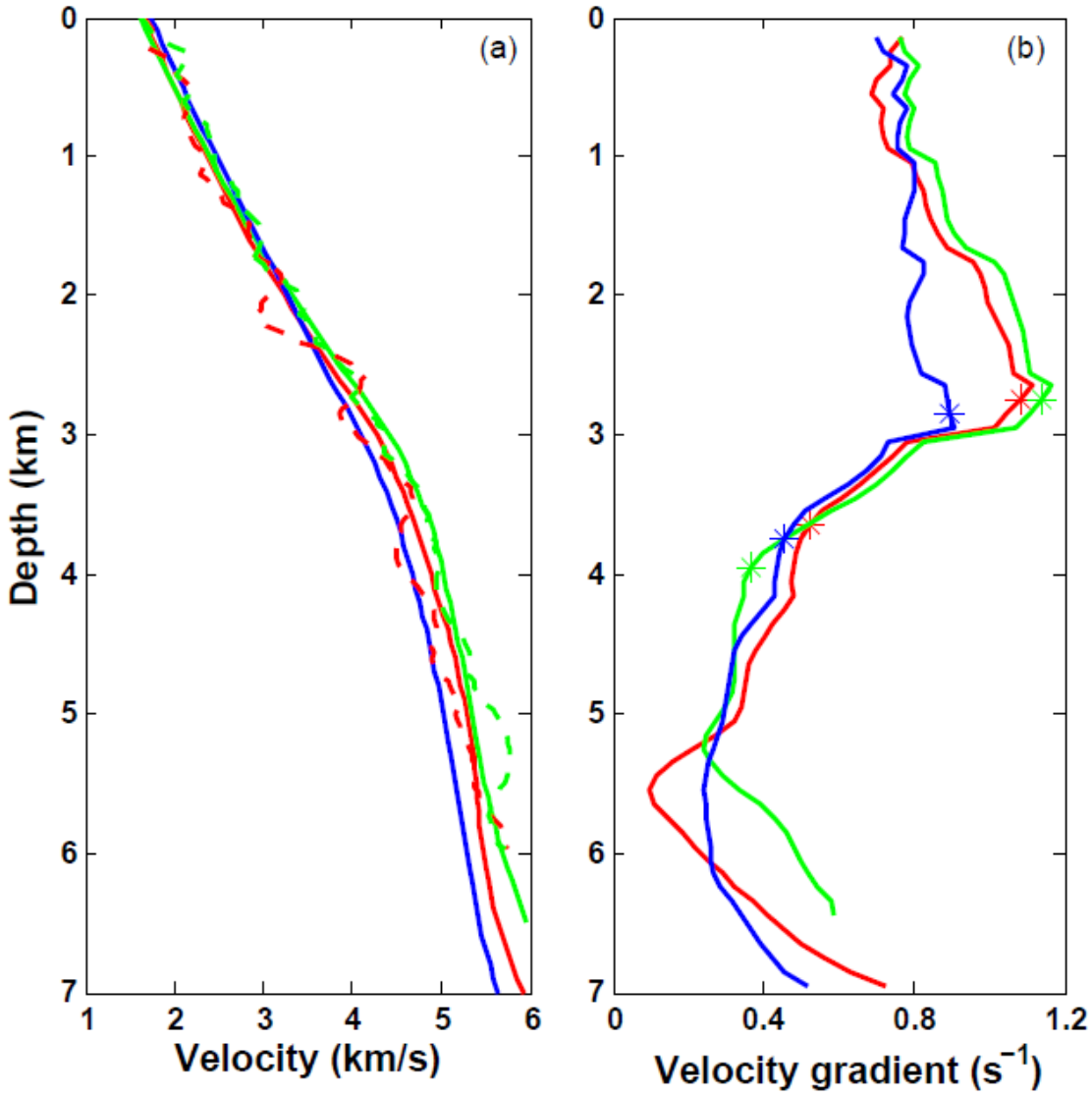

The velocity-depth and velocity gradient-depth profiles at three locations along Line 1. a) Velocity profiles at three locations along Line 1 at model km 12 (red), km 30 (green), and km 50 (blue). The solid lines are from first-arrival travel-time tomography, and the dashed lines from full-waveform inversion. The velocity-depth profiles are averaged 500 m horizontally for travel-time tomography, and 200 m for full waveform inversion. b) Velocity gradient profiles at those three locations. The top and the bottom of the transition zone is marked by stars.

Figure 2.15

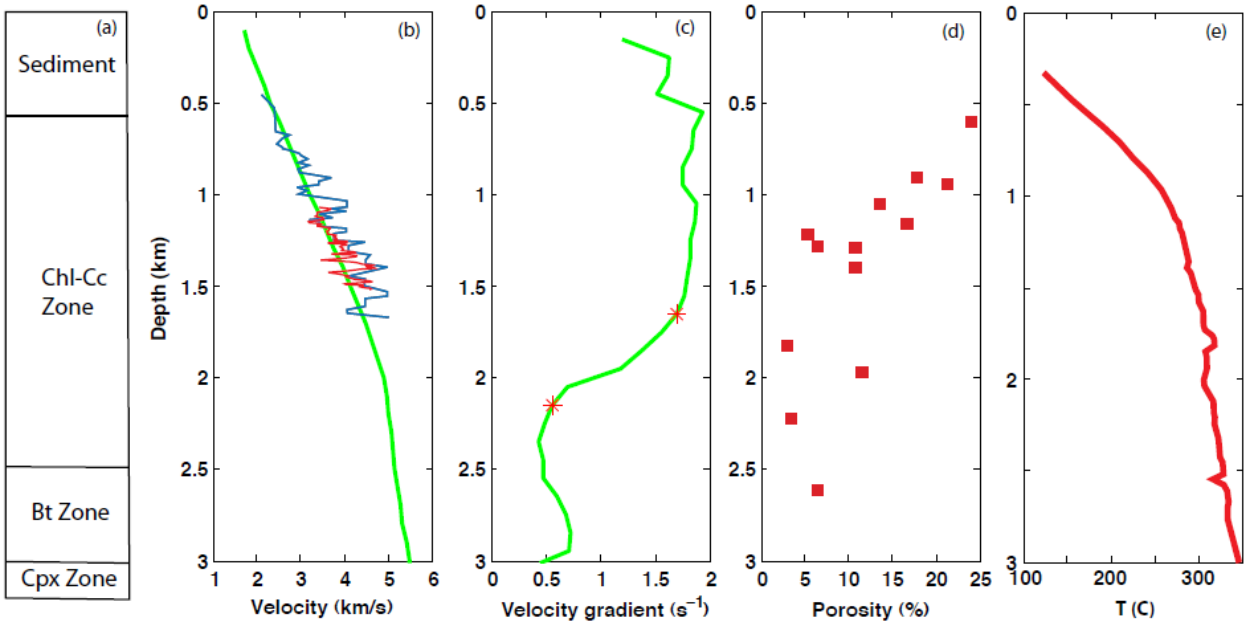

The correlation of the seismic velocity model with borehole observations from the State 2-14 well in the Salton Sea geothermal field. a) Metamorphic zones from *Cho et al.* [1988]. b) P-wave seismic velocity from this study (green), vertical seismic profiling in the well (blue) from *Daley et al.* [1988], sonic waveform log (red) from *Paillet and Morin* [1988]. c) Velocity gradient from this study. Top and bottom of the transition zone in velocity gradient are marked by red stars. d) Porosity of core samples from *Paillet and Marin* [1988]. e) Borehole temperature from *Sass et al.* [1988].

Figure 2.16

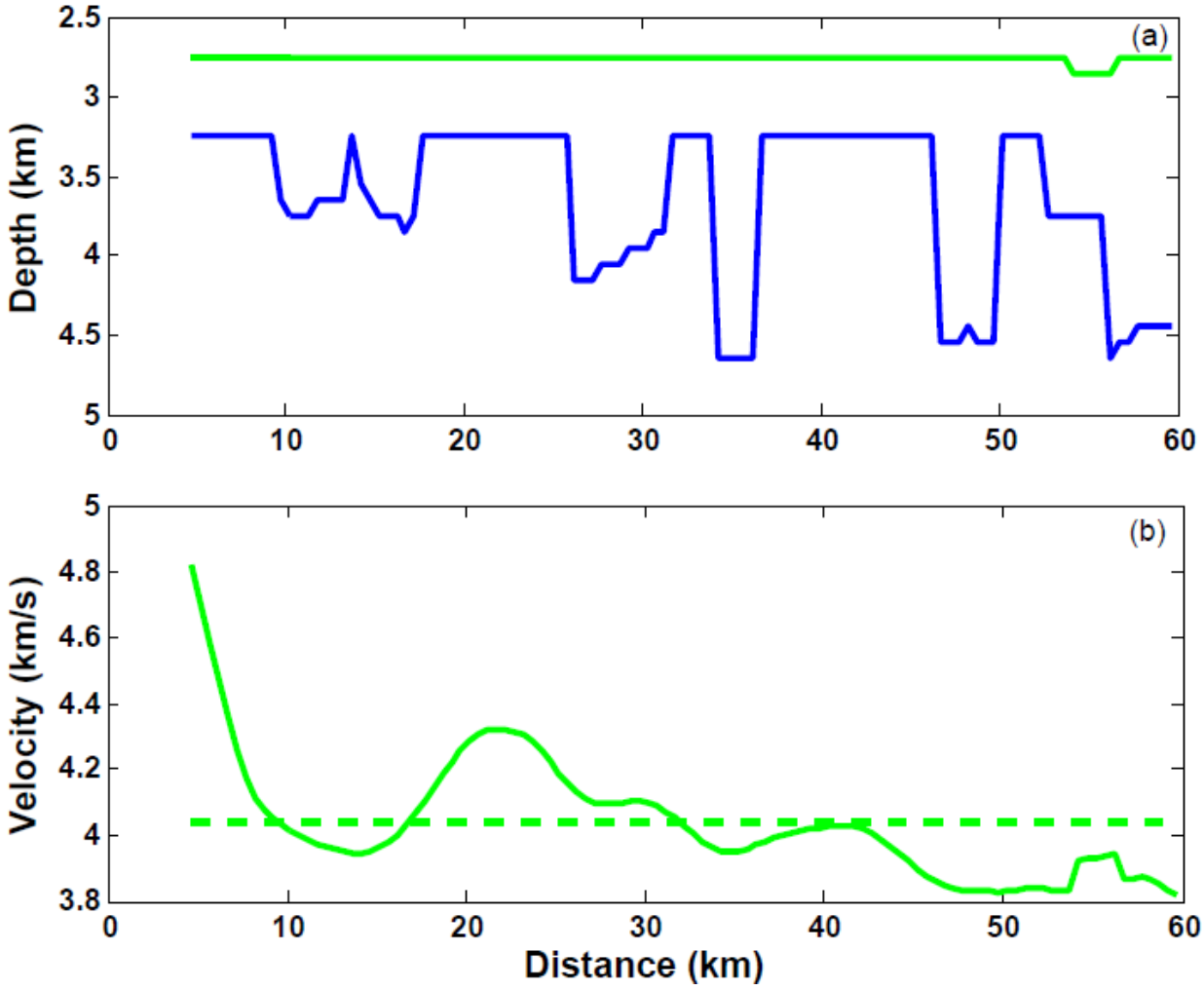

The top and bottom of the transition zone along Line 1 and the corresponding velocity. The top boundary is in green, and the bottom boundary is in blue. In panel b, the velocity at the top boundary is plotted, with the mean velocity of 4.04 km/s as a dashed line.

Figure 2.17

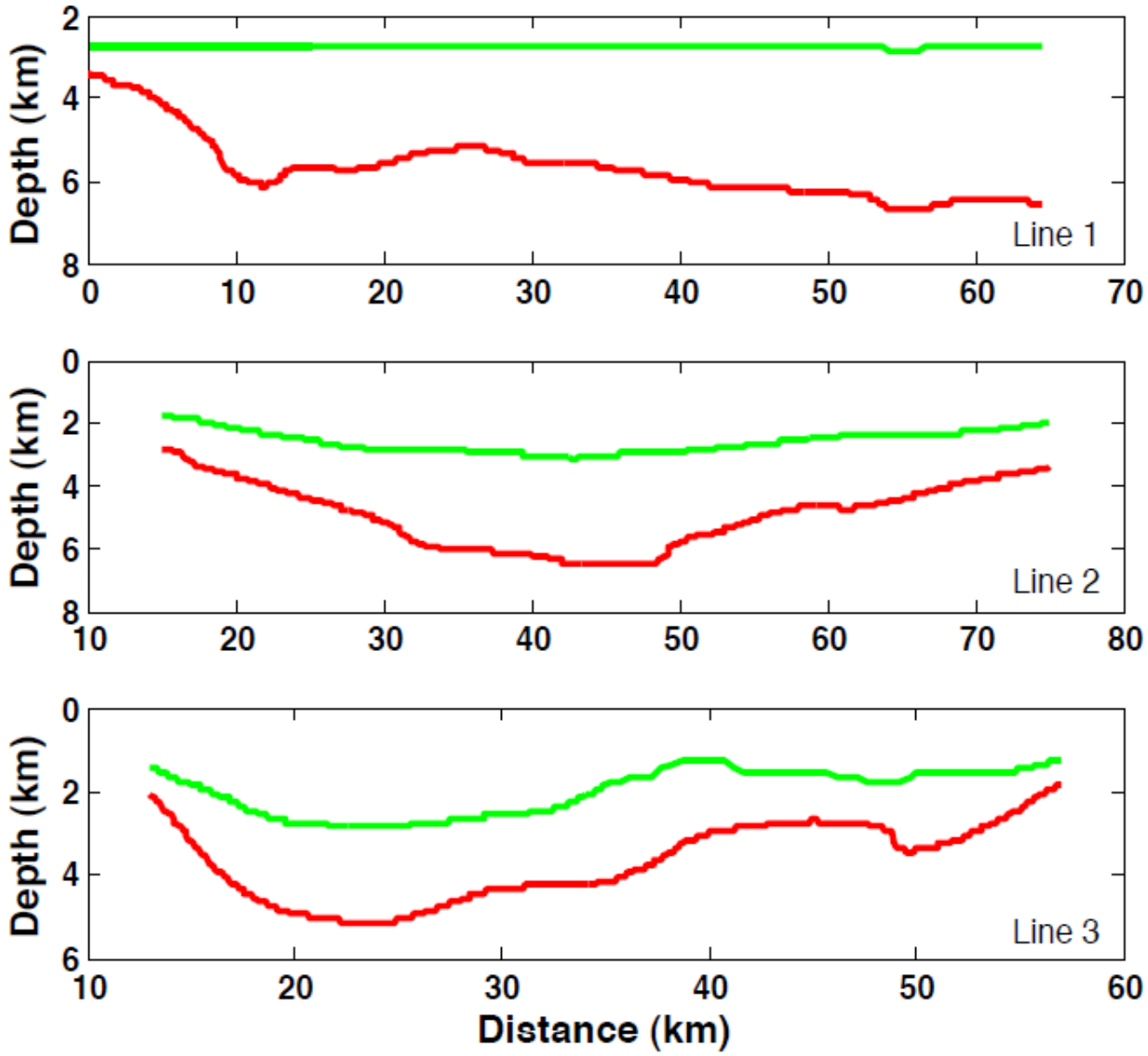

The crystalline rock depth in the valley along all three seismic profiles. The top of the change in velocity gradient within the Imperial Valley is shown in green. This depth represents a greenschist-facies meta-sedimentary rock with ~5% porosity. Red is the top of meta-sedimentary crystalline crust with very low porosity, derived using a proxy of 5.5 km/s seismic velocity (5.3 km/s for Line 3 because of shallower imaging depth). These boundaries are actually gradational due to progressive metamorphism.

Table 2.1 Inverted frequencies.

Frequencies (Hz)	Number of iterations	Synthetic-Data cost function reduction	Real-Data cost function reduction
2	8	44%	22%
2.4	8	46%	22%
2.9	8	43%	24%
3.5	8	45%	34%
4.2	8	44%	46%
5	8	44%	43%
6	8	42%	52%
7	8	44%	48%

Chapter 3

Continental rupture and the creation of new crust in the active Salton Trough rift, southern California, illuminated by the Salton Seismic Imaging Project*

Abstract

A 250-km long refraction and wide angle reflection seismic profile along the axis of the Salton Trough parallel to the direction of plate motion was analyzed to constrain the crustal and upper mantle velocity structure during active continental rifting in the Salton Trough, California. The results show that the crust is very thin and approximately one-dimensional from the northern Salton Sea to the southern end of the Imperial Valley. About 3 km of Colorado River sediment underlie the Salton Sea and Imperial Valley. The transition to underlying crystalline rock (~4.0 km/s) is characterized by a strong velocity gradient that reduces to much weaker gradient at ~2.8 km depth. This boundary is not a depositional surface, and the crystalline rock is interpreted to be sediment metamorphosed by high heat flow to at least 7-8 km deep. Deeper felsic crystalline rock with a velocity of ~6.2-6.7 km/s is less than 5 km thick, and might be stretched pre-existing crust or additional sediment metamorphosed to a higher grade. High velocity (~6.8 km/s) lower crust between ~13 km depth and the Moho is interpreted as rift-related underplated gabbros. The Moho is at 17-18 km depth and relatively flat. The upper mantle velocity is 7.8-7.9 km/s, indicative of high temperature and partial melting. Structure under the Coachella Valley is distinctly different. Sediment thins to the north and the underlying crystalline rock (~6 km/s, with a much smaller vertical gradient) is interpreted to be old granitic basement. Mafic rock does not exist at 14-18 depth as it does to the south, and a much weaker reflector suggests Moho at 28 km depth. Structure south of the International boundary in Mexico is less well constrained, but

has slower mid-crustal velocity and rocks with mantle velocity must be much deeper. The different basement and deeper Moho in the Coachella and Mexicali valleys suggest that the main rift zone lies between them, and is at least ~100 km wide. Structure is remarkably uniform in the middle and lower crust and upper mantle, despite the narrow volcanic, thermal and seismogenic rifting in the upper crust. North American lithosphere in the central Salton Trough has been rifted apart for more than 100 km, and is being replaced by new crust added by magmatism from below and sedimentation from above.

Keywords: active rifting, crustal structure, Salton Trough, tomography, controlled-source seismic, seismic velocity

* An edited version of this chapter will be submitted to *Journal of Geophysical Research*. Han, L., J. A. Hole, G. S. Fuis, J. M. Stock, N. W. Driscoll, G. M. Kent, A. Kell, M. J. Rymer, A. Gonzalez-Fernandez, and O. Lazaro-Mancilla, Crustal and upper mantle velocity structure during active continental rifting in the Salton Trough, southern California.

3.1 Introduction

Passive continental margins represent the transition from continental rifting to oceanic seafloor spreading. Passive margins are typically classified depending upon the magma volume available from decompression melting of the asthenosphere. Some continental margins are magmatically rich, characterized by transitional crust composed primarily of voluminous igneous rocks [e.g., *White and Mckenzie*, 1989; *Holbrook and Kelemen*, 1993]. Other continental margins are magmatically starved, with exposed serpentinized mantle at the seafloor [e.g., *Whitmarsh et al.*, 2001; *Hopper et al.*, 2004]. Seismic reflection and refraction imaging of the continental margin is the primary method to identify these two end members.

An intermediate type of continental margins might form new transitional crust through a combination of lithospheric stretching, magmatism and voluminous sedimentation. Numerical modeling suggests that sedimentation reduces the time to localize continental rifting into a narrow rift [*Bialas and Buck*, 2009]. They argue that the weight of sediment reduces lateral differences in buoyancy forces, promoting narrow rifting. The creation of new crust by thick sedimentation and magmatism probably also play an important role in this rifting process. The Salton Trough in southern California and northern Mexico (Figure 3.1) is an excellent site to study this type of continental rifting process and the roles of magmatism and sedimentation in the creation of the transitional crust.

The 2011 Salton Seismic Imaging Project (SSIP) was designed to investigate rifting processes at the northern end of the Gulf of California and earthquake hazards at the southern end of the San Andreas Fault system. This paper derives the whole crustal and upper mantle seismic velocity structure along the axis of the Salton Trough to understand the rifting process.

Specific goals include the role of sedimentation on rift localization, whether magmatism from the upper mantle is localized or widely distributed in the lower crust, whether pre-existing continental crust underlies the rift, and the overall width of the rift.

3.2 Tectonic Setting

The Salton Trough is the northern end of the Gulf of California extensional province (Figure 3.1) [e.g., *Elders et al.*, 1972; *Lonsdale*, 1989; *Stock and Hodges*, 1989; *Larsen and Reilinger*, 1991]. The initial opening of Gulf of California began about 12 Ma, shortly after subduction ceased along the continental margin of Mexico [*Stock and Hodges*, 1989]. Nearly all of the dextral displacement between the Pacific and North American plates prior to 6.3 Ma was accommodated outside of the gulf region, and the plate boundary motion was localized in the Gulf of California by 6 Ma [*Oskin et al.*, 2001; *Oskin and Stock*, 2003]. Total opening is estimated to be ~270 km since 6.3 Ma along the entire length of the Gulf of California rift system, including the Salton Trough [*Oskin and Stock*, 2003; *Dorsey et al.*, 2007].

The Gulf of California is characterized as a series of right-lateral transform faults and relatively short rift segments that result from the plate motion between Pacific Plate and North American Plate (Figure 3.1). In the southern Gulf, the pull-apart rifts have evolved into full seafloor spreading [*Larson et al.*, 1968]. In the central Gulf, hundreds of km of oceanic crust are covered by ~4-km thick sediments [*Lizarralde et al.*, 2007]. The northern Gulf is underlain by thick sediment from the Colorado River and the continental crust has been extensively stretched and only recently broken [*Gonzalez-Fernandez et al.*, 2005; *Martin-Barajas et al*., 2013].

The Salton Trough is an on-shore analog to those rift systems in the Gulf of California, lying at the mouth of the Colorado River. It was formed by oblique extension between the right

lateral strike-slip San Andreas Fault (SAF) and Imperial Fault near the Salton Sea, and between the Imperial Fault and the Cerro Prieto Fault in northern Mexico (Figure 3.1). The Salton Trough includes the Coachella Valley, Salton Sea, Imperial Valley and Mexicali Valley along the axis from northwest to southeast. The southern segment of SAF runs along the northeast side of the Salton Trough, and terminates at the eastern shore of the Salton Sea. The current slip rate of SAF in the Coachella Valley is ~2.6 cm/yr, which accounts for most of the ~3.5 cm/yr motion along the Imperial Fault, and the remaining plate motion (~0.9 cm/yr) is taken up by the San Jacinto Fault [*Bennett et al*., 1996]. The Salton Sea is ~70 m below sea level, separated from the Gulf by the Colorado River delta that is ~12 m above sea level near the USA-Mexico border. The Salton Sea is less than 50 m deep, formed by a drainage canal accident in 1905 that diverted water from the Colorado River, and evaporation is balanced by irrigation runoff.

The northern Imperial Valley and southern Salton Sea are seismically highly active. Most of the seismicity occurs at ~4-10 km depth in the Brawley Seismic Zone (Figure 3.1) [*Lin et al.*, 2007; *Hauksson et al.*, 2013]. The entire valley is also characterized by very high heat flow, ~140 mW/m^2 on average [*Lachenbruch et al*., 1985], more than double the average continental heat flow. Volumetrically minor and young volcanism (<500 ka) is observed at the Salton Buttes along the southern shore of the Salton Sea [*Robinson et al.*, 1976; *Schmitt and Vazquez*, 2006; *Schmitt and Hulen*, 2008]. A huge volume of sediment has been carried into the Salton Trough and the northern Gulf of California by the Colorado River from erosion of the Colorado Plateau [*Dorsey*, 2010; *Dorsey and Lazear*, 2013]. The sedimentation rate in the area of the Salton Buttes over the last ~0.8 Ma is estimated to be in the range of 2.2-3.8 mm/yr [*Schmitt and Hulen*, 2008].

3.3 Previous Seismic Work

Numerous studies have used regional seismic networks and local earthquakes to develop three dimensional (3D) velocity models in southern California [e.g., *Magistrale et al*., 1992; *Zhao et al.*, 1996; *Magistrale et al*., 2000; *Hauksson*, 2000; *Kohler et al.*, 2003; *Hauksson*, 2010; *Lovely et al*., 2006; *Lin et al*., 2007; *Tape et al.*, 2009; *Lin et al*., 2010; *Savage and Wang*, 2012; *Lin et al.*, 2013; *Lee et al.*, 2014]. *Richards-Dinger and Shearer* [1997] estimated an average crustal thickness of 28 km in southern California and a Moho depth of 18 km in the Salton Trough by stacking the Moho-reflected phase. *Lekic et al.* [2011], using scattering of teleseismic shear waves, suggested that in the Salton Trough, either the mantle lithosphere has experienced more thinning than the crust or large volumes of new lithosphere have been created. These studies were consistent with the deep sedimentary basin, high velocity floor, and shallow Moho in the Salton Trough. Some of those models were aided by including information from seismic refraction studies, which provided a much better resolution on the crustal and upper mantle structures due to dense station coverage.

In the Salton Trough, two previous controlled-source seismic refraction surveys were acquired to study the basin structure. *Fuis et al.* [1984] and *Kohler et al*. [1986] imaged the upper and middle crust throughout the entire Imperial Valley, but neither the Moho reflected phase PmP nor refracted phase Pn were recognized to constrain deep crustal structure. The survey of *Parsons and McCarthy* [1996] imaged the Moho at ~21-22 km depth in the Imperial Valley and deepening to ~27 km beneath the Chocholate Mountains east of the valley. However, no Pn phase was recorded, and the profile along the axis of the Salton Trough is poorly resolved. *Larkin et al.* [1996] performed low-resolution deep crustal seismic reflection imaging of the transitional crustal structure between the Salton Trough and the Basin and Range province.

Brothers et al. [2009, 2011] studied basin and fault architecture in the top ~70 m in the Salton Sea using high resolution chirp seismic reflection data.

In Mexico, multichannel seismic reflection and refraction/wide-angle reflection seismic profiles have been analyzed to image basin structure and rifting styles in the inactive Altar Basin of the southern-most Salton Trough [*Pacheco et al*., 2006], in the northern Gulf of California [*Persaud et al.*, 2003; *Gonzalez-Fernandez et al*., 2005; *Aragon-Arreola and Martin-Barajas*, 2007; *Gonzalez-Escobar et al.*, 2009; *Martin-Barajas et al*., 2013], and in the central and southern Gulf of California [*Aragon-Arreola et al*., 2005; *Lizarralde et al.*, 2007].

3.4 SSIP Data

3.4.1 Data Acquisition

Seven onshore seismic refraction and wide-angle reflection 2-D profiles and two 3-D grids, all recording both inline and offline shots, were acquired by SSIP in 2011 to image the 3-D structure of the Salton Trough (Figure 3.1). Ocean-Bottom Seismometers (OBS) were deployed in the Salton Sea to record both onshore shots and air-gun shots in the Sea, in order to fill the data coverage gap between the Coachella and Imperial Valleys.

Two types of seismographs were used on land, RefTek 125a "Texans" with single-component 4.5-Hz geophones, and RefTek 130's with 3-component 4.5-Hz geophones. The sample rate was 4 ms. The OBS's were L-CHEAPO 4x4 with 4 component 4.5-Hz seismographs plus hydrophone but a sample rate of 5 ms. In total, 2762 land seismographs and 50 OBS's were used at 4206 sites, in spacing as dense as 100 m. Onshore controlled sources were 126 explosions of 3-1400 kg contained in plugged boreholes, and in the Salton Sea a 3.44 L

generator-injector (GI) airgun was fired at 2330 locations. Complete details about the survey are described in *Rose et al.* [2013].

This paper is focused on the 250-km long NNW-SSE refraction and wide-angle reflection profile along the axis of the Salton Trough, parallel to the transform faults and relative plate motion direction (Figure 3.1). The explosive shot information is listed in Table 3.1. Densely spaced (~3 km) but small (~120 kg) shots were fired to provide dense ray coverage of the upper crust in the Brawley Seismic Zone (BSZ), while large shots up to 1440 kg were used to produce deep crustal and upper mantle phases (PmP and Pn). The land seismographs on this profile were all single component Texans at a spacing of 100 m for the smaller shots and 100 or 200 m for large shots. The receiver spacing in Mexico was 500 m. 38 OBS's were deployed along the line at ~1500 m spacing. 366 airgun shots were fired every ~100 m along the line to constrain the upper crustal structure of the Salton Sea. Three gaps in station coverage exist at the US/Mexico border, the southern shore and the northern shore of the Salton Sea.

3.4.2 Data Description

Three types of seismic data were recorded: shot-Texan data, shot-OBS data, and OBS-airgun data. Air-gun shots were also recorded by land seismometers very close to the Salton Sea, but they were not included here due to the short recording offset range and the low data quality. The seismic line went through different environments, including urban areas with vehicle traffic, a shallow water lake, energy plants in a geothermal field, and active farms. The response of onshore seismometers was different from that of the OBS. Explosive shot size varied, and coupling varied primarily as a result of dry or wet holes. The station spacing was much larger in

Mexico and in the Salton Sea. As a result of all these factors, there were systematic variations in noise level along the line.

Representative data sections are shown in Figures 3.2-3.6. Data quality is generally best in the farmland of the Imperial and Mexicali Valleys, with the exception of the geothermal field near the Salton Sea. Seafloor OBS data were of good quality, but larger station spacing reduced the ability to correlate low-amplitude phases. Urban noise was high in most of the Coachella Valley, and smaller shots were required due to setbacks from structures, such that Coachella Valley data have poorer quality. The airgun was too small to be recorded beyond ~30 km offset, but provided excellent control of shallow structure under the Salton Sea [*Kell et al*., submitted], enabling the shot-OBS data to constrain deeper structure.

At very short shot-receiver offsets high-amplitude first arrivals "A" with an apparent velocity of ~2 km/s are direct or shallowly refracted waves in the valley sediment (Figures 3.2-3.6). These waves continue as very strong secondary arrivals, in part because a strong velocity gradient with depth produces a low-velocity surface waveguide. For all shots that produce shot-receiver raypaths that underlie the Salton Sea, Imperial Valley, and Mexicali Valley, the data are very similar (Figures 3.2-3.4 and positive offsets on Figure 3.5). Shot and OBS gathers in this region are roughly symmetric at positive and negative offsets, and observe similar arrivals at similar offsets, indicating an approximately 1-D crustal structure. There are minor variations along the valley, with the strongest being earlier arrivals for shots and stations very close to the Salton Buttes, suggesting thinner sediment at this location. Shots with raypaths that underlie the Coachella Valley have arrivals with different characteristics that will be described below.

A refracted arrival Pg phase “B” appears as a first arrival beyond a minimum offset of ~5 km. The transition from arrival “A” to “B” is not sharp, and there is no evidence for a reflection corresponding to this refractor. Arrival “B” has an apparent velocity of ~4 km/s at about 8 km offset, but increases to ~5.2 km/s by about 12 km offset, and ~6 km/s by about 20 km. The low velocity at near offset is typical of sedimentary rock, but quickly become greater than 5 km/s, which corresponds to fractured felsic crystalline rock. These changes in apparent velocity are smooth as a function of offset, suggesting that velocity increases smoothly with depth rather than having strong velocity discontinuities in the upper crust. Beyond about 50 km offset, arrival “B” increases to an apparent velocity greater than 6.6 km/s, corresponding to the lower crust. Note the long-delay high amplitude phase B', which is observed and modeled as basin reverberations of phase "B" by *McMechan and Mooney* [1980] and *Fuis et al.* [1984]. It is caused by the strong vertical velocity gradients in a thick sedimentary basin.

A strong secondary arrival "D" appears at offsets beyond 40 km throughout the Salton Sea, Imperial and Mexicali Valleys (Figures 3.2, 3.3 and 3.5). This arrival has the curvature and strong amplitude typical of a wide-angle reflection from a sub-horizontal boundary. It is observed for shot-receiver midpoints from the northern end of the Salton Sea to Mexico (PmP in Table 3.1). While this strong arrival is observed at > 40 km offset on many shots, only a handful of shots have sufficiently strong signal to record a refracted first arrival “E” beyond ~80 km offset. “E” has the correct offset-time geometry to be from a refractor corresponding with reflector “D” (Figures 3.3 and 3.5). Arrival “E” has an apparent velocity of ~7.8 km/s, identifying “D” and “E” as the reflection from the Moho (PmP) and refraction from the upper-most mantle (Pn), respectively. Pn is strong on the shot at the southern end of the line recorded in the northern Imperial Valley and on several shots in the southern Imperial Valley recorded on the

OBS in the Salton Sea (Table 3.1). Only on one shot can Pn be observed on stations in the southern Coachella Valley (Figure 3.3). Fortunately, shot 11620 in the southernmost Coachella Valley (Figure 3.5) produced an extremely weak Pn arrival recorded on stations in the Imperial Valley that reverses the Pn ray path. The reciprocity of shot-receiver travel times with shot 10460 (Figure 3.2) at the southern end of the Imperial Valley was necessary to identify this arrival in Figure 3.5; no other shots in the north produced Pn on stations to the south. Numerous shots reverse the PmP ray coverage beneath the southern Salton Sea and the Imperial Valley (Table 3.1). At later times than Pn, the crustal refraction "B" with an apparent velocity of ~6.8 km/s and the PmP "D" converge into a single arrival with stronger energy than Pn (Figures 3.2, 3.3 and 3.5). A multiple of this phase is also observed as phase D' on shot 11620 in Figure 3.5. The very short shot-receiver offsets at which PmP (strong beyond 40 km) and Pn (first arrival beyond 80 km) are observed indicate a very thin crust; typical continental crust observes those arrivals at almost double those offsets.

In the Coachella Valley, the refracted arrival Pg phase "C" behaves differently from "B" (Figure 3.6 and negative offsets on Figure 3.5). It has an apparent velocity of ~6 km/s at earlier time from ~10 to >60 km offset, which requires a shallow refractor and a very small velocity gradient beneath. The velocity at the refractor corresponds to relatively unfractured felsic crystalline rock. Note the sharp change in arrival time at ~10 km offset to the north. It indicates a near surface sharp basin thickness change, which may be fault-related or caused by three dimensional geology and the crooked line geometry. Beneath the Coachella Valley, refracted phase "C" does not increase to apparent velocity beyond 6.2 km/s. This is distinctly different from "B" to the south, which requires the presence of 6.7 km/s at relatively shallow depth. If such a velocity exists under the Coachella Valley, it must be at much greater depth. The apparent

velocity and curvature of Pg phase B and that of phase C is significantly different, which suggests that the basement in the Coachella Valley is different from that beneath the Salton Sea and the Imperial Valley.

In contrast to the Imperial Valley, most shots don't have long offset recording and the data quality is too low to constrain the deep crustal structures in the Coachella Valley. Two exceptions are shot 11620 (Figure 3.5) and shot 12220 (Figure 3.6). A very weak arrival "F" is observed on shot 11620, and a possible reflection phase G with ~10 km offset range is recorded on shot 12220. PmP phase “D” in the Imperial Valley is not observed on shot 11620. Phase F is tentatively identified as a reflection off the Moho (PmP2), although no data exist at sufficient offset to identify whether this phase correlates with an upper-mantle refraction or not. The depth corresponding to this reflector is very similar to the regional Moho in southern California. If phase G is a deep crustal reflection, the arrival time suggests a depth similar to that of the Moho beneath the Salton Sea, but the short recording range limits any further modeling. Because a clearer deep crustal reflection (phase F) is identified at the same middle point range on shot 11620, phase G is not interpreted as a Moho reflection. We admit that better data is required in order to construct the lower crustal and upper mantle structures in the Coachella Valley, but the observation from SSIP dataset suggests that the middle crust and the Moho in the Coachella Valley is distinct from that beneath the Salton Sea.

3.5 Method

Travel times of the direct, turning, refracted, and reflected arrivals described above were inverted to produce a seismic velocity model of the crust and upper-most mantle. The three-dimensional (3D) inversion approach of *Hole* [1992] and *Zelt et al.* [1996] was used. Travel

times were computed using a finite-difference solution of the eikonal equation [*Vidale*, 1990; *Hole and Zelt*, 1995] using a 100 m grid spacing. Times at receivers are interpolated, and rays are found by tracing through the gridded travel times. All times and rays were traced in 3D to include true shot-receiver offsets on the crooked line, but the velocity model was forced to be two-dimensional (2D) perpendicular to the line. OBS's were receivers for the explosive shots, but were also used as shots computing times via reciprocity for the airgun data.

The first arrivals were inverted using travel time tomography [*Hole*, 1992]. The algorithm uses simple back-projection to distribute the travel-time misfit evenly along the whole ray path. The slowness (inverse of velocity) perturbation in a grid cell is calculated from the mean misfit of all the rays traveling through that cell. Where the receivers were unevenly spaced, a weighting parameter was applied to produce a more even weighting by shot gather. A moving average filter was applied to smooth the velocity perturbation before it is added to the previous velocity model. This procedure is iteratively repeated to generate a new 3D velocity model. The smoothing size of the moving average filter is chosen to be very large in the initial iterations. Smoothing is gradually reduced as the iterations proceed, maintaining a fixed horizontal to vertical aspect ratio. In this manner, misfits are pushed towards large-scale velocity structure, and the starting model for the next iteration is less dependent upon the original starting model. Iteration was stopped when ray smearing begins to appear and/or the misfits approximate the picking errors. This approach produces a model with minimal structure required by the data [e.g., *Zelt*, 1999]. Model resolution is primarily limited by the shot spacing onshore and OBS spacing in the Salton Sea; these are variable along the line.

The starting velocity model was a very smooth, one dimensional (1D) best fit model derived from the first arrival travel times (Figure 3.7b). If the geology varies dramatically along

the seismic profile, different starting models are built for each segment of the profile. For example, the red solid line is for the Imperial Valley, and the red dashed line is for the Coachella Valley, because the data indicate that the Coachella Valley has much thinner sediment and a different crystalline basement. Smooth interpolation was applied between the two starting models at the southern end of the Coachella Valley. A horizontal:vertical smoothing of 3:1 was used, which approximates the average orientation of the ray path, more horizontal than vertical.

The first arrivals ray coverage is much denser in the upper crust than in the middle crust (Figure 3.9). This is due to a decrease in the velocity gradient with depth, constrained by the decreasing curvature of the travel-time curves as a function of offset (Figure 3.7). This also corresponds to the maximum offset at which the densely spaced smaller shots and the airgun data lose signal. To accommodate this difference in data constraints, and to include deeper arrivals, a layer stripping approach was used [*Zelt et al*., 1996; *Zelt*, 1999]. This approach determines the shallow velocity structure based on the best data, then fixes the shallower velocity while modeling deeper structures that have poorer data constraints. The approach was used sequentially for dense first-arrival ray coverage in the upper-most crust, then the sparser first-arrival coverage in the middle to lower crust, then the PmP data for the lower crust and Moho, then the Pn data for the upper mantle.

The velocity structure above the 6 km/s contour was fixed, and first-arrival tomography was continued. Travel-time misfits for those rays that penetrated this artificial, smooth boundary were applied to the portion of the ray path below the boundary. Due to more horizontal ray paths, sparser large shots that have deeper rays, and larger picking errors due to smaller signal strength, a larger smoothing aspect ratio and a smoother final velocity model with lower resolution was derived for the middle crust (Table 3.2). The artificial boundary was smoothed in order to

remove an artificial discontinuity. This ray coverage extended to a velocity of ~6.7 km/s, but did not include Pn velocities above 7 km/s at offsets greater than ~80 km. The exception was the Coachella Valley, where first arrivals do not observe velocity greater than 6.2 km/s nor penetrate as deep (Figure 3.9). No first-arrival ray coverage exists in the middle crust under the Coachella Valley at the depths where faster velocity is observed to the south. However, the observed travel times are inconsistent with faster velocity, thus constraining a much lower maximum velocity in the middle crust.

Three dimensional reflection tomography [*Zelt et al.,* 1996] was used to model the wide-angle reflection travel times from the Moho (PmP). The velocity model was fixed above the 6.7 km/s contour, and extrapolated to depth at 6.7 km/s. The Moho depth was inverted using a horizontal smoothing of of 20-50 km, depending on the reversal shot interval. This boundary was then fixed, and the remaining misfits used to invert for seismic velocity in the lower-most crust, keeping the shallower crust fixed. This new lower-crustal velocity was fixed again to invert for Moho depth. This procedure was iterated until the rms misfit stopped decreasing.

The crustal velocity model and the Moho depth were fixed, and Pn was used to model the upper mantle velocity. The upper mantle velocity was kept very smooth (Table 3.2) because the data reversal distance is ~120 km. However, there is sufficient data coverage to detect a large-scale lateral change in mantle velocity. The data only constrain the upper-most mantle lid and not deeper mantle velocity.

3.6 Seismic velocity model

The seismic velocity model of the entire crust and upper-most mantle (Figure 3.8) was generated from all of the arrivals discussed in section 3.4, using the method described above. Figure 3.9 shows ray coverage, and Figures 3.10 and 3.11 and Table 3.2 show data misfits.

3.6.1 upper crust

Very dense shot, receiver, OBS, and airgun spacing provide excellent ray coverage of the upper crust, to a depth of ~7-8 km (Figure 3.9), corresponding roughly to the 6 km/s contour (Figure 3.8). The shallowest velocity is ~1.8 km/s, representative of unconsolidated valley sediment, but increases rapidly as a function of depth. Details in the sediment are smoothed by the tomography. However, phase "B" in the seismic data (Figures 3.2-3.5) include first arrivals with apparent velocity that increases rapidly and smoothly with distance from 4 to >6 km/s (Figure 3.7). This provides evidence for a strong, smooth velocity gradient with depth, with no evidence for discontinuities. Velocity increases from values typical of unconsolidated sediment to values faster than clastic sedimentary rock, requiring crystalline rock within the bottom part of this gradient zone. Beyond ~4 km/s, the apparent velocity changes more slowly as a function of offset, indicating a decreasing velocity gradient with depth. The 4.0 km/s and overlying contours are relatively flat from the northern Salton Sea to the northern Mexicali Valley, with 4.0 km/s at ~3 km depth. A notable exception is a ~10 km wide zone beneath the Salton Sea geothermal field, where velocity contours <5.0 km/s are ~1.5 km shallower.

However, shallow velocity structure in the Coachella Valley is distinctly different. Sediment thins to the north, and contains local, likely fault-bounded basins. These basins are illustrated by rapid lateral changes in travel time that correlate with receiver position (e.g., at offset of 10 and 30 km to the north in Figure 3.5); these small sub-basins are not well represented

by the velocity model due to the urban noise in the data and the larger smoothing used in the Coachella Valley tomography. The shot gathers show a much sharper increase in apparent velocity from ~2 km/s to ~6 km/s, and velocity near 6 km/s persists out to long offsets. Sedimentary basement has a seismic velocity of 6-6.2 km/s typical of felsic (granitic) crystalline rock. The basement boundary is vertically smoothed by the tomography. A thicker basin and slower basement velocity are indicated at the northern end of the line, where the line obliquely crosses multiple strands of the San Andreas Fault.

The southern end of the line is constrained by a shot in the corner of Arizona that is reversed by several shots in the southern Imperial Valley, but there were no shots for 50 km in Mexico (Figure 3.1). While not as well constrained, velocity contours representing sediment are shallower towards the south end of the line, while underlying contours are deeper (Figure 3.8). This may be due to the Arizona shot being somewhat offline, closer to the edge of the Salton Trough.

3.6.2 middle crust

Below 7-8 km depth, or ~6 km/s, in the Imperial Valley and Salton Sea, the velocity gradient with depth continues to decrease. This means that first arrivals from these depths arrive at much longer offsets and lower amplitudes. They are not recorded from the airguns, and only partly recorded from the small explosive shots due to low signal-to-noise ratio on the OBS records. As a result, the spatial resolution in the middle crust is not as good, and a larger lateral smoothing was used in the tomography (Table 3.2). However, the larger shots indicate that apparent velocity continues to increase with offset (except in the Coachella Valley), but at a slower rate. Beyond ~90 km, the first arrival phase “B” becomes a secondary arrival behind the

upper-mantle refraction (e.g., Figure 3.2 and 3.5 as a long-offset secondary arrival). The maximum apparent velocity of this phase is ~6.8 km/s. This continuous increase in apparent velocity with offset indicates a sufficient velocity increase with depth that first-arrival turning rays provide continuous, overlapping ray coverage down to ~13 km depth (Figure 3.9), where the velocity is ~6.8 km/s (Figure 3.8). While the velocity gradient from 7 to 13 km depth is much smaller than in the upper crust, it is a relatively large gradient for normal continental crust [*Christensen and Mooney*, 1995].

Basement below 6 km/s in the Coachella Valley is very different from that to the south (Figure 3.8). It is characterized by a much smaller velocity gradient, which is directly constrained by the data that do not observe an apparent velocity >6.2 km/s. Although the internal structure of the middle crust is not constrained by turning ray coverage (Figure 3.9), its velocity must be much slower than that beneath the Salton Sea and the Imperial Valley or higher velocity would be observed as first arrivals in the data. The data do not allow velocity >6.5 km/s shallower than ~13 km depth nor velocity >6.8 km/s shallower than ~18 km depth.

The Mexicali Valley is not as strongly different from the Imperial Valley, but also has slower velocity at 9-14 km depth (Figure 3.8). This is in contrast to the shallow velocity, which is a little faster than to the north. The location of this lateral change is not well constrained due to the lack of shots in Mexico, but it is not far south of the USA-Mexico border.

3.6.3 lower crust and Moho

Beneath the Salton Sea and the Imperial Valley, strong first and secondary turning-wave arrivals (phase “B” in Figure 3.5) directly constrain a velocity of 6.7-6.8 km/s at 13 km depth (Figure 3.8). Deeper crustal velocity is constrained by dense, reversed PmP ray coverage (Figure

3.9). As a secondary arrival, PmP has larger picking errors (Table 3.2), and may be consistently picked one or more cycles (~110 ms per cycle) early or late. The estimated picking error and rms misfit (Table 3.2) correspond to ~1 km of uncertainty in Moho depth. The PmP data indicate a relatively flat Moho at 17-18 km depth and a lower crustal velocity of ~6.8 km/s, consistent with the refracted arrivals (Figure 3.8). Beneath the northern Salton Sea, the Moho is 2-3 km deeper and dips to the north, constrained by strong but unreversed reflections recorded by OBS from shots in the southern Coachella Valley. The Moho is shallowest (~17 km depth) beneath the Brawley Seismic Zone, but the difference of <1 km is in the uncertainty range of the model.

The strong PmP reflection at 45-90 km shot-receiver offsets observed in all of the data underlying the Imperial Valley and Salton Sea (Phase D in Figures 3.2, 3.3, and 3.5) is absent in data beneath the Coachella Valley. In the Coachella Valley, deep crustal phases are only observed from two shots with poor data quality, which results in large uncertainties for the middle and lower crustal structure in this area. The first is in shot gather 11620, which observes an unreversed reflection phase F (Figure 3.6), which suggests a reflector at ~28 km depth. The other is shot gather 12220, in which reflection phase G looks similar to PmP to the south, but is at much larger shot-receiver offset and only recorded for ~10 km offset range. The reflector G is roughly at 18-19 km depth and distance of 50-60 km, but no Pn is recognized. We interpret this reflector as the boundary between the middle and lower crust, and the ~28 km deep reflector as Moho, primarily because it is almost as deep as Moho observed in surrounding areas [*Richards-Dinger and Shearer*, 1997].

3.6.4 upper mantle

Pn phases are recorded by 6 shots across an offset range of >20 km, well establishing the apparent velocity, and 3 additional shots with only a short segment (Table 3.1). The low signal strength of Pn, especially on shot 11620 (Figure 3.6), produces a larger picking error. This error is likely correlated within a shot gather, and non-Gaussian due to the possibility of cycle skips. Picking a late cycle is more likely than an early pick. However, the slope of the picks is much better constrained and is the primary constraint on mantle velocity. A uniform upper mantle with a velocity of 7.85 km/s provides an excellent fit to all the Pn phases except shot 10000 (Table 3.2). The modeled Pn travel times are systematically earlier than the picks by almost 100 ms for shot 11620. This is mainly because the middle and lower crust (beneath 10 km depth), through which the 11620 Pn travels, is poorly constrained due to very limited ray coverage (see Figure 3.9).

The apparent velocity of the Pn arrival on shot 10000 is consistent with the same upper mantle velocity, but the Pn arrival times are about 250 ms later than the synthetic arrival time, much larger than the estimated picking error. Unfortunately, this phase is not reversed; no shot recorded Pn on receivers in Mexico. Wide-angle reflections similar to the PmP beneath the Imperial Valley exist beneath the Mexicali Valley (e.g., Figure 3.2), but no shot gather constrains PmP directly beneath the US-Mexico border. While this may be an artifact of shot coverage, it may indicate that the reflectors observed at the same depth north and south of this point are discontinuous. The reflections observed under the Mexicali Valley constrain the depth of the reflector, which is very similar to under the Imperial Valley. Yet, the Pn phase from shot 10000 arrives much too late for this reflector to be the Moho. Because Pn and the reflection has a similar ray path to the reflector, the Pn travel time above the reflector cannot vary much. So the Pn delay must occur below the reflector. For this reason, a velocity of 7.2 km/s was used beneath

the Mexicali reflector, meaning it is not Moho. The location of the change from 7.85 to 7.2 km/s (dotted line in Figure 3.8 at km 190) is poorly constrained. However, moving it further north by ~10 km requires faster velocity (~7.5 km/s) below the Mexicali reflector, and moving it further south cannot effectively delay the Pn from shot 10000, because the Pn ray travels directly to the mantle rather than along the reflector. In addition, velocities greater than 7.8 km/s must be at least 5 km deeper, as indicated by the dotted line at the south end of Figure 3.8.

4. Comparison with previous refraction models

The seismic data and the velocity model in this paper are consistent with the upper crustal model down to 6-8 km depth within the Imperial Valley by *Fuis et al.* [1984] and *Kohler and Fuis* [1986]. This includes the high velocity gradient in the upper crust and basin thickness of 3-5 km. With many more shots and stations, SSIP provides better spatial resolution. However, the middle and lower crust of *Fuis et al.* [1984] is not similar to Figure 3.8, as they locally include a seismic reflector at 11 km depth and regionally include a "sub-basement" refractor with velocity >7 km/s dipping north along the valley at 10-16 km depth. The midpoints of their reflector are to the west of the Imperial Fault, which is outside of the pull-apart basin studied by this paper. East of the Imperial Fault, the seismic data of the two projects contain similar arrivals, but they are interpreted differently here due to SSIP's much denser station spacing that allows excellent correlation of phases. Our shot 10460 (Figure 3.3) was intentionally co-located with shotpoint 6 of *Fuis et al.* [1984], and the reversed line between their shots 6 and 13 is sub-parallel to our line. The dipping 7 km/s refraction from their shot 6 on this line (Figure 3.8 of *Fuis et al.* [1984], which has a different reducing velocity) is consistent with the upper crustal refraction "B" phase in SSIP Figure 3.3; but their reversed refraction arrival from their shot 13 is the PmP phase

described in this paper. This re-interpretation of their arrivals using SSIP's denser data replaces their >7 km/s dipping sub-basement with structure similar to Figure 3.8.

Parsons et al. [1996] analyzed data from a densely sampled profile that started in the southern Imperial Valley and headed northeast into Arizona, and a second profile that ran across the western Imperial Valley and western margin of the Salton Sea and Coachella Valley. The first line densely sampled the middle and lower crust only at the eastern margin and east of the sea. Their line along the axis of the Salton Trough had only 5 shots, and is cited as being poorly constrained. Two reflectors at ~16 and ~22 km were reported along the Salton Trough line. Given the large uncertainty in their middle and lower crustal velocity, and the location of the northern two-thirds of their line at the valley margin, SSIP's results are better constrained and probably more representative of the central axis of the valley.

5. Salton Trough Rift structure and processes

Thick sediment with low seismic velocity (<2 to ~4 km/s) from the Colorado River was deposited in the Salton Trough at a rate of ~2 km/Myr. The minimum sediment thickness as constrained by seismic velocities is ~3 km beneath the Salton Sea, the Imperial Valley and the Mexicali Valley, and only ~1.5 km in the Salton Sea geothermal field. It gradually thins towards the northern Coachella Valley. The seismic velocity continuously increases with depth due to compaction, cementation, and hydrothermal alteration.

Under the Salton Sea and Imperial Valley, sediment velocity increases to ~ 5 km/s at ~4 km depth, which is too high for sedimentary rocks and is likely felsic crystalline rocks. The seismic velocity is still much lower than unfractured granitic rocks [*Christensen and Mooney*, 1995] or than basement in surrounding mountains. Seismic velocity could be reduced due to

fracturing, but it is slow throughout the entire valley, not just the active BSZ. The effects of fractures are likely compensated by hydrothermal alteration. No reflection is observed at the top of the crystalline rocks, which suggests a transitional boundary rather than depositional discontinuity. The crystalline rocks beneath the Imperial Valley are interpreted as young metamorphosed sediment that result from high heat flow in the Salton Trough [*Fuis et al*., 1984]. SSIP constrains the velocity increase with depth with more details than 1979 dataset, but is consistent with and reinforces this interpretation (Chapter 2).

Under the Imperial Valley and Salton Sea, the seismic velocity continues to increase in the middle crust to ~6.8 km/s. The velocity of 6.2-6.6 km/s is consistent with the felsic-intermediate composition middle and lower continental crust of southern California. The velocity gradient with depth is higher than typical continental crust, but might be consistent with stretched continent. Alternatively, this increase in velocity could result from continued metamorphism of basin sediment to higher amphibolite or granulite grade. This layer that could be either stretched pre-existing continent or meta-sedimentary rock is ~5 km thick (Figure 3.12).

The lower crust has a layer ~5 km thick with a seismic velocity of 6.7-6.8 km/s (Figure 3.8), constrained by a 6.8 km/s refracted arrival and by curvature of the PmP travel-times. A velocity >6.7 km/s is consistent with gabbroic rock at the high temperatures expected at depth in the rift, and is not observed elsewhere in southern California crust. This layer is interpreted to be underplated mafic magmatic material associated with partial melt in the rift's upwelling asthenosphere (Figure 3.12). Basaltic xenoliths with mid-ocean-ridge chemistry are found in the Salton Buttes [*Schmitt and Vazquez*, 2006], supporting this interpretation. The upper mantle lid velocity of 7.85 km/s is consistent with high temperature and partial melting. The upper mantle lid velocity of 7.85 km/s is ~3% lower than global average [*Christensen and Mooney*, 1995],

suggesting high temperature and partial melting. Teleseismic body wave tomography indicates upper-mantle seismic velocity at least 2% slower than regional mean from 60 to 160 km depth beneath the Salton Trough [*Schmandt and Humphreys*, 2010].

A very different crystalline rock velocity structure is observed beneath the sedimentary basin of the Coachella Valley. A sharper boundary is indicated by a sharper transition from ~2 km/s phase A to ~6 km/s phase C in the seismic data and very low velocity gradient with depth beneath basement (Figure 3.8). This velocity and gradient are typical of intact felsic crystalline rock. While ray coverage is not very good in the middle crust under the Coachella Valley (Figure 3.9), the first arrival data constrain the velocity from ~7 to ~16 km depth to be slower than that beneath the Salton Sea. If Salton Sea seismic velocity structure existed at the same depths beneath the Coachella Valley, it would create a faster first arrival that is inconsistent with the data (Figure 3.5 and 3.6). For these reasons, despite the lack of turning ray coverage, the velocity model must have much slower velocity under the Coachella Valley than under the Salton Sea (Figure 3.8).

Similarly, the strong PmP reflection observed at 40-80 km offset under the Salton Sea and Imperial Valley is absent beneath the Coachella Valley. The deeper seismic reflector "F" observed on Figure 3.5 at ~28 km depth (Figure 3.8) is interpreted to be Moho. No Pn arrival is observed to confirm this interpretation, but 28 km is almost as deep as the Moho beneath the surrounding ranges [*Richards-Dinger and Shearer*, 1997]. Based on these observations, the Coachella Valley sedimentary basin is interpreted to be deposited on modestly extended pre-existing granitic continental crust typical of southern California (Figure 3.12). The transition between weakly extended pre-existing crust with a deep Moho and strongly attenuated or broken crust with a very shallow Moho is beneath the southern-most Coachella Valley.

Structure beneath the Mexicali Valley is constrained by reversed data, but at a much larger shot spacing (Figure 3.9). Sedimentary structure appears similar to the Imperial Valley, but is only ~3 km thick (Figure 3.8), consistent with a well near the southern-most shotpoint [Pacheco *et al.*, 2006]. The shallowest crystalline rocks increase rapidly to ~6 km/s, then have a much lower gradient than beneath the Imperial Valley (Figure 3.8). This basement structure is more similar to the Coachella Valley. At 10-15 km depth, the velocity is much lower beneath the Mexicali Valley than the Imperial Valley (Figure 3.8). While a strong reflector is observed that resembles the PmP beneath the Imperial Valley, seismic velocity beneath this reflector must be ≥7.2 km/s beneath the reflector beneath the Mexicali Valley (Figure 3.8). The nature of this reflector is unclear, and it is awkward that it is so similar to the Moho to the north, however a clear Pn phase on the southernmost shot requires that the Moho be much deeper beneath the Mexicali Valley (Figure 3.8).

We interpret the lower velocity gradient in the upper crust, lower velocity in the middle crust, and deeper Moho as stretched continental crust (Figure 3.12). It may be thinner than beneath the Coachella Valley, and the lower-most crust has a high velocity that suggests intrusion of mafic rift magmatism. Inline with the SSIP line to the south-southeast is the Altar basin in northern Sonoro [*Pacheco et al*., 2006]. In the northern and central Gulf of California, a series of rift basins along the eastern side of the Gulf became inactive when rifting jumped northwestward to the currently active rift centers ~3 Myr ago [*Stock*, 2000; *Aragon-Arreola and Martin-Barajas*, 2007]. Between these inactive rifts and the active rifts is a thicker block of thinned continental crust [e.g., *Martin-Barajas et al*., 2013]. We interpret the seismic velocity structure and thicker crust beneath the Mexicali Valley as a similar block of stretched continental crust between the older, inactive Altar Basin and active Imperial Valley-Salton Sea rift. The

boundary between this block and the Imperial Valley crust lies close to the Mexico-USA border (Figure 3.12).

The crust and upper mantle model in Figure 3.12, which is parallel to the relative plate motion direction, illustrates a strongly extended rift zone with ~18-km thick crust that is ~100 km wide. The remarkably 1D structure and flat Moho suggests that active extension in the lower crust and upper mantle is widely distributed across this ~100 km width. Because localized Moho topography or mantle velocity anomaly are not observed and the middle crust seems not to be affected by locally focused magmatism, we conclude that there is no localized seafloor spreading center beneath the thick sediment of the Salton Trough. Instead, the lower crust is formed by underplating or distributed intrusion of mafic magma from the hot upper mantle. Based on thermal arguments to avoid melting the overlying felsic rocks, *Lachenbruch et al*., [1985] made a similar conclusion that magmatism must be broadly distributed. The pre-existing continental crust has either totally ruptured or been ductilely stretched to at most 5 km thick. When the brittle part of the pre-existing continent ruptured, deep sediment may have kept the middle and lower crust ductile because of high temperature (Chapter 4). The broadly distributed magmatism and ductile extension in the lower crust contrasts with relatively localized brittle deformation in the Brawley seismic zone and very localized volcanism at the Salton Buttes.

Assuming a constant rifting rate of ~2.6 cm/yr, the current motion on the southern San Andreas Fault, the 100-km wide rift means that the continent broke apart ~4 Myr ago. The Salton Trough rifting rate may have been faster prior to initiation of the San Jacinto Fault ~1 Ma [*Kirby et al*., 2007]. If rifting jumped from the Altar Basin to the Imperial Valley ~3 Ma [*Aragon-Arreola and Martin-Barajas*, 2007], then continental breakup occurred very quickly. This rifting took advantage of older extension in the southern Basin and Range [*Stock*, 2000]. Most (~13 km)

or all of the existing 18-km thick crust formed by sedimentation from above and magmatism from below. Felsic crystalline rocks of this crust include metamorphosed sediment and perhaps pieces of strongly stretched continent. This mostly new crust will eventually become a passive continental margin. This suggests that the stretching of lithosphere may be underestimated in a rift system filled with a large volume of sediment from a river delta.

The cross-section of Figure 3.12 can be compared to similar cross-sections parallel to the relative plate motion direction across other rift segments of the Gulf of California [*Gonzalez-Fernandez et al*., 2005; *Lizarralde et al*., 2007; *Martin-Barajas et al*., 2013]. These sections show a transition from sediment-free in the southern Gulf to sediment-filled in the northern Gulf and Salton Trough. In the southern and central Gulf, the continent has ruptured and seafloor spreading has created hundreds of km of oceanic crust. In some of these rift segments, the continent broke after little extension, creating a sharp boundary between thick continental crust and oceanic crust, while other segments stretched the continent hundreds of km before rupture [*Lizarralde et al*., 2007]. Sediment thickness on these rift segments is 0 km in the southern Gulf to 2-3 km in the central Gulf.

The northern Gulf of California has a sedimentation rate almost as high as the Salton Trough. The northern Gulf contains the inactive Tiburon Basin to the southeast, similar to the Altar Basin, and the active Delfin Basins to the northwest, similar to the active Salton basin. The Tiburon Basin and an intra-basin structural high are both underlain by strongly extended continental crust [*Gonzalez-Fernandez et al*., 2005; *Martin-Barajas et al*., 2013]. In the Delfin Basins, the continent is interpreted to have ruptured relatively recently, creating at most 25-40 km of new crust by magmatism and sedimentation [*Martin-Barajas et al*., 2013]. Stretched continental crust beneath the Mexicali Valley (Figure 3.12), between the inactive Altar and

active Salton basins, is interpreted to be similar to the intra-basin high between the inactive Tiburon and active Delfin basins. However, the Salton basin is interpreted to have broken or almost broken the continent ~3 Myr ago, creating ~100 km of new crust with steep margins to thicker crsut. In comparison, the continent stretched more and broke later in the Delfin Basin. These differences are similar to those observed by *Lizarralde et al.* [2007] in adjacent rift segments in the southern Gulf of California. In both the Delfin and Salton Trough basins, new crust is being created by magmatism and sedimentation, and seafloor spreading has not yet started. The Salton Trough and northern Gulf of California emphasize the important role of river-delta sedimentation upon rifting.

6. Conclusions

The crust is ~18 km thick and roughly one dimensional from the northern Salton Sea to the southern end of the Imperial Valley. In the central Salton Trough, crystalline rocks (>~5.2 km/s) occur at ~4 km depth, and are interpreted to be sediment metamorphosed by high heat flow to ~8 km depth. Crystalline rocks with velocity of ~6.2-6.7 km/s are ~4.5 km thick, and are interpreted to be either stretched pre-existing continental crust or a high-grade metamorphosed sediment. A high velocity of ~6.8 km/s in the lower crust is interpreted as rift-related mafic intrusion by underplating. The upper mantle velocity is 7.85 km/s, indicative of high heat and partial melting. In contrast, in the Coachella Valley, sediment thins to the north, the crust thickens, and the basement is interpreted to be continental granitic crust. The Mexicali Valley is also interpreted to be thicker and composed of stretched continental crust. North American crust has been essentially rifted apart with steep continental margins. Since breakup, an ~100 km wide zone of new crust in the extensional direction has been created by magmatism from below and sedimentation from above. The active rift zone is interpreted to be at least ~100 km wide in the

lower crust and upper mantle, despite the much narrower volcanic, thermal and seismic features in the upper-most crust.

Acknowledgments. This research was supported by NSF MARGINS and EarthScope grants 0742263 to JAH and 0742253 JMS, by NSF Marine Geology and Geophysics grant 0927446 to NWD and by the U. S. Geological Survey's Multihazards Research Progam. We thank the >90 field volunteers and USGS personnel who made data acquisition possible. Numerous landowners allowed access for shots and stations. Seismographs and technical support were provided by the IRIS-PASSCAL instrument facility; special thanks to Mouse Reusch and Patrick Bastien from PASSCAL for their field and data efforts.

References

Aragon-Arreola, M. J., M. T. Morandi-Soana, J. A. Martin-Barajas, L. A. Delgado-Argote, and A. Gonzalez-Fernandez, 2005. Structure of the rift basins in the central Gulf of California: Kinematic implications for oblique rifting, *Tectonophysics*, 409, 19-38.

Bennett, R. A., W. Rodi, and R. E. Reilinger, 1996. Global positioning system constrains on fault slip rates in southern California and northern Baja, Mexico, *J. Geophys. Res*., 101, 21,943-21,960.

Bialas, R. W., and W. R. Buck, 2009. How sediment promotes narrow rifting: Application to the Gulf of California, *Tectonics*, 28, TC4014, doi:10.1029/2008TC002394.

Brothers, D. S., N. W. Driscoll, G. M. Kent, A. J. Harding, J. M. Babcock, and R. L. Baskin, 2009. Tectonic evolution of the Salton Sea inferred from seismic reflection data, *Nat. Geosci*., 2, 581-584, doi:10.1038/ngeo590.

Brothers, D., D. Kilb, K. Luttrell, N. Driscoll, and G. Kent, 2011. Loading of the San Andreas fault by flood-induced rupture of faults beneath the Salton Sea, *Nat. Geosci*., 4, 486-492, doi:10.1038/ngeo1184.

Dorsey, R. J., A. Fluette, K. McDougall, B. A. Housen, S. U. Janecke, G. J. Axen, and C. R. Shirvell, 2007. Chronology of Miocene-Pliocene deposits at Split Mountain Gorge, southern California: A record of regional tectonics and Colorado River evolution, *Geology*, 35, 57-60.

Dorsey, R. J., 2010. Sedimentation and crustal recycling along an active oblique rift margin Salton Trough and northern Gulf of California, *Geology*, 38, 443-446, doi:10.1130/G30698.1.

Dorsey, R. J., and G. Lazear, 2013. A post-6 Ma sediment budget for the Colorado River，*Geosphere*, 9, doi:10.1130/GES00784.1.

Elders, W. A., R. W. Rex, T. Meidav, P. T. Robinson, and S. Bieler, 1972. Crustal spreading in southern California, *Science*, 178, 15-24.

Fuis, G. S., and W. M. Mooney, J. H. Healy, G. A. McMechan, and W. J. Lutter, 1984. A seismic refraction survey of the Imperial Valley region, California, *J. Geophys. Res*., 89, 1165-1189.

Gonzalez-Fernandez, A., J. J. Danobeitia, L. A. Delgado-Argote, F. Michaud, D. Cordoba, and R. Bartolome, 2005. Mode of extension and rifting history of upper Tiburon and upper Delfin basins, northern Gulf of California, *J. Geophys. Res*., 110, 2003JB002941.

Hauksson, E., 2000. Crustal structure and seismicity distribution adjacent to the Pacific and North America plate boundary in southern California, *J. Geophys. Res*., 105(B6):29.

Hauksson, E., J. Stock, R. Bilham, M. Boese, X. Chen, E. J. Fielding, J. Galetzka, K. WHudnut, K. Hutton, L. M. Jones, H. Kanamori, P. M. Shearer, J. Steidl, J. Treiman, S. Wei, and W. Yang, 2013. Report on the August 2012 Brawley Earthquake Swarm in Imperial Valley, Southern California, *Seismol. Res. Lett*., 84(2), 177-189, doi:10.1785/0220120169.

Holbrook, W. S., and P. B. Kelemen, 1993. Large igneous province on the United States Atlantic margin and implications for magmatism during continental breakup, *Nature*, 364, 433-436.

Hole, J. A., 1992. Nonlinear high-resolution three-dimensional seismic travel time tomography. *J. Geophys. Res*., 97, 6553-6562.

Hole, J. A., R. M. Clowes, and R. M. Ellis, 1993. Interpretation of three-dimensional seismic refraction data from western Hecate Strait, British Columbia: Structure of the crust, *Can. J. Earth Sci*., 30, 1427-1439.

Hole, J. A., and B. C. Zelt, 1995. 3-D finite-difference reflection traveltimes, *Geophys. J. Int*., 121(2), 427-434.

Hopper, J. R., T. Funck. B. E. Tucholke, H. C. Larsen, W. S. Holbrook, K. E. Louden, D. Shillington, and H. Lau, 2004. Continental breakup and onset of ultraslow seafloor spreading off Flemish Cap on the Newfoundland rifted margin, *Geology*, 32, 93-96.

Kell, A. M., V. J. Sahakian, G. M. Kent, N. W. Driscoll, A. J. Harding, R. L. Baskin, M. Barth, J. A. Hole, J. M. Stock, and G. S. Fuis, 2016. New Constraints on the architecture and evolution of the Imperial-San Andreas pull-apart system beneath the Salton Sea, California (submitted).

Kirby, S. M., S. U. Janecke, R. J. Dorsey, B. A. Housen, V. E. Langenheim, K. A. McDougall, and A. N. Steely, 2007. Pleistocene Brawley and Ocotillo Formations: Evidence for initial strike-slip deformation along the San Felipe and San Jacinto fault zones, southern California, J. Geol., 115, 43-62.

Lachenbruch, A. H., J. H. Sass, and S. P. Galanis, Jr., 1985. Heat flow in southernmost California and the origin of the Salton Trough, *J. Geophys. Res*., 90, 6709-6736.

Larkin, S. P., A. Levander, D. Okaya, and J. A. Goff, 1996. A deterministic and stochastic velocity model for Salton Trough/Basin and Range transition zone and constraints on magmatism during rifting, J. Geophys. Res., 101, 27, 883-27,897.

Larsen, S., and R. Reilinger, 1991. Age constraints for the present fault configuration in the Imperial Valley, California: Evidence for northwestward propagation of the Gulf of California rift system, *J. Geophys. Res*., 96, 10,339-10,346.

Larson, R. L., H. W. Menard, and S. M. Smith, 1968. Gulf of California: A result of ocean-floor spreading and transform faulting, *Science*, 161, 781-784.

Lekic, V., S. W. French, and K. M. Fischer, 2011. Lithospheric thinning beneath rifted regions of southern California, Science, 334, 783-787, doi:10.1126/science.1208898.

Lin, G., P. M. Shearer, E. Hauksson, and C. H. Thurber, 2007. A three-dimensional crust seismic velocity model for southern California from a composite event method, *J. Gephys. Res*., 112, B11306, doi:10.1029/2007JB004977.

Lin, G., C. H. Thurber, H. Zhang, E. Hauksson, P. M. Shearer, F. Waldhauser, T. M. Brocher, and J. Hardebeck, 2010. A California statewide three-dimensional seismic velocity model from both aboslute and differential times, *Bull. Seismol. Soc. Amer*., 100, 225-240, doi:10.1785/0120090028.

Lizarralde, D., G. J. Axen, H. E. Brown, J. M. Fletcher, A. Gonzalez-Fernandez, A. Harding, W. S. Holbrook, G. M. Kent, P. Paramo, F. Sutherland, and P. J. Umhoefer, 2007. Variation

in styles of rifting in the Gulf of California, *Nature*, 448, 466-469, doi:10.1038/nature06035.

Lonsdale, P., 1989. Geology and tectonic history of the Gulf of California, *in* E. L. Winterer, D. M. Hussong, and R. W. Decker, eds., The Eastern Pacific Ocean and Hawaii, *Geol. Soc. Am., The Geology of North America*, vol. N, p. 499-521.

Lovely, P., J. H. Shaw, Q. Liu, and J. Tromp, 2006. A structural Vp model of the Salton Trough, California, and its implications for seismic hazard, *Bull. Seismol. Soc. Amer*., 96, 1882-1896.

Magistrale, H., H. Kanamori, and C. Jones, 1992. Forward and inverse three-dimensional P wave velocity models of the southern California crust, *J. Geophys. Res*., 97, 14,115-14,135.

Magistrale, H., S. Day, R. W. Clayton, and R. Graves, 2000. The SCEC southern California reference three-dimensional seismic velocity model version 2, *Bull. Seismol. Soc. Amer*., 90, S65-S76.

McMechan, G. A., and W. D. Mooney, 1980. Asymptotic ray theory and synthetic seismogram for laterally varying structures: Theory and application to the Imperial Valley, California, *Bull. Seismol. Soc. Amer*., 70, 2021-2035.

Martin-Barajas, A., M. Gonzalez-Escobar, J. M. Fletcher, M. Pacheco, M. Oskin, and R. Dorsey, 2013. Thick deltaic sedimentation and detachment faulting delay the onset of continental rupture in the Northern Gulf of California: Analysis of seismic reflection profiles. *Tectonics*, 32, 1294-1311, doi:10.1002/tect20063.

Oskin, M., J. Stock, and A. Martin-Barajas, 2001. Rapid localization of Pacific-North America plate boundary motion in the Gulf of California, *Geology*, 29, 459-462.

Oskin, M., and J. Stock, 2003. Miocene to recent Pacific-North America plate motion and opening of the Upper Delfin Basin, northern Gulf of California, Mexico, *Geol. Soc. Amer. Bull*., 115, 1173-1190.

Pacheco, M., A. Martin-Barajas, W. Elders, J. M. Espinosa-Cardena, J. Helenes, and A. Segura, 2006. Stratigraphy and structure of the Altar basin of NW Sonora: Implications for the history of the Colorado River delta and the Salton Trough, *Revista Mexicana de Ciencias Geologicas*, 23, 1-22.

Parsons, T., and J. McCarthy, 1996. Crustal and upper mantle velocity structure of the Salton Trough, southeast California, *Tectonics*, 15, 456-471.

Persaud, P., J. M. Stock, M. S. Steckler, A. Martin-Barajas, J. B. Diebold, A. Gonzalez-Fernandez, and G. S. Mountain, 2003. Active deformation and shallow structure of the Wagner, Consag, and Delfin Basins, northern Gulf of California, Mexico, *J. Geophys. Res*., 108, 2002JB001937.

Richards-Dinger, K. B., and P. M. Shearer, 1997. Estimating crustal thickness in southern California by stacking PmP arrivals, *J. Gephys. Res.*, 102, B7, 15,211-15,224.

Rose, E.J., G.S. Fuis, J.M. Stock, J.A. Hole, A.M. Kell, G. Kent, N.W. Driscoll, M. Goldman, A.M. Reusch, L. Han, R.R. Sickler, R.D. Catchings, M.J. Rymer, C.J. Criley, D.S. Scheirer, S.M. Skinner, C.J. Slayday-Criley, J.M. Murphy, E.G. Jensen, R. McClearn, A.J. Ferguson, L.A. Butcher, M.A. Gardner, I. Emmons, C.L. Loughran, J.R. Svitek, P.C.

Bastien, J.A. Cotton, D.S. Croker, A.J. Harding, J.M. Badcock, S.H. Harder and C.M. Rosa, 2013, Borehole-explosion and air-gun data acquired in the 2011 Salton Seismic Imaging Project (SSIP), southern California-Description of the survey: U.S. Geological Survey Open-File Report 2013-1172, 83pp., http://dx.doi.org/10.3133/ofr20131172.

Robinson, P. T., W. A. Elders, and L. J. P. Muffler, 1976. Quaternary volcanism in Salton Sea geothermal field, Imperial Valley, California, *Geols. Soc. Amer. Bull*., 87, 347-360.

Savage, B., and Y. Wang, 2012. Integrated model for the crustal structure in the Gulf of California extensional province, *Bull. Seismol. Soc. Amer*., 102, 878-885, doi:10.1785/0120110196.

Schmandt, B., and E. Humphreys, 2010. Complex subduction and small-scale convection revealed by body-wave tomography of the western United States upper mantle, *Earth Planet. Sci. Lett*., 297, 435-445.

Schmitt, A. K., and J. B. Hulen, 2008. Buried rhyolites within the active, high-temperature Salton Sea geothermal system, *J. Volcanol. Geotherm. Res.*, 178(4), 708-718.

Schmitt, A. K., and J. A. Vazquez, 2006. Alteration and remelting of nascent oceanic crust during continental rupture: Evidence from zircon geochemistry of rhyolites and xenoliths from the Salton Trough, California, *Earth Planet. Sci. Lett*., 252, 260-274.

Stock, J. M., 2000. Relation of the Puertecitos Volcanic Province, Baja California, Mexico, to development of the plate boundary in the Gulf of California, in Delgado-Granados, H., Aguirre-Diaz, G., and Stock, J. M., eds., Cenozoic Tectonics and Volcanism of Mexico, Geol. Soc. Amer. Special Paper 334, 143-156.

Stock, J. M., and K. V. Hodges, 1989. Pre-Pliocene extension around the Gulf of California and the transfer of Baja California to the Pacific Plate, *Tectonics*, 8, 99-115.

Tape, C., Q. Liu, A. Maggi, and J. Tromp, 2009. Adjoint tomography of the southern California crust, Science, 325, 988-992, doi: 10.1126/science.1175298.

Vidale, J. E., 1990. Finite difference calculation of travel times in three dimensions, *Geophysics*, 55, 521-526.

White, R., and D. Mckenzie, 1989. Magmatism at rift zones: The generation of volcanic continental margins and flood basalts, *J. Geophys. Res*., 94, 7685-7729.

Whitmarsh, R. B., G. Manatschal, and T. A. Minshull, 2001. Evolution of magma-poor continental margins from rifting to seafloor spreading, Natrue, *413*, 150-154.

Zelt, B. C., R. M. Ellis, R. M. Clowes, and J. A. Hole, 1996. Inversion of three-dimensional wide-angle seismic data from the southwestern Canadian Cordillera. *J. Geophys. Res*., 101, 8503-8529.

Zelt, C. A. (1999), Modelling strategies and model assessment for wide-angle seismic traveltime data, Geophys. J. Int., 139, 183-204.

Zhao, D., H. Kanamori, and E. Humphreys, 1996. Simultaneous inversion of local and teleseismic data for the crust and mantle structure of southern California, *Phys. Earth Planet. Int*., 93, 191-214.

Figure 3.1

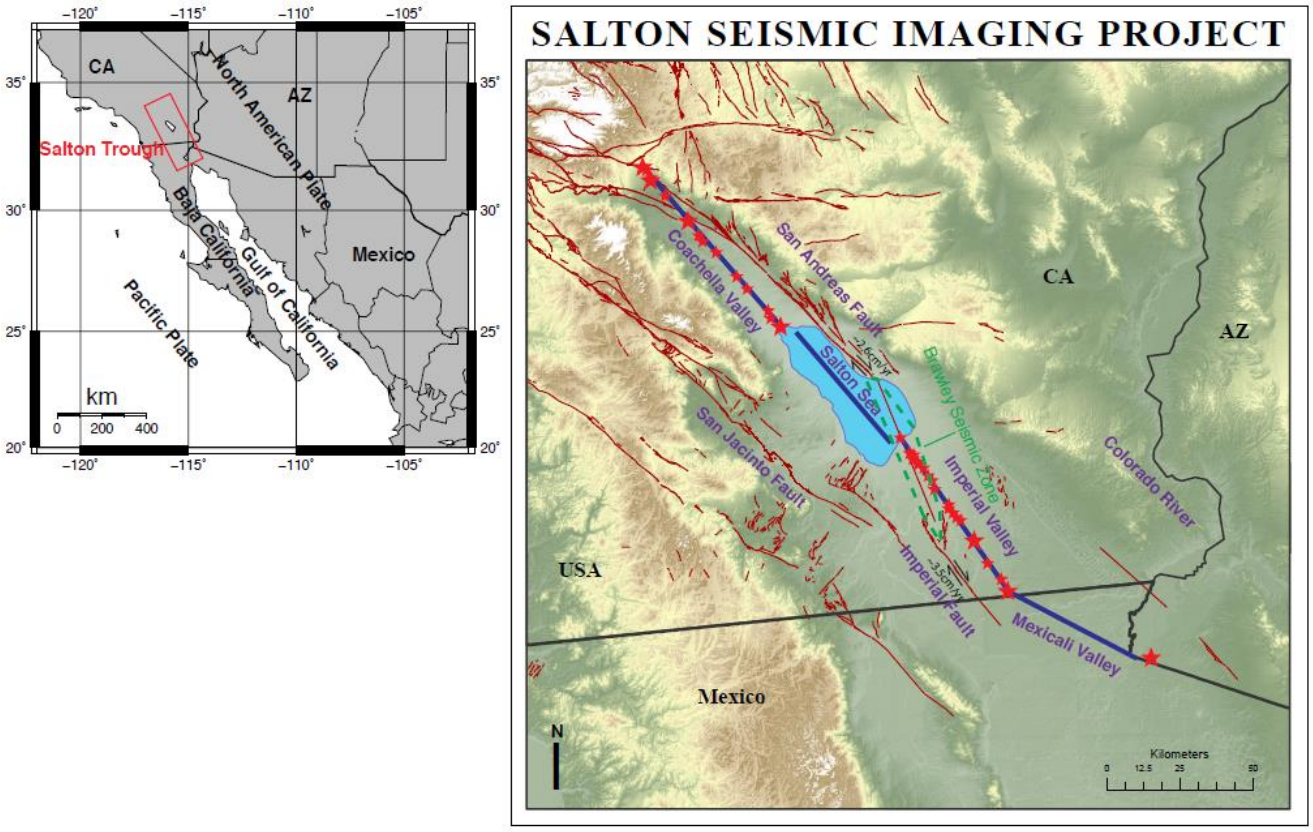

Salton Seismic Imaging Project (SSIP) study area and Line 1 deployment. SSIP Line 1 and active faults in the Salton Trough. Red stars are explosive shots, and larger stars correspond to larger shots. Blue lines are onshore seismographs and airgun shots in the Salton Sea. Note, AZ, Arizona; CA, California.

Figure 3.2

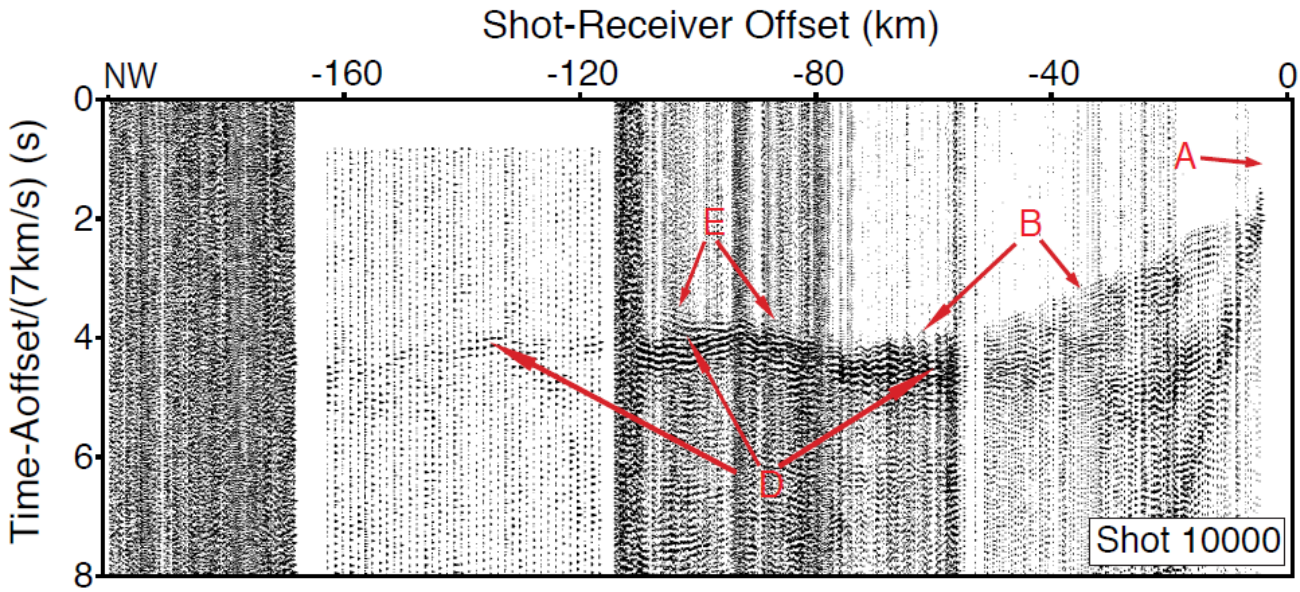

Seismic data for shot 10000. X-axis is shot-receiver offset with negative value to the northwest, and y-axis is travel time reduced by 7 km/s. The data are bandpass filtered by an Ormsby filter 5-8-20-30 Hz. Seismic arrivals are interpreted in the main text: A, direct or turning wave in sediment; B, turning waves in the crystalline crust; B', multiple of B in the sedimentary basin; C, refracted arrival in the Coachella Valley; D, reflection from the moho; E, refraction from the upper mantle; G, possible deep crustal reflection. Those phase labels also apply for following figures.

Figure 3.3

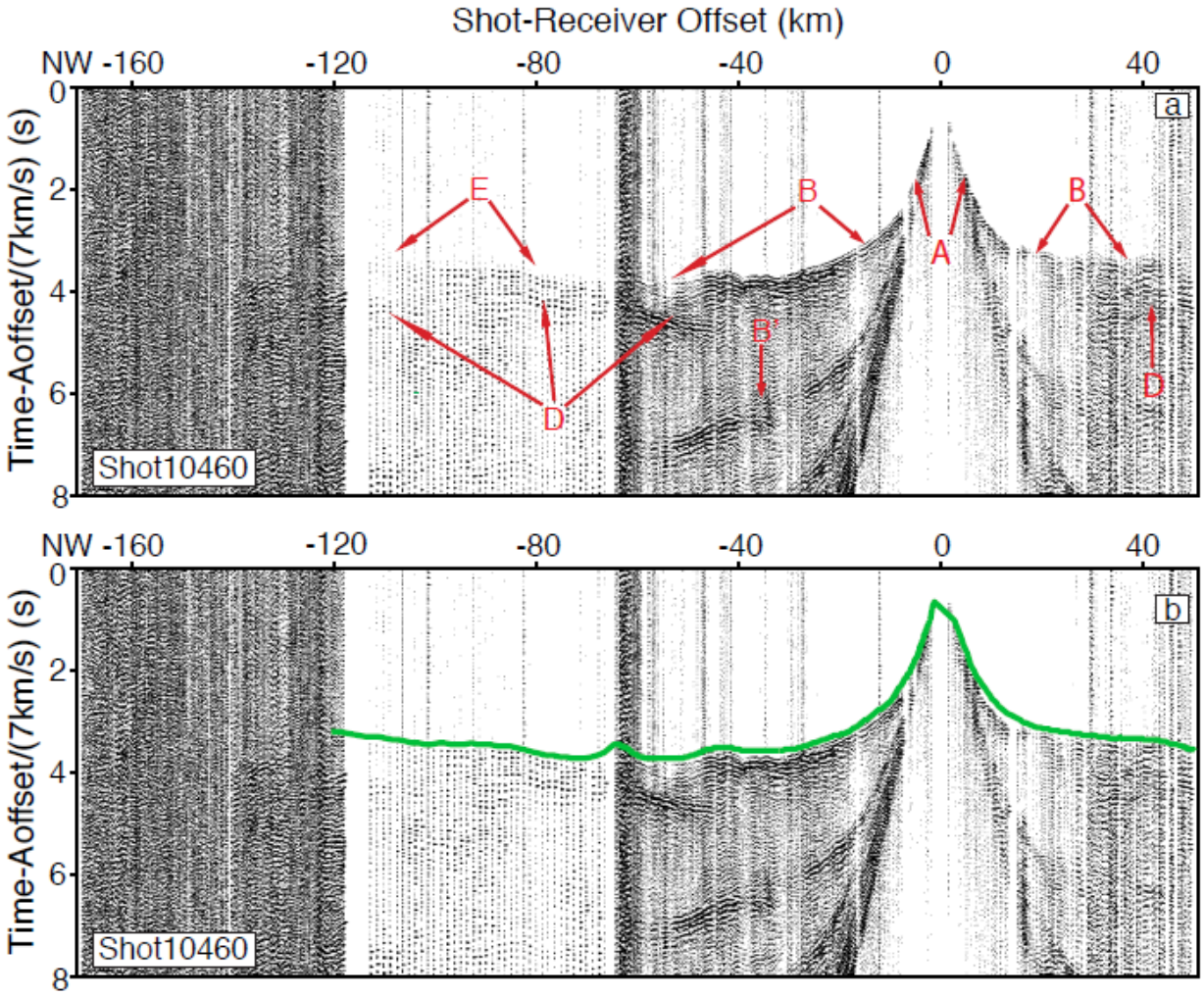

Seismic data for shot 10460. It is plotted as in Figure 3.2. (a) raw data, and (b) data with superimposed arrival times computed from the model of Figure 8.

Figure 3.4

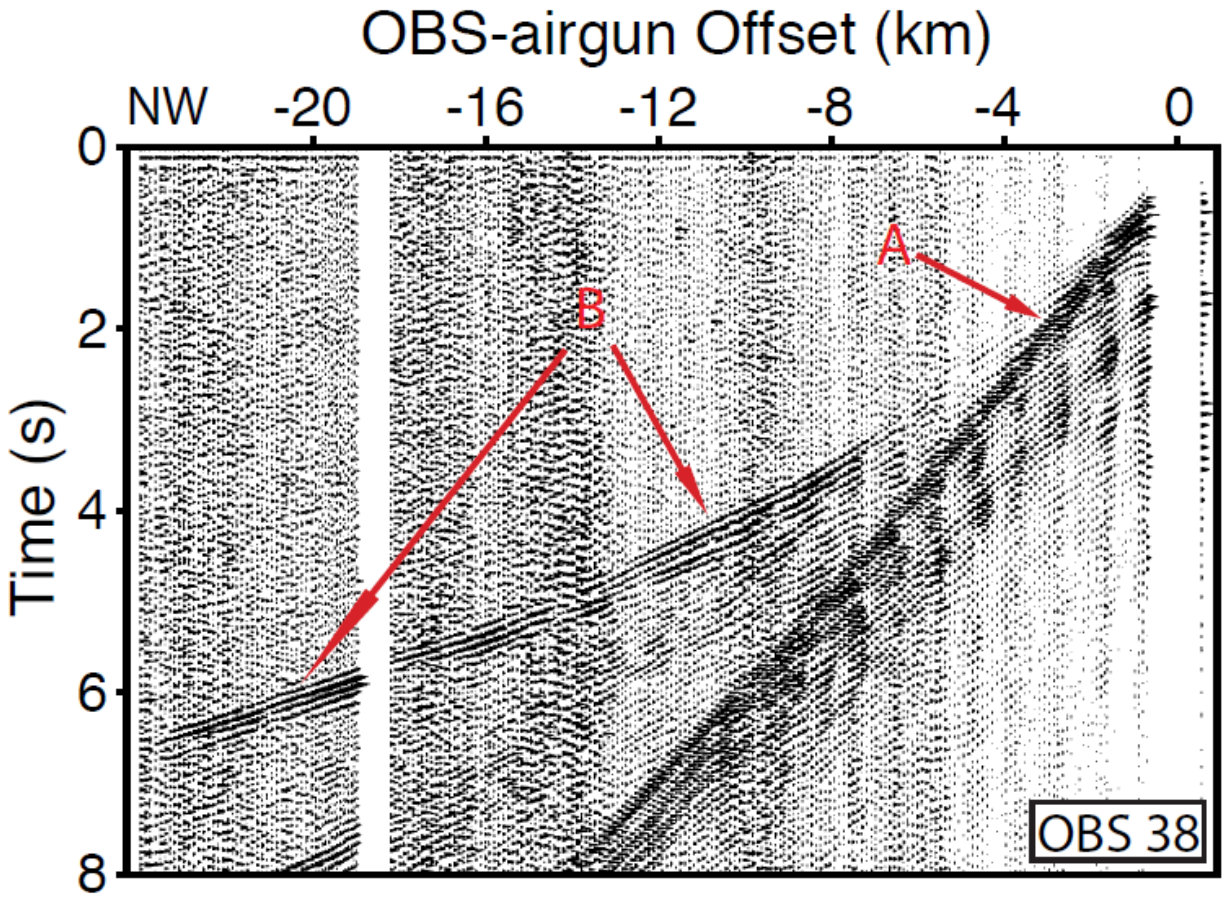

Seismic data for airgun shots recorded on OBS 38. It is plotted as in Figure 3.2 but filtered to 5-8-15-18 Hz.

Figure 3.5

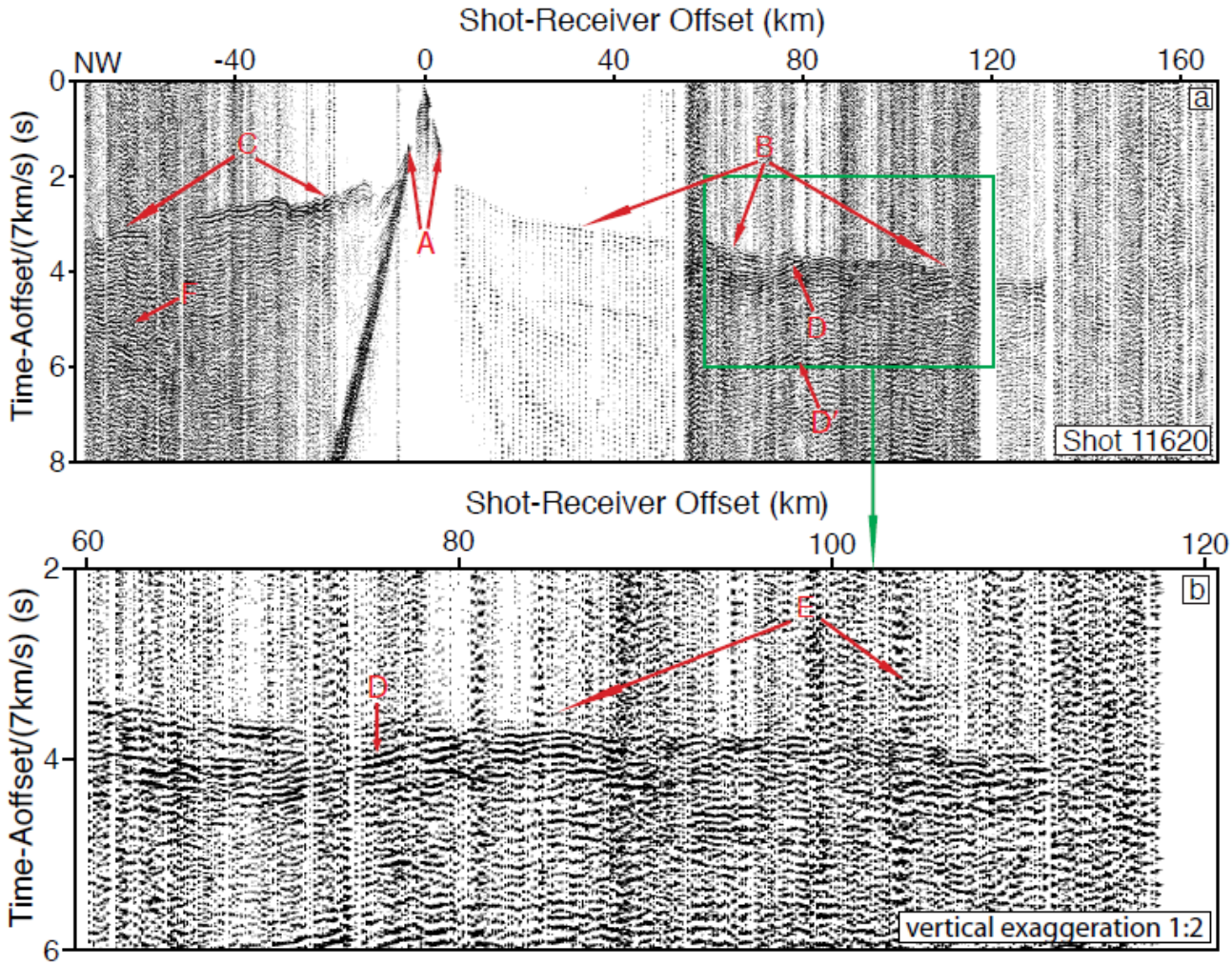

Seismic data for shot 11620. It is plotted as in Figure 3.2.

Figure 3.6

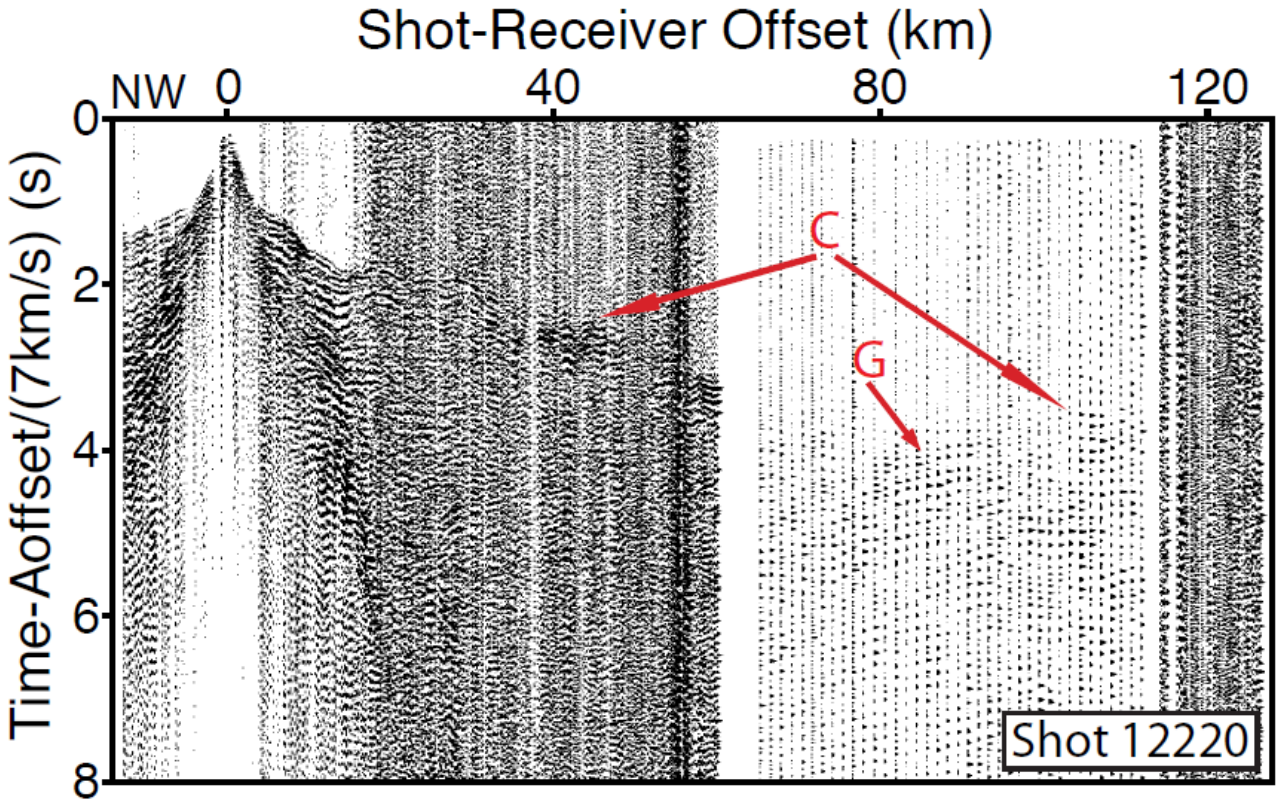

Seismic data for shot 12220. It is plotted as in Figure 3.2.

Figure 3.7

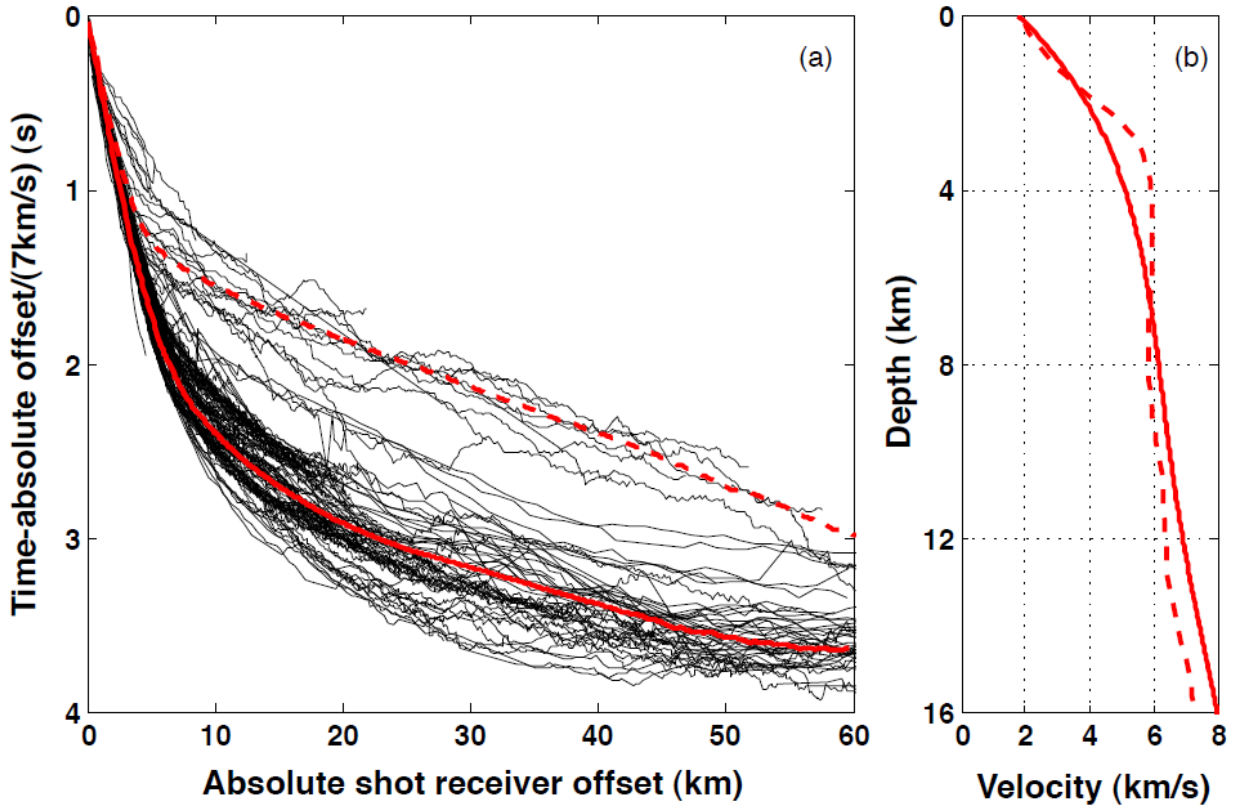

1D starting velocity model. a) Short-offset first arrival travel times. Black lines correspond to different shots, different directions from each shot. Thick red lines are synthetic first arrival travel times, corresponding to the velocity models in panel b. b) 1D starting velocity models for the crustal tomography in the Salton Sea, Imperial Valley and Mexicali Valley (red solid line) and Coachella Valley (red dashed line).

Figure 3.8

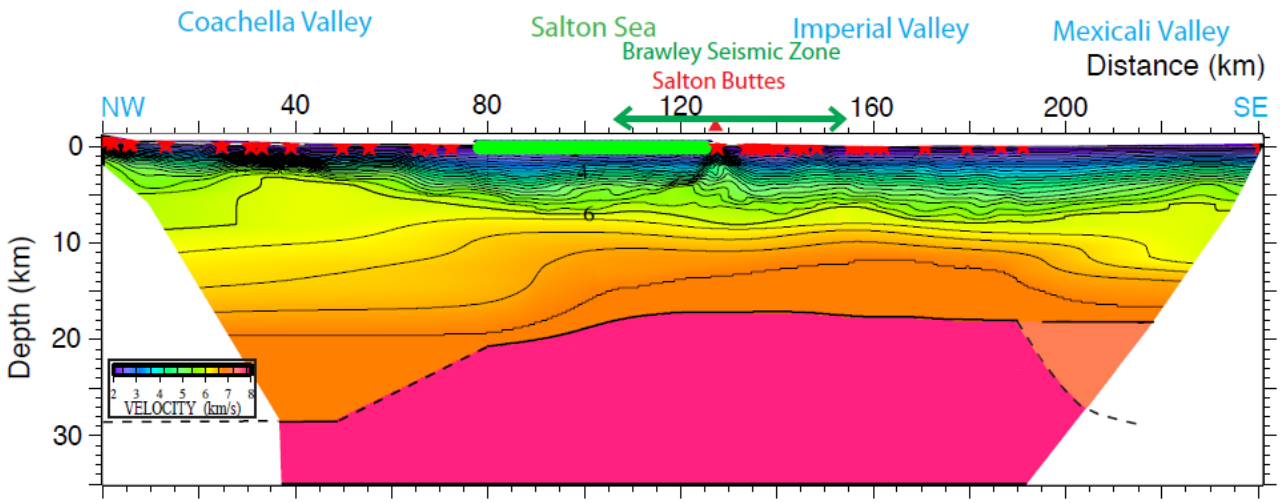

Seismic velocity model along the axis of Salton Trough. Red stars are explosive shots, and green circles are OBS locations. Contour interval is 0.2 km/s. The thick black line below 6 km/s is the strong reflector, dashed where not directly constrained. Regions without ray coverage are white.

Figure 3.9

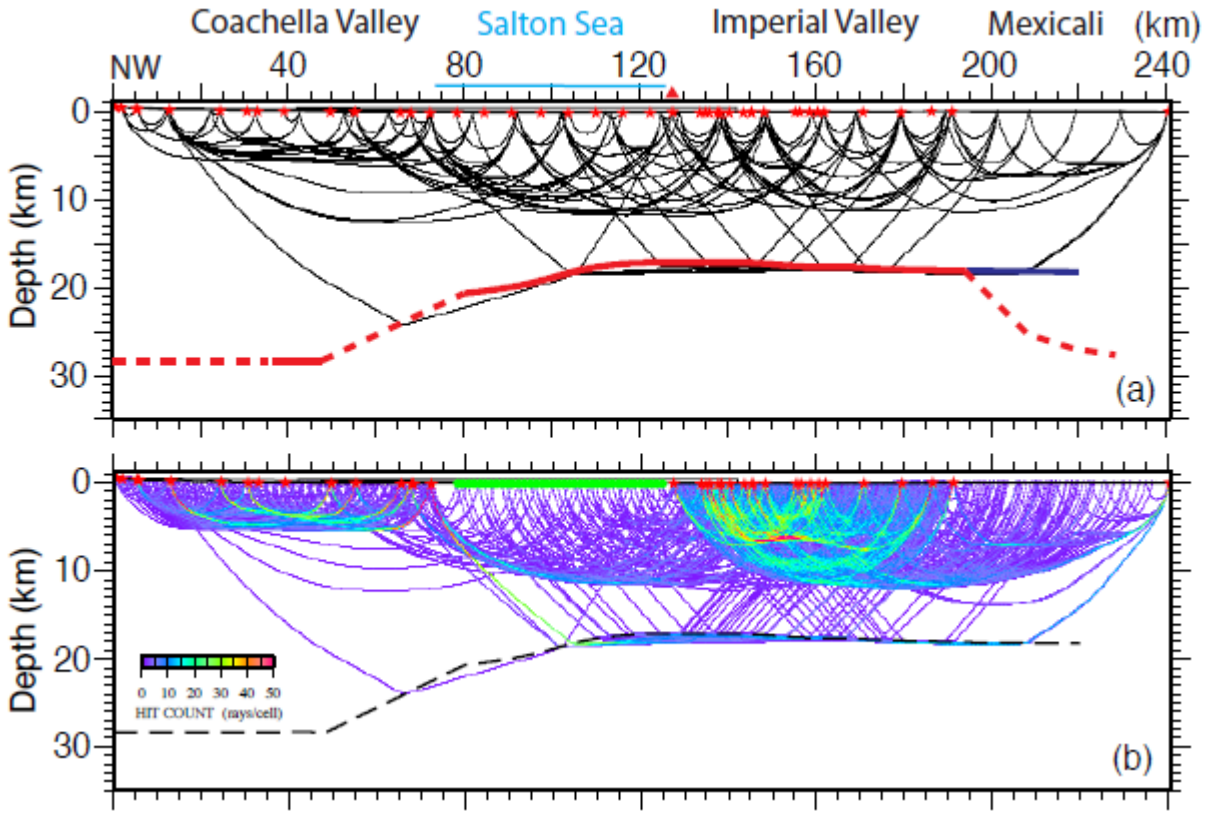

First arrival ray coverage. (a) First-arrival ray coverage, including mantle Pn, in the velocity model shown in Figure 3.8. (b) Hit count is for 0.1 km grid cells. Red stars are the shots and green circles are the OBS. For clarity, rays to only every 10th onshore receiver, only every 2nd OBS, and only every 10th airgun shot are traced.

Figure 3.10

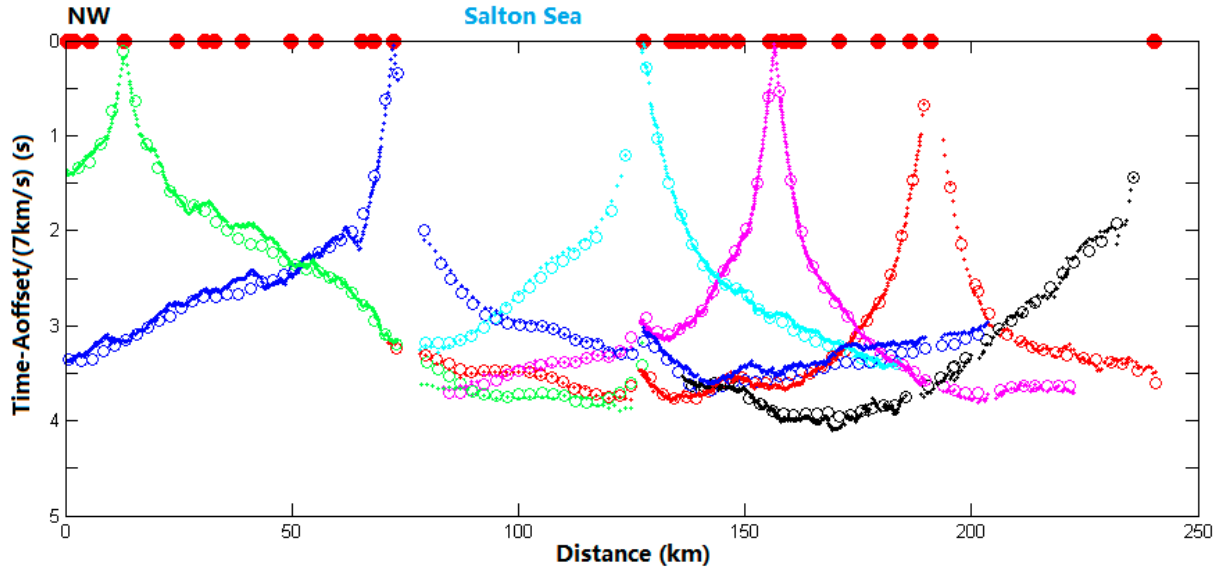

Comparison of first arrival picks and synthetic travel times. First arrival, including Pn, picks and synthetic travel times of 6 shot examples, are shown with a reduced travel time of 7 km/s. Picks are plotted at the location of the receiver. Red solid circles are shots. Dots in different colors are picks, and circles are corresponding synthetic travel times for different shots. Synthetic travel times only every 3 km are plotted for clarity.

Figure 3.11

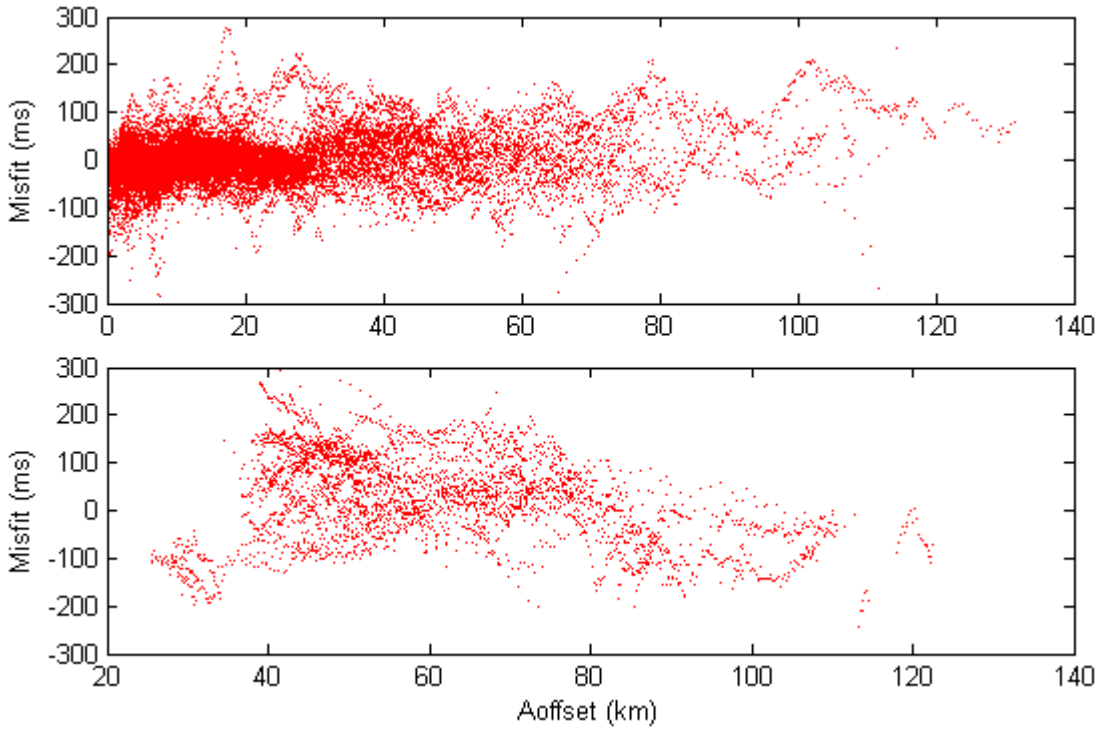

Seismic velocity model misfit. Misfit vs. absolute shot-receiver offset for (a) first arrivals, including Pn and (b) PmP.

Figure 3.12

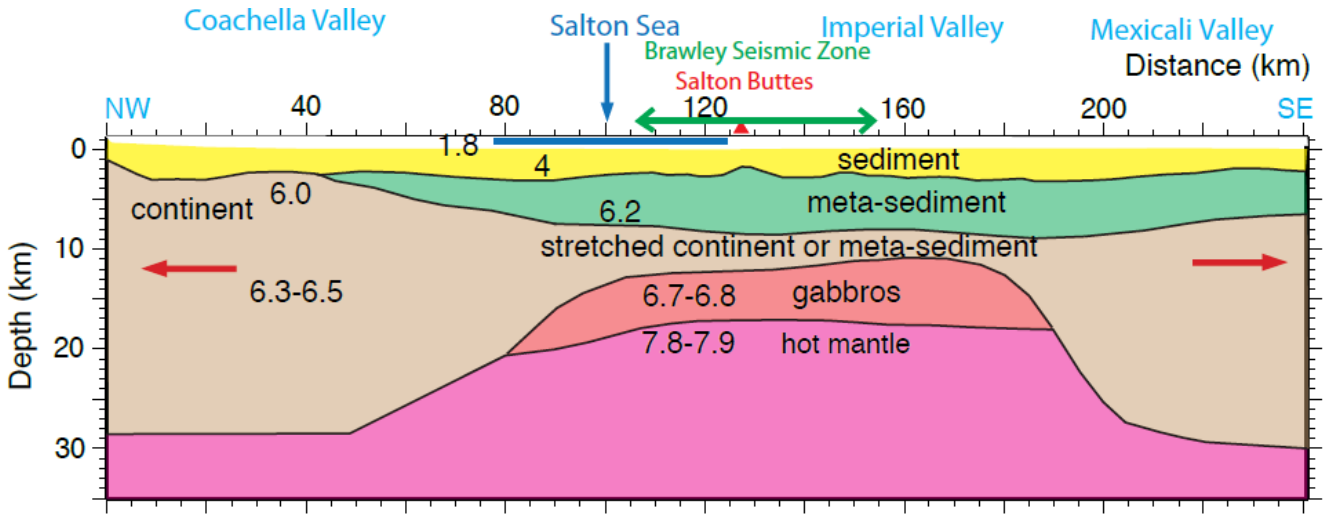

Geological interpretation of the rifting process from the velocity model. The sediment thins and the metamorphosed sediment pinches out towards Coachella Valley. The current and pre-existing upper crust has ruptured with normal faults developed down to ~10 km. The pre-existing lower crust is possibly left in the middle crust and stretched over a broad area due to high temperature. Limited sills and dikes probably intrude the lower mafic crust and the middle crust.

Table 3.1 Shot information

Shot ID	Size (kg)	Picks Offset Range (km)	Deep Crustal Phases
10000	1440	(-150, 0)	Pn, PmP
10460	1367	(-130, 50)	Pn, PmP
10510	229	(-120, 60)	Pn, PmP
10580	229	(-110, 60)	Pn, Pmp
10670	458	(-100, 70)	Pn, PmP
10750	116	(-90, 30)	PmP
10770	104	(-90, 80)	Pn, PmP
10790	69	(-90, 70)	Pn, PmP
10810	115	(-90, 70)	PmP
10830	115	(-90, 80)	PmP
10900	115	(-70, 90)	PmP
10931	229	(-80, 90)	PmP
10932	229	(-70, 70)	PmP
10950	115	(-80, 90)	PmP
10980	115	(-80, 80)	PmP
10990	115	(-70, 80)	PmP
11000	115	(-80, 80)	PmP
11020	115	(-70, 80)	PmP
11030	115	(-70, 90)	PmP
11050	120	(-70, 80)	PmP
11100	181	(-50, 80)	PmP
11620	416	(-80, 130)	Pn, PmP, PmP2
11650	115	(-50, 100)	Pn, PmP
11680	116	(-60, 90)	NA
11800	69	(-60, 90)	PmP
11860	115	(-50, 80)	PmP
11960	5	(-10, 10)	NA
12000	137	(-10, 10)	NA
12050	229	(-30, 50)	NA
12100	456	(-20, 40)	NA
12220	115	(-20, 120)	NA
12290	456	(-10, 30)	NA
12300	81	(-10, 30)	NA
12330	230	(-3, 5)	NA
12341	1367	(0, 10)	NA
12342	456	(0, 10)	NA

In total, 36 shots were fired along this line. Negative offset for picks is for stations to the north of the shot, while positive is to the south. Pn is refraction from the Moho; PmP is reflection from

the Moho beneath the Salton Sea and Imperial Valley, and PmP2 is reflection from the Moho beneath the Coachella Valley.

Table 3.2 Model resolution and parameters

Model depth	Smoothing ratio	Resolution/smoothing size (horizontal/vertical)	Picking uncertainty	RMS misfit
Upper crust	3:1	5km/1km	40-50 ms	34 ms
Middle crust	10:1	20km/2km	100 ms	85 ms
Lower crust and Moho	20:1	20km/1km	220 ms	230 ms
Upper mantle	20:1	100km/5km	220 ms	70 ms

Chapter 4

The effects of thick sediment upon continental breakup: kinematic and thermal modeling of the Salton Trough, southern California*

Abstract

A one-dimensional time-dependent numerical model is developed to simulate the rifting process and thermal evolution of the Salton Trough. Based upon a new seismic velocity model, the rifting model assumes that the addition of underplated mafic magma and deposited sediment compensate for thinning of the crust during extension. The modeled heat flow is most consistent with field measurements if the middle crust is stretched pre-existing continental crust. The crustal rheology calculated from lithology and the modeled temperature shows that deformation in the lower crust in the Salton Trough is currently ductile. The same extension mechanism could continue for millions of years if there is sufficient sediment supply. Rapid sedimentation delays the breakup of the continental crust and prevents the initiation of seafloor spreading by maintaining the thickness of the extended crust. This process probably created passive continental margins globally.

Keywords: active rifting, continental breakup, sedimentation, Salton Trough, thermal modeling, numerical modeling

* An edited version of this chapter will be submitted to *Geology*. Han. L., R. P. Lowell, J. A. Hole, and J. M. Stock. The effects of thick sediment upon continental breakup: kinematic and thermal modeling of the Salton Trough, California.

4.1 Introduction

The Salton Trough is the northern end of the Gulf of California extensional province [e.g., *Elders et al.*, 1972; *Lonsdale*, 1989; *Stock and Hodges*, 1989; *Larsen and Reilinger*, 1991]. It results from the oblique extension along the entire length of the Gulf of California rift system between North American and Pacific plates in last 6.3 Ma [*Oskin et al*., 2001; *Oskin and Stock*, 2003]. The rift system has evolved into full seafloor spreading in the southern Gulf. In the Salton Trough and the northern and central Gulf, the pull-apart rifts are covered by at least 4-8 km thick sediments [*Fuis et al.*, 1984; *Gonzalez-Fernandez et al.*, 2005; *Lizarralde et al.*, 2007; *Han et al.*, in preparation], and seafloor spreading has not begun.

The whole crustal and upper mantle structure across the rift center in the central Salton Trough has recently been imaged [*Han et al.*, 2016]. The results indicate that new crust is formed by sedimentation from above and magmatism from below and that homogenous lower crust and upper mantle extends laterally for ~100 km. This inferred crustal and upper mantle structure is consistent with widely distributed magmatism and ductile deformation. Figure 1 depicts this seismically inferred one-dimensional crust and upper mantle structure, where the black box outlines the model space.

Lachenbruch et al. [1985] developed a one-dimensional steady state analytical model of basin formation in the Salton Trough, based on the crustal velocity model by *Fuis et al.* [1984]. This kinematic model (referred to as L's model in the later text) provided a robust explanation for the high heat flow of ~140 mW/m^2 in the Salton Trough; however, the recent seismic model has modified and better constrained some of the model parameters. In this paper, we develop a one dimensional numerical scheme following *Lachenbruch et al.* [1985] to simulate both steady-state

and non-steady-state conditions. First, we build a thermal model using the new constraints to test whether the L's model results hold. Then we compare the models with and without sedimentation, to show the effects of thick sediment on the rifting processes.

4.2 Method

The kinematic model for the rifting process is based on several explicit assumptions briefly described here. The justification of these assumptions and more details on the method can be found in *Lachenbruch et al.* [1985]. 1) The lower crustal mafic magmatism and upper crustal sediments simultaneously compensated for the thinning of the crust in a certain ratio during extension. 2) As the basin extended, all layers of the crust thinned uniformly, or the fracturing of the brittle part of the crust could be simulated by ductile thinning. 3) The crust is incompressible, so the total volume of the crust doesn't change during extension. 4) The crust has remained predominantly solid. 5) The magmatic material in the lower crust was added by uniform underplating from the mantle. 6) The upper mantle temperature remained close to the basalt solidus during the extension.

The recent seismic model shown in Figure 1 strongly supports assumptions 1, 4, 5, and 6 and partially supports assumption 2. The basement density is ~2700 kg/m^3 at the sediment basement boundary at ~2.75 km depth [*Tarif et al.*, 1988; *Han et al.*, 2016], so the density increase down to the middle crust is less than 5%, which justifies assumption 3.

In addition to these main assumptions, we use a constant temperature boundary condition at the base of the crust, assuming that the system is heated by the latent heat of magmatic intrusion and the conductive heat flux from mantle. We recognize that crustal radioactivity may contribute ~15 mW/m^2 to the heat flow [*Lachenbruch et al.*, 1985; *Sass et al.*, 1984], suggesting

a reduced heat flow of ~125 mW/m^2 in the Salton Trough. We assume that hydrothermal circulation that is evident in the small zone identified as he Salton Sea geothermal field [*Newmark et al.*, 1988] is not wide spread throughout the crust. Hence, the model neglects the effects of hydrothermal circulation of the thermal evolution of the crust. For simplicity, we assume that the pore space of the sediment has been mostly closed by compaction and mineral reactions at the time of deposition.

From a reasonable starting condition, if the numerical model reaches a quasi steady state, that result should be the same as the L's model. The code is described in detail below. Although we use a different approach, the modeled extension mechanism is the same as the L's model.

We construct a one-dimensional, time-dependent model in which the crust is homogeneous in the lateral direction for all properties, including temperature, composition and density. The values and units of those and other model parameters are listed in Table 1. In this model the crustal thickness h(t) and L(t), the length over which the crust extends, are treated as functions of time t. We consider a constant rate of extension v, resulting in a strain rate r = v/L(t). For a sedimentation rate S, and rate of magmatism M, the fraction of sediment in the newly formed crust Ø = S/(S+M). After extension over a small time step Δt, the length of the new extended crust is L(t)+vΔt. The new crust then consists of the thinned original crust and the newly added crust via sedimentation and magmatism. That is:

$$h(t+\Delta t) = h(t)\frac{L(t)}{L(t)+v\Delta t} + (S+M)\Delta t \qquad (1)$$

For a non-steady state condition, the crustal thickness may increase or decrease with time. At steady state, however, h(t) and L(t) are both constant, so h(t+Δt) equals h(t). From equation (1) and the definition of Ø, we have

$$S = h(t)\frac{v}{L(t)+v\Delta t}\varnothing \quad (2a)$$

$$M = h(t)\frac{v}{L(t)+v\Delta t}(1-\varnothing) \quad (2b)$$

For a given depth z(t) in the crust, thinning of the crust brings it shallower to the surface whereas sedimentation forces it deeper. So after a small time step Δt,

$$z(t+\Delta t) = z(t)\frac{L(t)}{L(t)+v\Delta t} + S\Delta t \quad (3)$$

As shown in Figure 2, the crust thins from the black solid box into the blue dash box. Meanwhile, sedimentation from above and magmatism from below compensate the thinning of the crust. This process pushes the layers originally near surface deeper, and brings the layers originally near the bottom of the crust shallower. At some depth z_0, which depends on the model parameter values, material is stationary in time and does not move either upward or downward. The further from this fixed depth, the faster the vertical movement. This process significantly promotes the heat transfer from the hot lower crust to the cold upper crust, by pushing the cold sediment deeper and bringing the hot gabbros shallower.

The vertical movement and thermal conduction both contribute to the thermal evolution of the crust. In the model, the thermal conduction between adjacent cells is simulated first, using the one-dimensional heat conduction equation:

$$\frac{\partial T}{\partial t} = \mathrm{a}\frac{\partial^2 T}{\partial^2 z} \quad (4)$$

where temperature T is a function only of time t and depth z, and the term $a = k/\rho c_p$ is the thermal diffusivity, where k is the thermal conductivity, ρ is the rock density, and c_p is the specific heat.

In a small time step Δt, the extension thins every cell, but doesn't change the temperature and other properties of that cell. Then cold sediment with temperature T_0 is added on the surface, and hot magma with temperature T_b at the base of the crust. This new crust column is re-gridded into normal cell size x, assuming perfect mixing of temperature, density and other physical properties. After that, the temperature of the surface cell is reset to surface temperature T_0, and the temperature of the bottom cell is reset to the basalt solidus temperature T_a. The basalt solidus temperature T_a is calculated by

$$T_a = T_m(0) + G_m h(t) \tag{5}$$

The adjusted magma temperature T_b is

$$T_b = T_m(0) + G_m h(t) + \frac{L_a}{c} \tag{6}$$

where $T_m(0)$ is adjusted basalt solidus temperature at the sea level, G_m is the gradient of solidus, h(t) is the crust thickness, and L_a/c is the ratio of the latent heat to the specific heat of basaltic magma [*Lachenbruch et al.*, 1985].

4.3 Benchmark with the L's model

Lachenbruch et al. [1985] showed the geotherms for different strain rates, assuming a constant temperature boundary condition and a uniformly extending crust with sedimentation and underplating, in their Figure 18. The L's model results are shown by green lines in Figure 3, for strain rates of 10, 50%/Myr, which correspond to extension rates of 1 and 5 cm/yr for an extensional length of 100 km. The geotherms from this study are shown by red lines. They are quasi-steady-state results after 10 Myr simulation time, with a starting temperature profile linearly from 0 °C at the surface to the basalt solidus at the base of the crust. Clearly, our

numerical method has successfully reproduced the L's model results. The model parameters used in this benchmark are shown in Table 2.

4.4 Salton Trough result

4.4.1 Steady state

As we now have a benchmarked numerical scheme, we can model the steady state geotherms in the Salton Trough, using the new constraints. As shown in Figure 1, the extensional length L(t) is 100 km in the extensional direction. The extension rate v is ~2.6 cm/yr, based on the current slip rate along the San Andreas Fault [*Bennett et al.*, 1996]. The crust thickness h(t) is ~17.5 km, with ~8 km thick sediment or metamorphosed sediment and ~5 km thick mafic lower crust on average. The ~4.5 km thick middle crust is either pre-existing crust or predominantly higher grade metamorphosed sediment. If the middle crust is pre-existing crust, the ratio Ø equals 0.62. If the middle crust is mostly metamorphosed sediment, the ratio Ø is ~0.71. Other model parameters are listed in Table 3.

The results for both cases are shown as red and green solid lines in Figure 4, respectively. The yellow dashed line is a normal geotherm with gradient of 25 °C/km, and the blue dashed line corresponds to a conductive heat flow of 125 mW/m^2. It takes only about 1 Myr for the temperature profile to get very close to the steady state result, which suggests that the system can quickly reach quasi-steady state. The temperature profile for the sedimentary middle crust case is slightly colder, because of more sediment subsidence than the pre-existing crust case. The conductive heat flow estimated for the sedimentary middle crust case is 96.4 mW/m^2, and that for the pre-existing middle crust case is 111.6 mW/m^2. This is generally consistent with field measurements, although the sedimentary middle crust case is slightly colder.

L's model provided a heat flow consistent with field measurements, for a wide range of ratio Ø and extension rate v. A much thinner crust than that estimated from *Fuis et al.* [1984] normally will result in a much higher heat flow. However, the modeled heat flow in this study is slightly lower. This is because the ratio Ø from the current seismic model is also much greater than the previous estimation. The ratio Ø in the L's model is 0.4, which means the magmatism is 1.5 times the sedimentation, whereas the ratio in this study is 0.62 for the pre-existing middle crust case and 0.71 for the sedimentary middle crust case, indicating that the magmatism is less than 56% of the sedimentation. The new crustal model suggests that the upper crust is significantly cooled as a result of more rapid sedimentation. In order to support the surface high heat flow, both magmatic latent heat and about 100 mW/m^2 mantle heat flux are required. While in L's model, the magmatic latent heat alone would melt significant amount of lower crust, due to the low ratio Ø.

If the crust has reached steady state, it will consist of only sediment and magmatic material. However, in the pre-existing middle crust case, significant amount of pre-existing crust exists. In addition, a magma generation rate of 6.7 km^3 per km extension per km length of rift is required to maintain the crust thickness. This is probably too high for the Salton Trough, because the crust is much thicker and the upper mantle is slower and colder than that at mid-ocean ridges. So we propose to explore the non-steady state condition with a lower magma generation rate for the pre-existing crust case in the following section.

4.4.2 Non-steady state

The numerical scheme described above enables us to simulate non-steady state conditions; but to implement the model, two additional assumptions are needed. There are: 7) the rates of

sedimentation and magmatism are proportional to the extension rate and 8) the extensional length L(t) grows with time.

We explore a wide range of magma generation rates along with corresponding initial crustal thickness and rift width at the onset of magmatic intrusion, as shown in Table 4. Different initial crust thickness and rift width is required by each model, in order to result in the current crustal structure at a given simulation time. We do not expect significant amount of magmatism to occur in the Salton Trough when the crust is much thicker than 30 km, which is close to the regional average crustal thickness [*Richards-Dinger and Shearer*, 1997], so the magma generation rate in model A is probably a minimum estimate.

The surface heat flow at the time when the model approaches the current crustal structure (Table 4) is generally consistent with the field measurement of 125 mW/m^2. The modeled heat flow decreases slightly as the magma generation rate increases. This occurs because heat is provided by a constant temperature boundary, which is independent of the magma generation rate. Moreover, in this model, a faster magma generation corresponds to faster sedimentation because of constant ratio Ø, which simultaneously makes the lower crust warmer and the upper crust cooler.

The results of model B with a magma generation rate of 6.0 km^3 per km extension per km length of rift are shown in details as an example. The thickness evolution of each layer with time is shown in Figure 6. Note that the original crust is thinning with time, and the middle crust is 4.5 km thick at present. The rift zone width increases linearly with time, because we use a constant extension rate of 2.6 cm/yr. The temperature and yield strength profiles after 1 and 2 Myr simulation time and the present, which is after ~3.2 Myr simulation time, are shown in Figure 6.

The heat flow estimated from the present geotherm is 108.0 mW/m^2. The crustal yield strength is calculated from the modeled temperature, following *Buck* [1991]. The upper and middle crust is assumed to be mainly dry quartzite, and the mafic lower crust is assumed to consist of 40% pyroxene and 60% anorthosite. The crustal yield strength indicates that the crust is dominated by ductile stress at depth. This result is consistent with the seismic interpretation that the deformation in the lower crust is ductile [*Han et al.*, 2016].

4.5 Discussion

The natural cycle of Colorado River flowing into and out of the Salton Trough has been about every 400-500 years and has repeated itself many times historically. This may change due to control by engineers in modern times. To explore the effects of sedimentation on the rift processes, we run two simulations from present state, one with the same sedimentation rate and one without sedimentation. A magma generation rate of 6.0 km^3 per km extension per km length of rift is used. The temperature profiles and the corresponding crustal yield strength after 10 Myr from present for both cases are shown in Figure 7. For the case without sedimentation, the crust will thin to ~9 km, and the crust will be dominated by brittle stress. This condition violates the assumption 2, suggesting that if the extension continues in the same rate, the continental crust in the Salton Trough will probably break up some time in the next 10 Myr. For the case with the same sedimentation rate, the crust will thin by only ~1.5 km, and the crustal rheology calculations suggest that the same extension mechanism could continue for at least another 10 Myr. With a greater magma generation rate, the crustal thinning will be even less significant. The temperature profile approaches a linear gradient after 10 Myr simulation time. This is because the thickness of new sedimentation and magmatism is much less, when they are distributed in a ~3 times broader rift zone. The temperature difference between two cases is really subtle, but the

thin crust results in a dominantly brittle rheology. In conclusion, the rapid sedimentation delays the breakup of the continental crust, and prevents the initiation of mid-ocean ridges, by maintaining the thickness of the extended crust. When the crust rheology changes, the extension rate may also change for a rift driven by local magmatism. However, in the Salton Trough, the rift is driven by far field extensional stress, which is independent of the local condition.

4.6 Conclusions

A one-dimensional numerical kinematic, thermal, and rheologic model is developed for the rifting process in the Salton Trough. In the model, the crust stretches uniformly, and new crust is added by sedimentation from above, magmatism from below, and metamorphism of the sediment. A thin layer of stretched continental crust remains in the middle crust. The model is consistent with the observed heat flow and seismic velocity structure. Rheology calculated from the modeled temperature and seismically observed composition supports the interpretation that deformation in the lower crust in the Salton Trough is ductile. This process is stable for millions of years as long as the sediment supply is maintained. In conclusion, rapid sedimentation delays final breakup of the crust and prevents the initiation of seafloor spreading by maintaining the thickness of the extending crust and keeping the crust predominantly ductile. This process probably occurs wherever a large river flows into a rift during continental breakup. It may explain passive margin structure in many global locations, including the Gulf of Mexico.

Acknowledgments. This research was supported by NSF MARGINS and EarthScope grants 0742263 to JAH and 0742253 JMS, by NSF Marine Geology and Geophysics grant 0927446 to NWD and by the U. S. Geological Survey's Multihazards Research Progam.

References

Bennett, R. A., W. Rodi, and R. E. Reilinger, 1996. Global positioning system constrains on fault slip rates in southern California and northern Baja, Mexico, *J. Geophys. Res*., 101, 21,943-21,960.

Buck, W. R., 1991. Modes of continental lithospheric extension, *J. Geophys. Res*., 96, 20,161-20,178.

Elders, W. A., R. W. Rex, T. Meidav, P. T. Robinson, and S. Bieler, 1972. Crustal spreading in southern California, *Science*, 178, 15-24.

Fuis, G. S., and W. M. Mooney, J. H. Healy, G. A. McMechan, and W. J. Lutter, 1984. A seismic refraction survey of the Imperial Valley region, California, *J. Geophys. Res*., 89, 1165-1189.

Gonzalez-Fernandez, A., J. J. Danobeitia, L. A. Delgado-Argote, F. Michaud, D. Cordoba, and R. Bartolome, 2005. Mode of extension and rifting history of upper Tiburon and upper Delfin basins, northern Gulf of California, *J. Geophys. Res*., 110, 2003JB002941.

Han, L., J. A. Hole, J. M. Stock, G. S. Fuis, G. M. Kent, N. W. Driscoll, A. Kell, M. J. Rymer, A. Gonzalez-Fernandez, and O. Lazaro-Mancilla, 2016. Crustal and upper mantle velocity structure during active continental rifting in the Salton Trough, southern California (in preparation).

Lachenbruch, A. H., J. H. Sass, and S. P. Galanis, Jr., 1985. Heat flow in southernmost California and the origin of the Salton Trough, *J. Geophys. Res*., 90, 6709-6736.

Larsen, S., and R. Reilinger, 1991. Age constraints for the present fault configuration in the Imperial Valley, California: Evidence for northwestward propagation of the Gulf of California rift system, *J. Geophys. Res*., 96, 10,339-10,346.

Lizarralde, D., G. J. Axen, H. E. Brown, J. M. Fletcher, A. Gonzalez-Fernandez, A. Harding, W. S. Holbrook, G. M. Kent, P. Paramo, F. Sutherland, and P. J. Umhoefer, 2007. Variation in styles of rifting in the Gulf of California, *Nature*, 448, 466-469, doi:10.1038/nature06035.

Lonsdale, P., 1989. Geology and tectonic history of the Gulf of California, *in* E. L. Winterer, D. M. Hussong, and R. W. Decker, eds., The Eastern Pacific Ocean and Hawaii, *Geol. Soc. Am*., *The Geology of North America*, vol. N, p. 499-521.

Newmark, R. L., P. W. Kasameyer, and L. W. Younker, 1988. Shallow drilling in the Salton Sea region: the thermal anomaly, J. Geophys. R., 93, 13005-13023.

Oskin, M., J. Stock, and A. Martin-Barajas, 2001. Rapid localization of Pacific-North America plate boundary motion in the Gulf of California, *Geology*, 29, 459-462.

Oskin, M., and J. Stock, 2003. Miocene to recent Pacific-North America plate motion and opening of the Upper Delfin Basin, northern Gulf of California, Mexico, *Geol. Soc. Amer. Bull*., 115, 1173-1190.

Richards-Dinger, K. B., and P. M. Shearer, 1997. Estimating crustal thickness in southern California by stacking PmP arrivals, *J. Gephys. Res.*, 102, B7, 15,211-15,224.

Stock, J. M., and K. V. Hodges, 1989. Pre-Pliocene extension around the Gulf of California and the transfer of Baja California to the Pacific Plate, *Tectonics*, 8, 99-115.

Tarif, P. A., R. H. Wilkens, C. H. Cheng, and F. L. Paillet, 1988. Laboratory studies of the acoustic properties of samples from Salton Sea Scientific Drilling Project and their relation to microstructure and field measurements, J. Geophys. R., 93, 13057-13067.

Figure 4.1

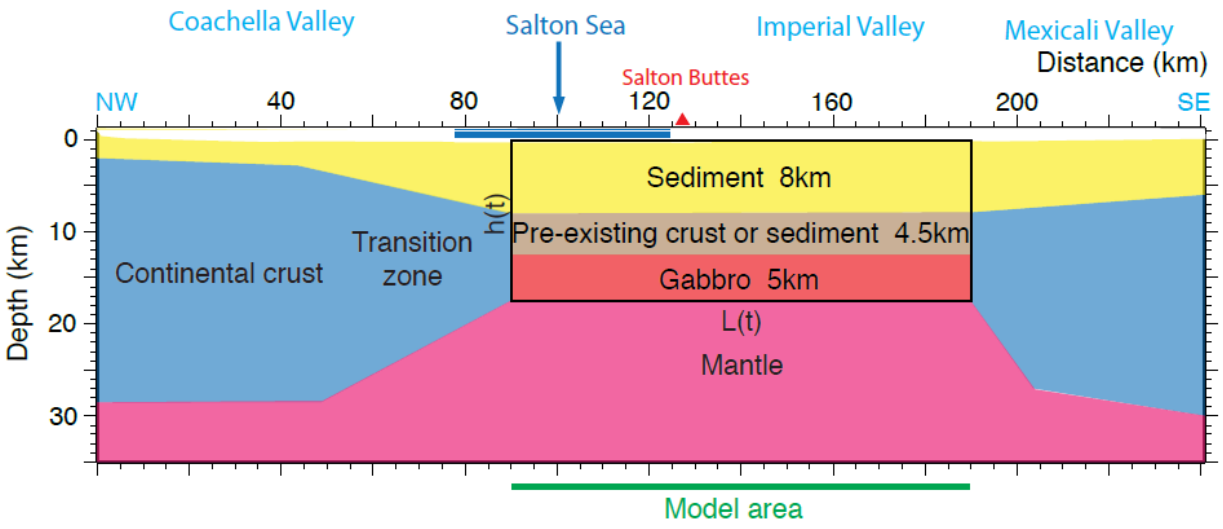

A sketch of the crustal structure across the rift in the Salton Trough from Chapter 3. The model space is shown by the black box.

Figure 4.2

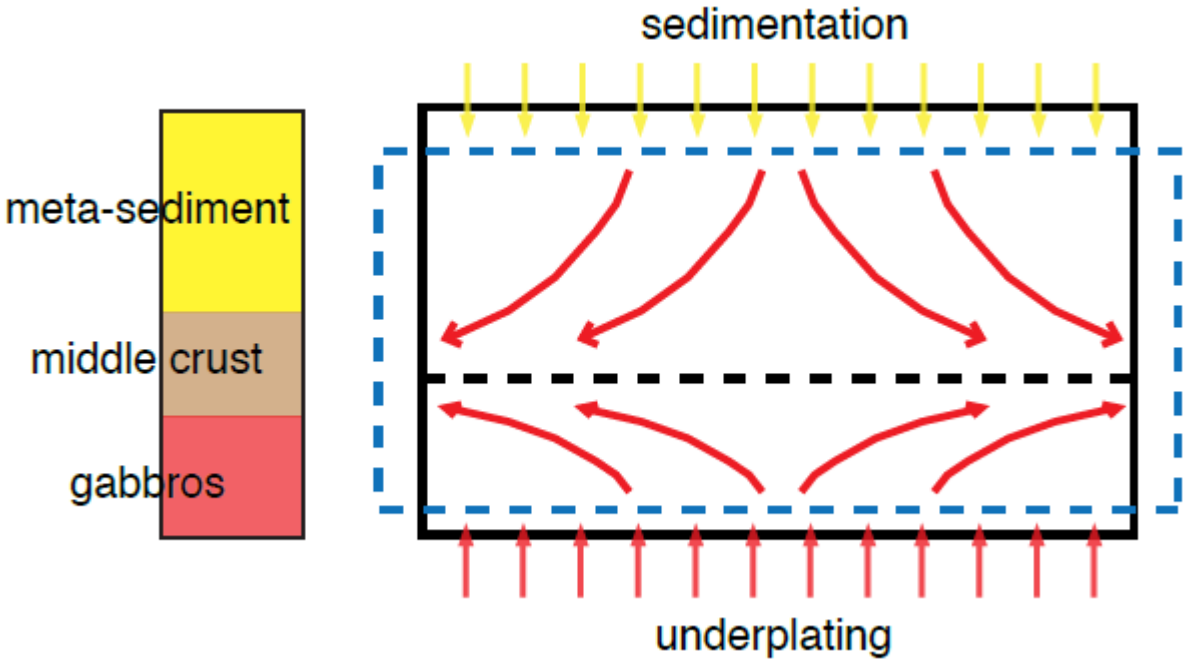

The simplified one dimensional extensional mechanism in the kinematic model. Crust thins from the black box to blue dash box during extension. The sedimentation and magmatic underplating compensate the crustal thinning simultaneously.

Figure 4.3

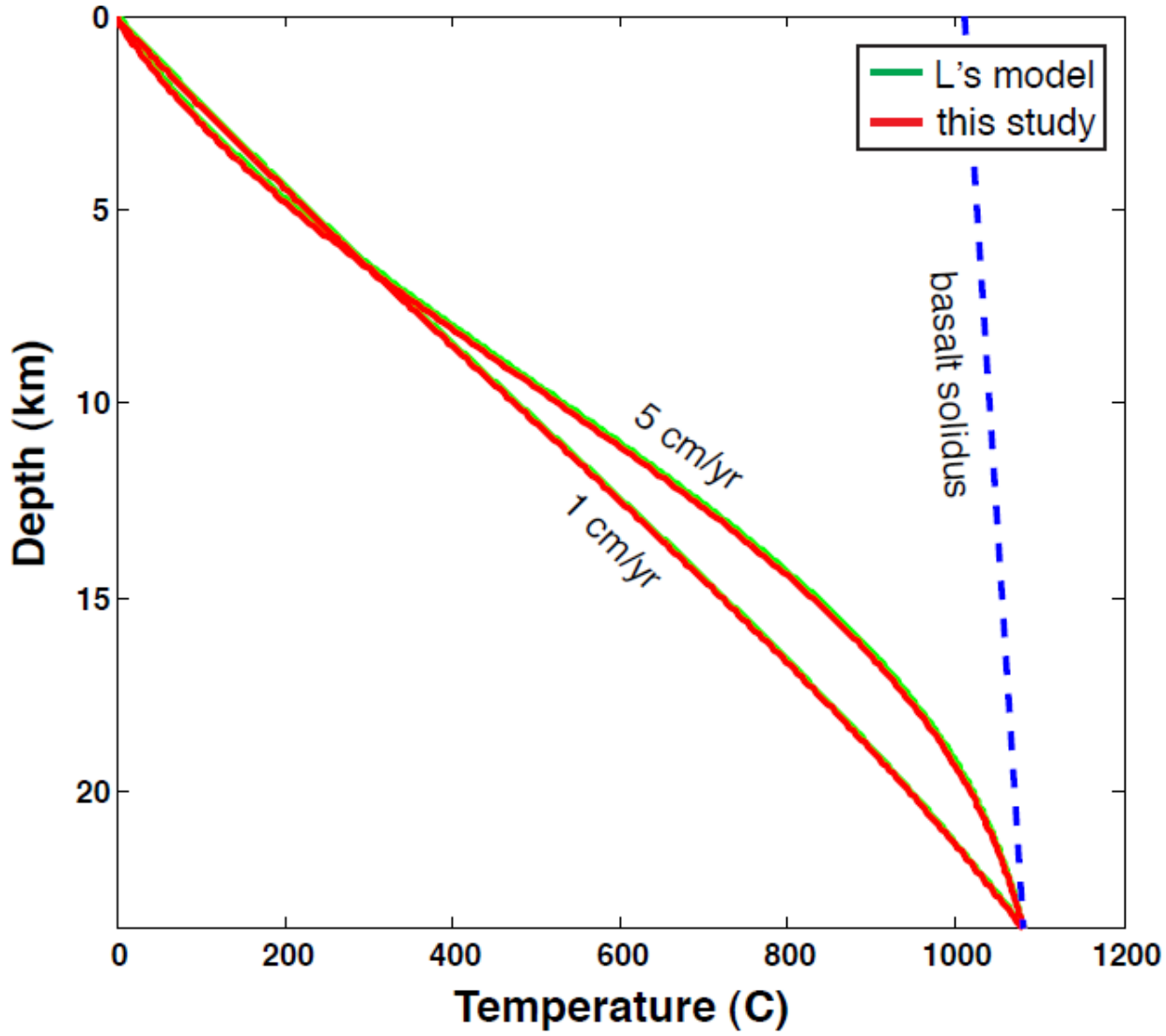

Benchmark with the L's model. The L's model results are in green, and those from this study are in red. The blue dashed line is the basalt solidus. Two extensional rates are simulated.

Figure 4.4

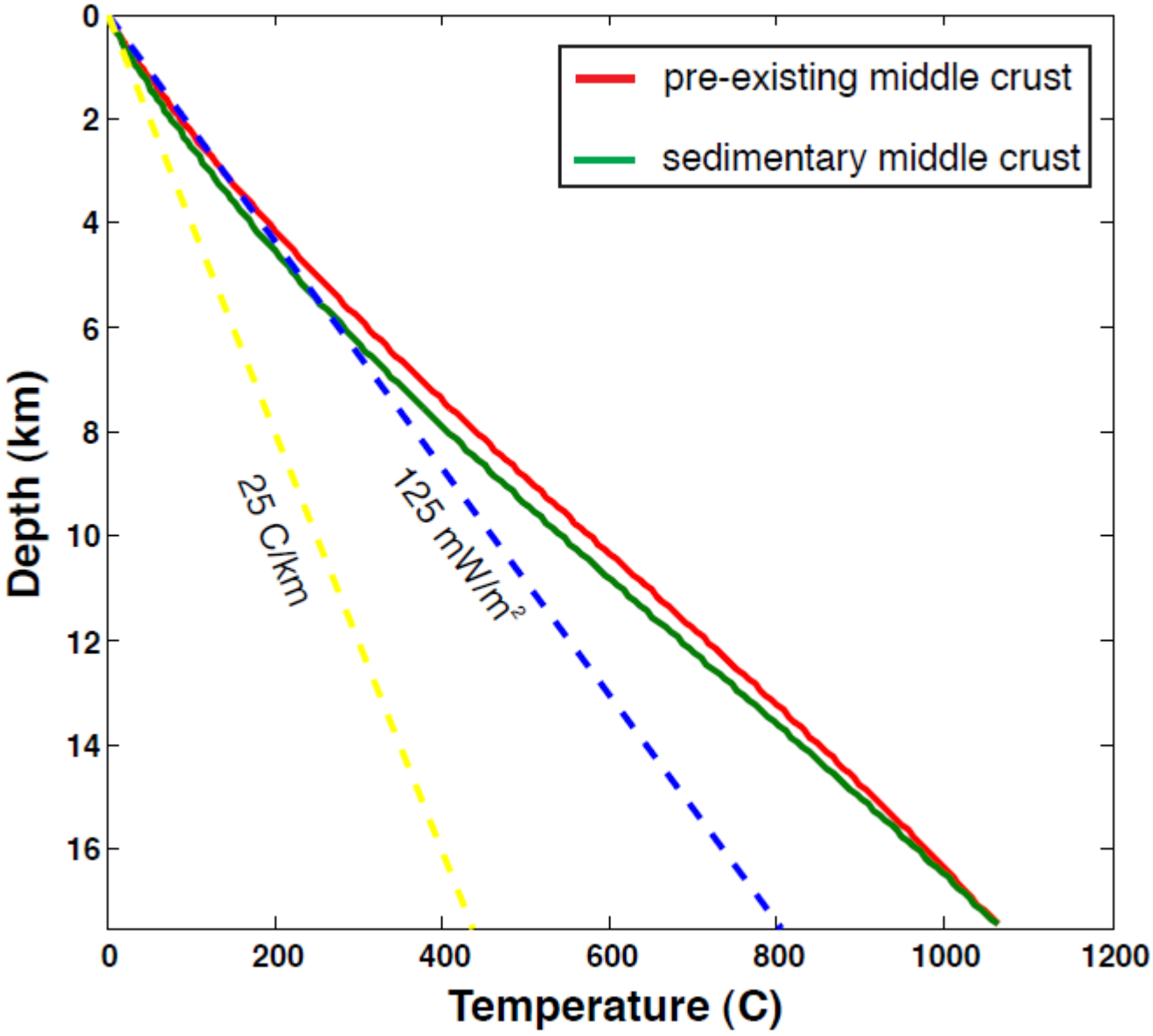

The steady state geotherm for the Salton Trough using the new constraints. The case that the middle crust is pre-existing crust is shown in green, and the case that the middle crust is predominantly sedimentary is shown in red. The blue dashed line corresponds to the geotherm for conductive heat flow of 125 mW/m^2. The yellow dashed line is a linear geotherm of 25 °C/km.

Figure 4.5

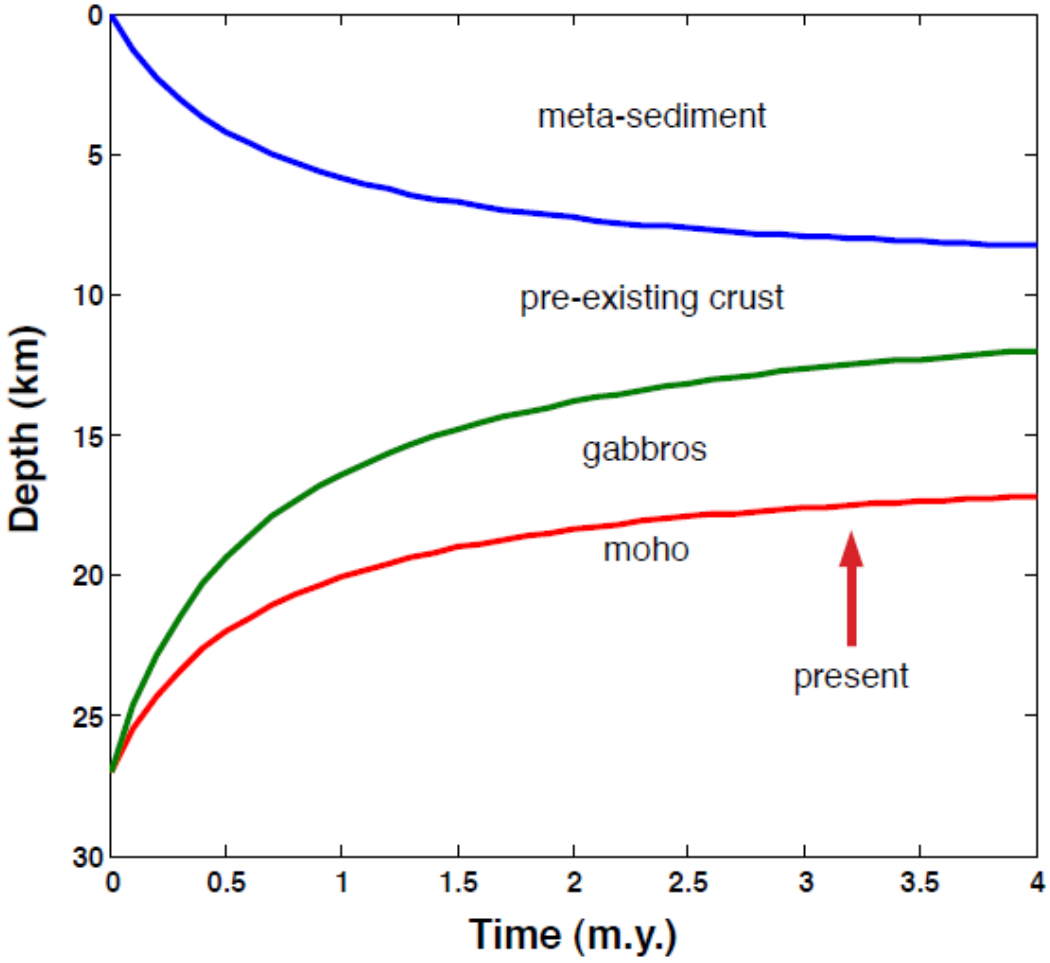

Crustal structure evolution with simulation time. This is for Model B in Table 4.4.

Figure 4.6

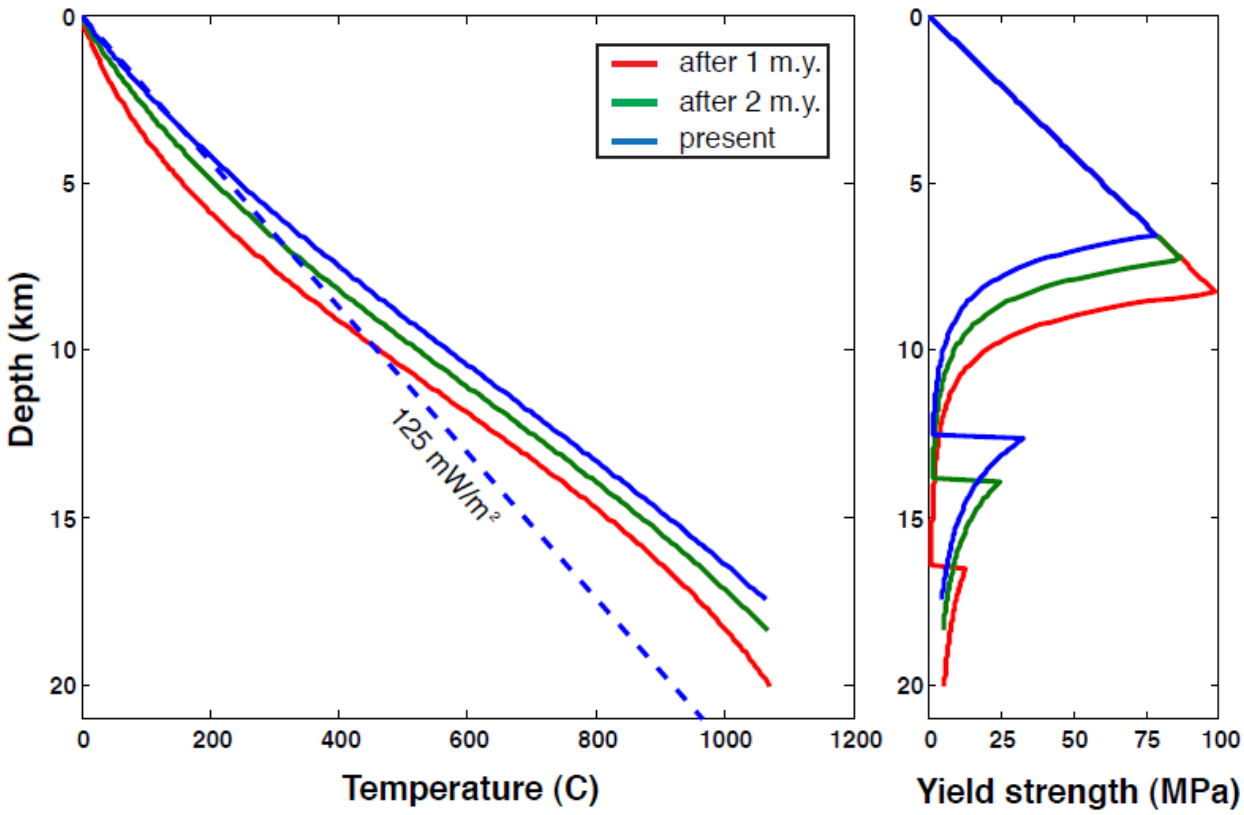

The geotherm and crust rheology at simulation time 1, 2 Myr and the present for Model B in Table 4.4. The blue dashed line is linear geotherm, corresponding to a conductive heat flow of 125 mW/m^2.

Figure 4.7

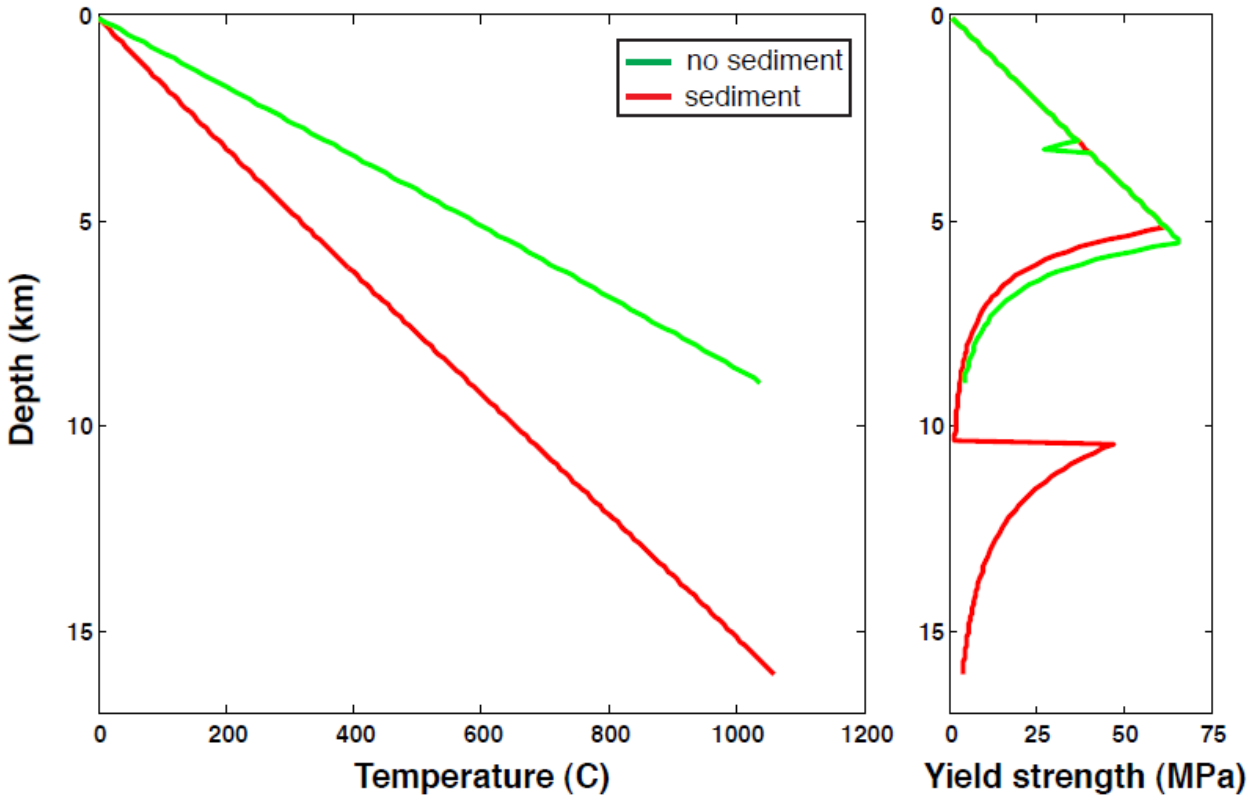

The geotherms and crust rheology after 10 Myr from the present with or without sedimentation. The model parameters are the same as Model B in Table 4.4.

Table 4.1. Kinematic and thermal model parameters

Symbol	Name	Unit	Value
h	crust thickness	km	h(t)
L	extensional length	km	L(t)
z	depth	km	
x	cell size	m	100
v	extension rate	cm/yr	2.6
r	strain rate	1/Myr	
S	sedimentation rate	m/yr	
M	magmatism rate	m/yr	
Ø	normalized sediment rate	dimensionless	
t	time	year	
Δt	time step	year	100
T	temperature	°C	
T_0	surface temperature	°C	0
T_a	basalt solidus temperature	°C	$T_a(h)$
T_b	adjusted magma temperature	°C	$T_b(h)$
T_m	adjusted basalt solidus temperature at sea level	°C	1010
G_m	gradient of basalt solidus	°C/km	3
L_a	latent heat	J/kg	L_a/c = 320 °C
c	specific heat of basaltic magma	J/(kg°C)	
k	thermal conductivity	W/(m°C)	2.72

ρ	rock density	kg/m^3	2800
c_p	rock specific heat	J/(kg°C)	
$k/\rho c_p$	thermal diffusivity	m^2/s	$9x10^{-7}$

Rock density, specific heat and conductivity are assumed to be constant for different rocks in the crust. The numerical method is capable of modeling these parameters as a function of rock composition. Thermodynamic parameter values are from *Lachenbruch et al.* [1985].

Table 4.2. Parameter in the benchmark model

Symbol	Unit	Value
h	km	23.5
L	km	100
v	cm/yr	1, 5
r	1/Myr	10%, 50%
Ø	dimensionless	0.4
T_0	°C	0
T_a	°C	1080.5
T_b	°C	1400.5

Table 4.3. Parameters for the Salton Trough steady state models

Symbol	Unit	Value
h	km	17.5
L	km	100
v	cm/yr	2.6
Ø	dimensionless	0.62, 0.71
T_0	°C	0
T_b	°C	1382.5

Table 4.4. Parameters for the Salton Trough non-steady state models

Model	magma generation rate (km^3/km/km)	sedimentation rate (km^3/km/km)	initial crust thickness (km)	initial rift width (km)	heat flow (mW/m^2)
A	5.8	3.6	32.6	13.8	109.1
B	6.0	3.7	27.0	16.7	108.0
C	6.2	3.8	23.3	19.4	107.2
D	6.4	3.9	20.6	21.9	106.2

Extension rate v is 2.6 cm/yr, the ratio Ø is 0.62, Tb is computed from equation (6).

Chapter 5

Future work

In previous chapters, I have showed that North American lithosphere in the central Salton Trough has been rifted apart for about 100 km, and is being replaced by new transitional crust added by magmatism from below and sedimentation from above (Chapter 2 and 3). The strain is localized and brittle in the upper crust, and wide distributed ductile in the lower crust and upper mantle. Rapid sedimentation plays an important role in the transition from rifting to drifting. It delays the breakup of the continental crust and prevents the initiation of mid-ocean ridges, by maintaining the thickness of the extended crust (Chapter 4).

However, the modeling in Chapter 4 is oversimplified, a three dimensional geodynamic modeling considering wider parameter ranges could improve our understanding on this extensional process. A comparison with other rifted continental margins, such as the Eastern North American margins, is important for understanding the evolution of continental rifting. This study has only used a small portion of the SSIP dataset. Clearly, more meaningful scientific results could be achieved from this dataset in the future, and some of them are closely related to this study.

5.1 Geodynamic modeling of the effects of thick sediment on the rifting process

A one dimensional kinematic model has been performed to study the effects of sediments upon continental rupture (Chapter 4), and successfully matches the heat flow measurement. However, three dimensional geodynamic modeling are required to fully understand this rifting process. *Bialas and Buck* [2009] has shown how sediment promotes the development of a narrow

rift in the Gulf of California, which is what we observe in the Salton Trough. It would be meaningful to use their numerical approach to verify the conclusion by my simple one dimensional model, and to study the essential role of thick sediment on the transition from continental rifting to oceanic spreading. For example, whether the crustal structure in the central Gulf of California is an intermediate stage of this transition, and how the rupture gets stabilized after the breakup of continental lithosphere. More interestingly, whether this transition works reversely, i.e. what will happen if a large amount of sedimentation is deposited on top of a currently active seafloor spreading center.

5.2 Comparison with other continental margins

In the southeastern United States, the rift-drift transition in the earliest Jurassic (~200 Ma) [*Withjack et al.*, 1998] resulted in the formation of the eastern North American margin and the opening of the Atlantic Ocean. While the Salton Trough has not reached that stage yet. The ongoing Eastern North American Margin (ENAM) project is to understand the breakup of ancient continents and the later evolution of this continental margin by landslides and other active processes, using active source onshore and offshore seismic data. The current East African Rift System (EARS) project is to investigate the basin evolution of the East African Rift, using newly reprocessed 2D and 3D seismic reflection data. The comparison of continental margins in the rifting and post-rift stages could improve the understanding of the full history of rift evolution. For instance, the passive continental margins in the central North America may contain significant amount of metamorphosed sedimentary rock, as observed in the Salton Trough.

5.3 Future work on SSIP dataset

This study is focused on the pull-apart basin inside the valley, additional work is required to better understand the geological structures outside the valley, especially to the west of the basin. The Line 1 and 2 upper crust P wave velocity structure has been compared at the intersection of two seismic lines in Chapter 2, however, the whole crust and upper mantle P and S wave velocity models have not been built yet. A comparison on the Moho depth and the upper mantle velocity and a three dimensional view of the Moho topography are very important for better understanding of the rifting process. A different middle crustal structure to the west of the Imperial Fault is evinced, but not carefully modeled yet. Full waveform inversion (FWI) has been successfully applied on Line 1 in northern Imperial Valley. This method could also be used along the central Line 3 and the OBS-airgun data to provide good constraints about the sediment-basement transition in the Salton Sea geothermal field and beneath the Salton Sea. It is also possible to apply FWI in eastern Line 4 in the Coachella Valley to study the structure of the San Andreas Fault. Numerous micro earthquakes ($M < 2$) have been recorded by the SSIP data. It would be valuable to systematically locate them for the understanding of seismicity and earthquake hazards in the Salton Trough. New heat flow data has been recently collected in the Imperial Valley by Dr. Collin Williams in USGS Menlo Park. A correlation of this high resolution heat flow data with the basement depth imaged in Chapter 2 could be very useful. The lower crust and upper mantle structure in the Coachella and Mexicali Valley is relatively poorly imaged, due to insufficient data density and quality. This should be considered when another seismic project is designed in the future.

References:

Bialas, R. W., and W. R. Buck, 2009. How sediment promotes narrow rifting: Application to the Gulf of California, *Tectonics*, 28, TC4014, doi:10.1029/2008TC002394.

Withjack, M. O., R. W. Schlische, and P. E. Olsen, 1998. Diachronous rifting, drifting, and inversion on the passive margin of central eastern North America: an analog for other passive margins, *AAPG Bulletin*, 82, 817-835.